ANGLE-RESOLVED PHOTOEMISSION SPECTROSCOPY OF FERROMAGNETIC EuO AND $SrRuO_3$ THIN FILMS

A Dissertation

Presented to the Faculty of the Graduate School

of Cornell University

in Partial Fulfillment of the Requirements for the Degree of

Doctor of Philosophy

by

Daniel Edward Shai

May 2014

ANGLE-RESOLVED PHOTOEMISSION SPECTROSCOPY OF FERROMAGNETIC EuO AND $SrRuO_3$ THIN FILMS

Daniel Edward Shai, Ph.D.

Cornell University 2014

Complex oxides are intensely studied due to their attractive materials properties, including a vast array of tunable and exotic electronic and magnetic phases. Experimental measurement of their electronic properties is a necessary first step toward understanding these materials and their ultimate utilization. In this thesis we describe the development and implementation of a state-of-the-art instrument which allows us to grow "artificial" structures of complex oxide thin films by molecular-beam epitaxy (MBE) and directly measure their momentum-resolved electronic structure using angle-resolved photoelectron spectroscopy (ARPES). We use this instrument to explore the momentum-resolved electronic properties of two ferromagnetic complex oxide materials, EuO and $SrRuO_3$.

We first present ARPES measurements on the doped ferromagnetic metal-insulator compound EuO. Our measurements in the low temperature ferromagnetic metallic state reveal charge carriers at the Brillouin zone boundary, consistent with density functional theory calculations, which predicts a half metal. Upon warming to to the paramagnetic phase, the metallic states at the zone boundary are transferred to pseudogapped states at the zone center. Our measurements also reveal a third type of charge carrier, which exists at Γ at all temperatures and corresponds to inactive dopants.

Through doping dependent measurements of EuO, we reveal a systematic evolution of the EuO valence band, which exhibits a diminished redshift and band gap, the later of which is consistent with dopant induced strain as indicated by first principles calculations. Near the

Fermi level, we discuss the pseudogapped states in terms of semi-localized charge carriers and present model calculations to support this. Finally, we discuss the formation of a two-dimensional free electron gas formed using deposition of Cs on the surface of EuO.

We then discuss the ferromagnetic 4*d* perovkite $SrRuO_3$. The Fermi surface in the ferromagnetic state consists of well-defined Landau quasiparticles exhibiting strong coupling to low-energy bosonic modes which contributes to the large effective masses observed by transport and thermodynamic measurements. Upon warming the material through its Curie temperature, we observe a substantial decrease in quasiparticle coherence but negligible changes in the ferromagnetic exchange splitting, suggesting that local moments play an important role in the ferromagnetism in $SrRuO_3$.

Biographical Sketch

Daniel Shai was born and raised in Akron, Ohio. It wasn't until he reached high school that he developed a strong interest in science by spending two summers working in a polymer engineering laboratory at the University of Akron. In 2003, he entered the College of Wooster, and unable to choose between Chemistry and Physics as a major, he decided to pursue both. He was fortunate enough to take advantage of the excellent undergraduate research programs offered at Wooster and elsewhere, and spent each of his summers and several of his academic years working on a number of undergraduate research projects, resulting in three publications. He graduated *summa cum laude* in 2007 as the first Wooster student to simultaneously earn Bachelor of Arts Degrees in both Physics and Chemistry.

That year, he moved to Ithaca, NY to continue his education at Cornell University. He joined the laboratory of Kyle Shen, a newly appointed professor in the physics department, and became one of the founding members of the ARPES research group at Cornell. There, he had the opportunity with the help of Kyle and several others to build a laboratory from scratch, starting with an empty room and developing the world class instrumentation it contains today. He earned a M.S. in Physics in January 2012, and continued in the Shen group while performing research toward his Ph.D. thesis which is presented here.

In 2007 Daniel was awarded a National Science Foundation Graduate Research Fellowship, and in 2008 he was awarded a NSF IGERT fellowship from the Cornell Center for Materials Research. Additionally he was recognized for his achievements through the 2007 Richard P. Feynman Award from the Cornell Physics Department.

Dedicated to Mom, Dad, and Katie.

Acknowledgments

Seven years is a long time to spend working full-time toward a Ph.D., and I wouldn't have lasted this long with out the help, guidance, and support from a very large group of people.

For nearly the entire duration of my time at Cornell, I have worked closely alongside two brilliant graduate students. Eric Monkman and John Harter – we've been through quite a lot together, and you have helped me in more ways than I can count. I cannot imagine what graduate school would have been like without you guys. The Shen group has grown in size dramatically with the addition of Shouvik Chatterjee, Bulat Burganov, Ed Lochocki, Haofei Wei, Jacob Ruf, and Brendan Faeth. Its been a pleasure getting to know you, watching you develop as scientists, and also watching myself transition to the role of a more senior graduate student in the process. I've also been fortunate enough to work with a number of excellent post-docs, including Dawei Shen, from whom I inherited the $SrRuO_3$ project and who was instrumental in combining the MBE and ARPES systems. More recently Yuefeng Nie, Phil King, and Masaki Uchida have each taught me a lot about growing and characterizing films, and have provided me with much valuable advice over the past few years. You've been great friends in and outside of the lab.

My advisor Kyle Shen has been a persistent source of help and motivation. I've really enjoyed watching him evolve from a new Assistant Professor to the supervisor he is today. Through it all, Kyle has always maintained an approachable demeanor and involved role in the lab, characteristics which can absent with busy professors. I have been afforded more opportunities than most graduate students by Kyle's doing, including traveling for beamtimes in Berlin, Paris, Palo Alto, Chicago, and beautiful and exotic Saskatoon. Kyle has spared virtually no expense to make our lives easier, including buying us a 3D printer and several top notch espresso machines to support the group's collective caffeine habit. I have fond memories of receiving interesting gadgets in packages addressed to me, but ordered by

Kyle, and trying to figure out where these ideas came from. Kyle has taught me a great deal about science and scientific equipment, and also about managing projects and people. And through Kyle, I've become a better writer and speaker. These skills will remain with me wherever I go.

I've also been fortunate enough to know a large number of bright and talented people in Darrell Schlom's group. I must thank Alexander Melville for growing all the EuO samples used in this thesis. Alex has an uncanny ability to get people to come out of their shell, and he used these powers on me every single day. Thanks to Carolina Adamo for growing all of the $SrRuO_3$ samples used in this thesis and for teaching me innumerable life lessons in the process. Carolina, your personality is a unique combination of warm, friendly, and tough, and it's remarkably effective. I've had so many interesting discussions with Rainer Held about science and about life over the past 2.5 years, and you've been a great biking and climbing partner and roommate. And thanks to Jessica Burton for all the coffees and for your friendship as well. I couldn't have asked for better friends, and I will miss you all.

Tassilo Heeg is a technical genius and I've learned a great deal about how to build equipment properly from him. Thanks to Julia Mundy for baking me and every other group member cakes on our birthdays. And to all the other Schlom group members: John Heron, Natalie Dawley, Hanjong Paik, Hari Nair, Charles Brooks, Shaobo Zhu, Che-Hui Lee, Gino Maritato, Alice Galdi, Joshua Tashman, and Arsen Soukiassian – its been fun!

I've learned a lot about materials science and film growth from Professor Darrell Schlom. Darrell's encyclopedic knowledge of oxides and MBE is simply astounding, and on a number of occasions, he's been able to solve my problems with an aptly chosen phase diagram. Darrell's enthusiasm for the work we do is contagious, which is particularly helpful when he comes by the lab to chat and see new results in the middle of a long night shift.

Mark H. Fischer has helped me understand many things pertaining to EuO, and Eun-Ah

Kim has helped maintain focus on what are important and worthy goals for the project. Additionally, I've had a number of useful discussions with Andreas Schmehl and Thomas Mairoser. And Tom Regier, David Hawthorne, and Andrew Achkar taught me much about x-ray absorption spectroscopy on EuO during my beamtimes at the Canadian Light Source.

When starting a new physics lab, you rely heavily on the machine shop and user facilities managers. Nathan Ellis has taught me everything I know about machining, which to my initial surprise, I've found I thoroughly enjoy. The rest of the Clark Hall staff, including Stanley Carpenter, Rodney Bowman, and Bob Tillotson, Eric Smith, Steve Kriske, and Jon Shu have all helped me accomplish many things during my time here.

The vast majority of this thesis was written on Lola Brown's dining room table while she provided me with food, coffee, and moral support. Lola, you deserve an extremely special thank you for your curiosity and optimism, which have frequently helped me view things from a fresh perspective.

And finally and most importantly I must thank my family. Mom and Dad, you have always encouraged and supported me in everything I've wanted to do, and I wouldn't be writing this if it weren't for you. And to my sister Katie, who is in many ways my diametric opposite, especially when it comes to career choices. You have always been willing to listen to me, and I've always valued your perspective and input. Your love and support has extended far longer than the past seven years, and I am tremendously grateful for all you do for me. Thanks to each of you!

Daniel Shai

April 2014

Table of Contents

List of Figures

List of Tables

CHAPTER 1

Introduction

For over fifty years, the semiconductor transistor has been the workhorse of the computing industry. Since Gordon Moore originally published his work on the proliferation of the number of devices on an integrated circuit [1], the trend toward miniaturization of devices has steadily continued. Yet it is widely accepted that the transistor as we know it is approaching its fundamental physical limitations and therefore further miniaturization cannot continue indefinitely [2]. As power dissipation increasingly becomes a problem in devices, it is clear that a new technology is needed in order to continue the technological advancements which have been enjoyed over the past half century.

Given these inherent physical limitations, it is likely that the next breakthrough in electronics will be materials-based, with a move away from so-called conventional materials like Si and GaAs, toward systems with more complex behavior. A promising class of materials are complex oxides, systems containing rare earth and transition metal cations combined with oxygen anions. The electronic properties in these materials are derived from strongly correlated d and f electrons, which results in a wide variety of exotic and potentially useful phenomena such as magnetism, colossal magnetoresistance, superconductivity and ferroelectricity [3, 4]. Moreover, the large carrier densities supported by oxides allow for superior miniaturization and scaleability as compared to traditional semiconductors [5]. In fact, rare earth and transition metal oxides have already begun to make their way into electronics and other related applications. For example, the Intel corporation has incorporated HfO_2 as a high-κ gate dielectric in their transistors [6], and high

temperature superconducting wire is being incorporated into the United States power grid [7]. Oxide-based ferroelectrics have been utilized recently by the Texas Instruments corporation to generate ultra-low-power and high speed non-volatile FRAM [8].

Despite the limitations of conventional materials, they are still the primary components in the microelectronics industry. This is partly due to the extremely high material quality achievable, which results from decades of materials growth optimization. Yet the quality of complex oxides is improving substantially. A commonly noted example is the observation of the fractional quantum hall effect in (Mg,Zn)O/ZnO heterointerfaces with electron mobilities exceeding 180,000 $cm^2V^{-1}s^{-1}$ [9]. Furthermore, the integration of oxides on semiconductors [10] adds enormous benefit to their use in electronics, as it enables the use of oxide components without completely abandoning the semiconductor infrastructure developed over the past five decades.

The novel ground states and potentially useful properties exhibited by oxides are a result of their spin, charge, orbital, and lattice degrees of freedom which are often strongly coupled. In this thesis we will focus on two complex oxides where the spin and charge degrees of freedom are intimately related. These materials are:

Europium Monoxide (EuO). A ferromagnetic oxide with large spin polarization ($P > 95\%$) [11], a large metal-insulator transition ($\Delta\rho/\rho \approx 10^{13}$) [12, 13] and colossal magnetoresistance ($\Delta\rho/\rho \approx 10^{6}$) [14]. EuO can be grown epitaxially on mainstream semiconductors like Si, GaN [15], and GaAs [16], and the ability of EuO to filter spins in a tunnel junction has been demonstrated [17].

Strontium Ruthenate ($SrRuO_3$). A metallic perovskite with properties largely applicable in the field of oxide electronics [18]. $SrRuO_3$ is ferromagnetic, and exhibits signs of strong correlations such as a large effective mass. The charge carriers in $SrRuO_3$ are spin

polarized and have been predicted to reach 100% polarization in thin film heterostructures [19]. Moreover $SrRuO_3$ has attracted attention from the spintronics community due to the correlation between its magnetic and charge transport properties [20, 21].

These materials, and oxides as a whole, are difficult to describe due to their competing interactions and inherently complex nature [22]. Despite decades of research on both compounds, there are numerous questions of about their basic behavior which have gone unanswered. There is a need for experiments to understand even the most fundamental properties, such as the nature of their electronic band structure, how it responds to controllable parameters such as temeprature and doping, and how it is related to more macroscopic phenomena. These questions will be addressed in this thesis.

While both of these materials exist in bulk form, we will focus on epitaxial thin films grown by reactive oxide molecular-beam epitaxy (MBE). This approach enables us to overcome several technical difficulties related to these materials but the advantages of using thin films extends far beyond these. The controlled growth of complex oxides in thin film form offers a way to engineer new functionalities in ways that cannot be achieved in bulk [23, 24]. For example, crystalline thin films grown epitaxially in registry with an underlying crystalline substrate allow one to explore the effects of epitaxial strain. By deliberately choosing a substrate material with a lattice parameter slightly different from that of the film material, one can grow a film which is strained biaxially by the substrate. Often this can amount to several per cent changes in lattice parameter, and can result in completely different properties of the film. By exploiting the atomic level control offered by deposition techniques such as MBE, one can explore finite size and quantum confinement effects in films which are only several monolayers thick, or which are 'sandwiched' between other materials. And perhaps the most powerful advantage to using thin films are the emergent phenomena which can be achieved through heterostructures and interfaces. The most well-known

example of interface physics is the two-dimensional electron gas which forms at the interface between two band insulators, $LaAlO_3$ and $SrTiO_3$, but there are numerous others (for a review, see Refs. [25, 26]). While we focus on films EuO and $SrRuO_3$ without complexities such as quantum confinement and heterostructuring, the equipment developed and results drawn in this thesis will be useful and extendable to studying more complex systems based on these materials.

1.1 Outline of this thesis

In this thesis, we will describe original experimental research performed on EuO and $SrRuO_3$ thin films. The thesis is divided into eleven chapters, summarized as follows. In Chapter 2 we will discuss angle-resolved photoemission spectroscopy (ARPES), the main experimental tool used to characterize the materials outlined above. We will also describe the unique capability of the ARPES system used here to characterize thin films grown by molecular-beam epitaxy. In Chapter 3 we will review the properties of Europium monoxide (EuO), focusing on the doping-induced ferromagnetic metal-insulator transition. In Chapter 4 we will discuss the growth process for producing high quality EuO thin films for characterization by photoemission, and we will describe a number of other characterization techniques used on EuO. In Chapter 5, we will discuss the temperature-dependent electronic structure in doped EuO as imaged by ARPES. We will continue our characterization of doped EuO in Chapters 6 & 7, where we will describe how the electronic structure in the valence band and near the Fermi level evolve with doping. We will conclude our discussion of EuO by exploring the formation of a two-dimensional electron gas on the surface of EuO in Chapter 8. In Chapter 9, we will discuss some of the properties of $SrRuO_3$ and describe how thin films are grown. Then in Chapter 10 we will discuss the characterization of $SrRuO_3$ by ARPES, focusing on the structure of the Fermi surface, presence of many-body interactions, and nature of its

ferromagnetic ground state. Finally, in Chapter 11 we will discuss the conclusions drawn in this thesis as well as potential future directions a continuation of this research could take.

CHAPTER 2

Angle-Resolved Photoemission Spectroscopy

The primary experimental characterization tool used in this thesis is angle-resolved photoemission spectroscopy, or ARPES. ARPES is an extremely powerful tool for probing charge carrier dynamics in crystalline systems. By utilizing both energy and momentum resolution, ARPES enables us to map out the single particle spectral function, $\mathcal{A}(k, \omega)$, which encodes information about the band structure (E vs. k) relationship, Fermi surface, as well as many-body effects governing the occupied electronic states in a crystal.

In this Chapter, we will review the historical development of photoemission as a probe of solid state systems. We will then discuss some of the theoretical aspects of the photoemission process, including many-body effects such as electron-phonon coupling which are relevant to the interpretation of the data presented in subsequent Chapters. We will include a technical description of the ARPES system constructed in part by the author as part of this thesis. Finally, we will describe the most unique functionality of this system, which is the ability to accept thin film samples grown by molecular-beam epitaxy (MBE).

2.1 Historical development of photoemission as a probe of solid state systems

Photoemission spectroscopy is a relatively mature experimental technique, and there are multiple textbooks [27, 28] and review articles [29] which cover many aspects of the subject.

The photoelectric effect was discovered experimentally by Heinrich Hertz in 1887 [30]. Hertz found that while using an induction coil to generate an electrical arc, he could induce an arc in a subsequent coil as a result of the ultraviolet radiation produced in the initial arc. Following this discovery, a number of others began to investigate this phenomena, but one of the most significant contributions came from Philipp Lenard, who began working as Hertz's assistant. Lenard characterized the velocity distribution of charged particles (then called "cathode rays") from a cathode exposed to ultraviolet light [31, 32]. Lenard concluded that the maximum energy of these particles was proportional to the frequency of the incident light, and the number of particles was proportional to the light intensity. This observation was wholly inconsistent with the classical description of light described by Maxwell's equations, which gives the energy of light as proportional to the intensity. Lenard was awarded the Nobel Prize in Physics in 1905 for his work on cathode rays.

The same year, Albert Einstein published his paper [33] explaining that light must be considered as quantized into individual photons. This description led to the famous Einstein equation,

$$E_{\mathrm{k,max}} = h\nu - \phi, \tag{2.1}$$

which relates the maximum kinetic energy of the photoelectron ($E_{\mathrm{k,max}}$) to the incident light energy ($h\nu$) through the sample work function (ϕ). This interpretation led to Einstein being awarded the 1921 Nobel prize in Physics. Equation (2.1) was subsequently verified through the photoemission experiments by Millikan [34], who was awarded the Nobel Prize in Physics for his work in 1923.

Photoemission was developed as a spectroscopic tool in the 1950s and 1960s, notably through the work of Berglund and Spicer on Cu and Ag, published in 1964 [35–37]. The same year E.O. Kane proposed that by combining photoemission with momentum resolution,

the band structure of a crystal could be mapped [38], but experimental evidence for ARPES was not demonstrated for 10 more years, until Traum, Smith, and Di Salvo performed the first ARPES experiments on 1*T*-$TaSe_2$ [39, 40]. Another photoemission-related Nobel Prize in Physics was awarded In 1981, this time to Kai Siegbahn for his contributions to developing x-ray photoelectron spectroscopy.

2.2 Three-Step Model

In this section we will begin to develop the theoretical framework describing the photoemission process. Although photoemission is not limited to crystalline solids, in the discussion that follows, we will limit ourselves to consider only these systems, as they are most relevant to this thesis and the loss of generality to other systems will simplify the description somewhat.

A complete description of the photoemission process must use the so-called one-step model, which treats the excitation process as a single coherent quantum mechanical process of an N body wavefunction subjected to boundary conditions which account for the crystalline potential, solid-vacuum interface, and propagation of the photoelectron through vacuum to the spectrometer. Such a description is usually prohibitively complex, which has led to a semiclassical description of the photoemission process which is broken down into three distinct steps. These are

1. Optical transition between an initial and final state in the bulk.
2. Propagation of the photoexcited electron to the sample surface.
3. Escape of the electron from the solid into the vacuum.

Only the first step is treated quantum mechanically, as will be described in §2.4. The

primary effect of step 2 is to account for inelastic scattering of the photoelectron wavefunction, which forces the electron wavevector to be complex. Step three involves overcoming the surface potential barrier which imposes kinematic constraints on on the measured photoelectron momentum, as will be described below.

2.3 Kinetics and Energetics of Photoemission

Photoemission involves the absorption of a photon by a crystal and a subsequent emission of a photoelectron with energy E_{kin} and momentum $\hbar\mathbf{K}$ which are then detected by an electron spectrometer. Experimentally, one measures E_{kin} and the direction (emission angle) of the photoelectron, which can be converted into its momentum. Using energy and momentum conservation laws, these quantities can then be converted into binding energy and crystal momentum of the electron prior to its photoexcitation.

Following the absorption of a photon with energy $E_{h\nu}$, a hole is created in an occupied state and the electron is promoted above the vacuum level and subsequently escapes the crystal and is detected with kinetic energy E_{kin}, which related to binding energy by

$$E_{kin} = E_{h\nu} - \phi - |E_B|\,, \tag{2.2}$$

where $E_{h\nu}$ is the photon energy and ϕ is the work function.

The momentum of the photoelectron can also be related to the original momenta of the electron within the solid through the use of momentum conservation laws. The photoelectron momentum $\mathbf{K}$ is determined by through measurement of the emission angle from the sample combined with the overall magnitude $|\mathbf{K}| = \frac{1}{\hbar}\sqrt{2m_e E_{kin}}$, where m_e is the free electron mass. Because of the discrete translational symmetry of the crystal in the in-plane directions, the in-plane crystal momentum of the electron is conserved in the photoemission

process. The crystal momentum of the electron prior to photoexcitation is directly related to the measured photoelectron momentum through

$$k_x = K_x + G_x \tag{2.3}$$

$$k_y = K_y + G_y. \tag{2.4}$$

where **G** is a reciprocal lattice vector. The out-of-plane component of the electron's momentum is not conserved due to the symmetry breaking at the surface of the sample. For quasi two-dimensional systems, knowledge of the out-of-plane component of the initial state momentum is irrelevant due to the minimal dispersion expected in that direction. For fully three-dimensional materials studied in this thesis, however, knowledge of the out-of-plane momentum is critical and therefore warrants further discussion.

Absolute determination of the crystal momentum requires detailed knowledge of both the initial and final states. Typically, one approximates the final state dispersion using the nearly free electron model [41]. In this case, one assumes that the final-state has a free electron-like dispersion represented as

$$E_f^{NFE}(\mathbf{k}) = \frac{\hbar^2 \mathbf{k}^2}{2m} - |E_0| = \frac{\hbar^2 \left(k_\perp^2 + k_\parallel^2\right)}{2m} - |E_0|\,, \tag{2.5}$$

where E_0 represents the bottom of the band, referenced to the Fermi energy. Solving Equation (2.5) for the out-of-plane momentum component one arrives at

$$k_\perp = \frac{1}{\hbar}\sqrt{2m(E_{kin} + V_0) - k_\parallel^2}, \tag{2.6}$$

where we have defined the *inner potential*, $V_0 = |E_0| + \phi$. Experimentally, V_0 is determined by utilizing photon energy dependent synchrotron-based photoemission spectroscopy.

By varying the incident photon energy (and thus E_{kin}), one can analyze the symmetry of the photoemission spectra and therefore determine which photon energies probe crystallographically equivalent momentum points. By utilizing Equation (2.6), one can determine V_0 for a particular material. Once V_0 is known, it can in principle be used in conjunction with Equation (2.6) to determine $k_\perp$ for an arbitrary photon energy.

2.3.1 Angle to Momentum Conversion

In this section we will discuss how to express the in-plane momenta k_x and k_y in terms of the three angular degrees of freedom one has when rotating a sample. In Figure 2.1 we illustrate the laboratory coordinate system for the experimental apparatus used to acquire all data in this thesis (see §2.7). The sample can be translated linearly in three orthogonal directions (x, y, and z), and rotated in three directions (θ, ϕ, and ω). In the discussion that follows, we will use the notation $\mathbf{X}_{\text{lab}}$ to denote a three dimensional vector with respect to the laboratory coordinate system, and $\mathbf{X}_{\text{sample}}$ to denote a vector with respect to the sample coordinate system.

As illustrated in Figure 2.1, an arbitrary point in k-space can be accessed by consecutive rotations of the three orthogonal angular directions. Using these rotations, we convert between coordinate systems through rotation matrices represented by

$$\mathbb{R}_\theta = \begin{pmatrix} \cos\theta & \sin\theta & 0 \\ -\sin\theta & \cos\theta & 0 \\ 0 & 0 & 1 \end{pmatrix}, \mathbb{R}_\phi = \begin{pmatrix} 1 & 0 & 0 \\ 0 & \cos\phi & -\sin\phi \\ 0 & \sin\phi & \cos\phi \end{pmatrix}, \mathbb{R}_\omega = \begin{pmatrix} \cos\omega & 0 & \sin\omega \\ 0 & 1 & 0 \\ -\sin\omega & 0 & \cos\omega \end{pmatrix}. \quad (2.7)$$

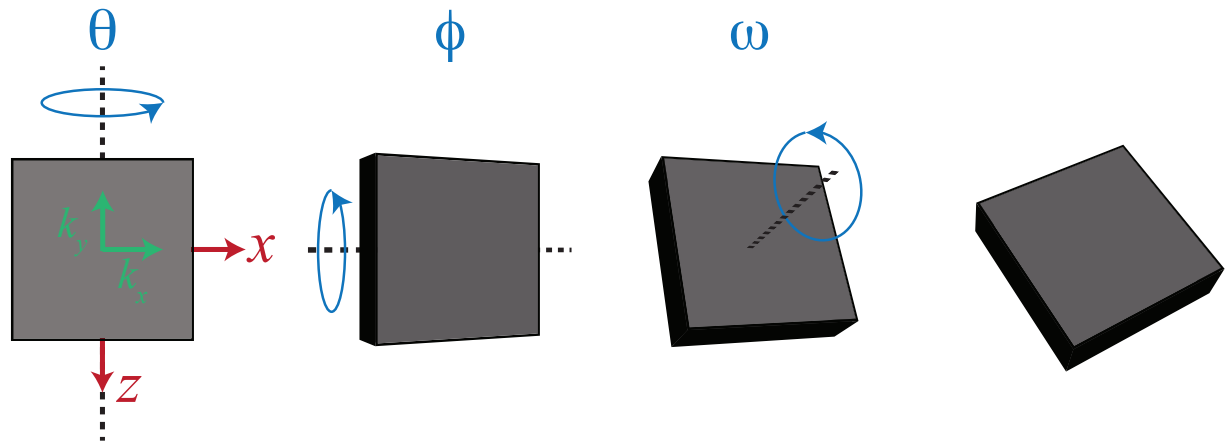

Figure 2.1: Schematic showing the three angular rotations performed on a sample to access an arbitrary point in k-space. The cartesian laboratory coordinates are shown in red, crystal momentum coordinates are shown in green (note: $\hat{y}$ points into the page, $\hat{k}_z$ points out of the page), and angles are colored blue.

Then an arbitrary vector in the laboratory coordinate system can be converted to the sample coordinate system by

$$\mathbf{X}_{\text{sample}} = \mathbb{R}_\omega \mathbb{R}_\phi \mathbb{R}_\theta \mathbf{X}_{\text{lab}}. \tag{2.8}$$

Taking into account the finite angular acceptance of the analyzer, given as $\pm q$, a photoelectron will be measured if it has momentum $\mathbf{X}_{\text{lab}} = \{0, p\cos q, p\sin q\}$, where $p = \sqrt{2mE_k}/\hbar$. The momenta in the sample frame of reference $\mathbf{X}_{\text{sample}} = \left\{k_x, \tilde{k}_z, k_y\right\}$, where $\tilde{k}_z$ does not represent the true out-of-plane momentum of the initial state since k_z is not conserved in the photoemission process, as discussed above. By applying the transformation in Equation (2.8) to the photoelectron momenta, one can directly compute the electron momenta prior to the photoexcitation:

$$k_x = \frac{\sqrt{2mE_k}}{\hbar}\left[\sin q\cos\phi\sin\omega - \cos q\left(\sin\theta\cos\omega + \cos\theta\sin\phi\sin\omega\right)\right] \tag{2.9}$$

$$k_y = \frac{\sqrt{2mE_k}}{\hbar}\left[\sin q\cos\phi\cos\omega + \cos q\left(\sin\theta\sin\omega - \cos\theta\sin\phi\cos\omega\right)\right]. \tag{2.10}$$

2.3.2 Surface Sensitivity and Final State Effects

Due to strong interactions, electrons scatter rapidly within a crystal. These scattering processes will alter the photoelectron momentum and also energy for inelastic processes. Thus, in ARPES, only ballistic (non-scattered) electrons originating near the sample surface can be used to extract initial-state E vs. k relationships. The relevant length scale is the inelastic mean free path or escape depth, λ. While λ is an energy-dependent quantity, the work by Seah and Dench [42] has shown that it is roughly material independent. In Figure 2.2, we show values of λ measured as a function of kinetic energy for a compilation of different materials. All data points follow the so-called "universal curve," which can be used to estimate λ for any photoemission measurement. Most ARPES measurements are performed in the vacuum ultraviolet (VUV) range, with kinetic energies typically from 10-100 eV. In this range λ is a minimum, typically, less than 1 nm.

A consequence of the finite escape depth of the photoelectron final state is a momentum broadening in the out-of-plane $\hat{\mathbf{z}}$ direction [43]. If one assumes a free-electron-like final state which is damped by the finite value of λ,

$$\psi(z) = \frac{1}{\sqrt{\lambda}}\exp(ik_{z0}z)\exp(z/2\lambda), \tag{2.11}$$

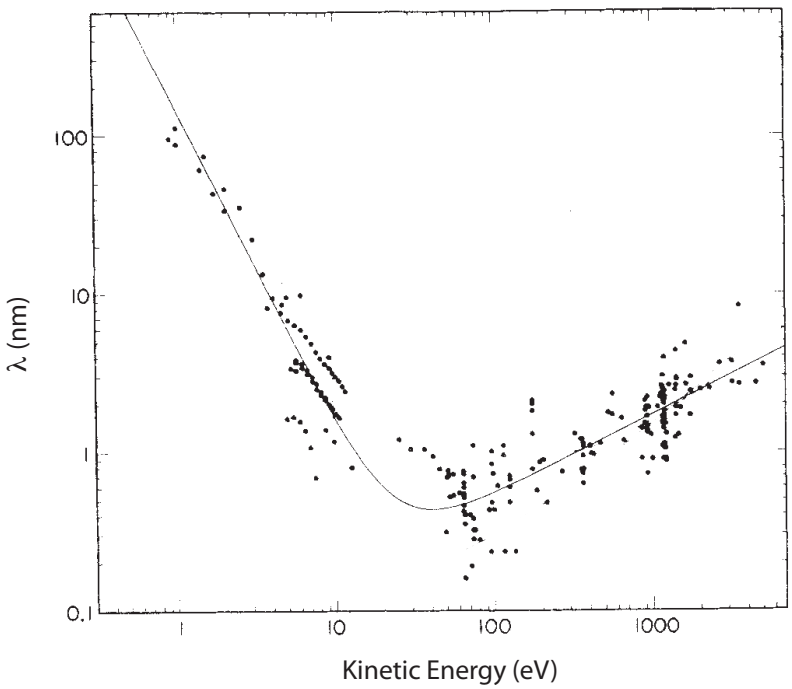

Figure 2.2: Plot of inelastic mean free path, λ versus electron kinetic energy compiled by Seah and Dench. Reprinted with permission from Ref. [42].

then the final state in momentum-space can be expressed as

$$\phi(k_z) \propto \frac{1}{i(k_z - k_{z0}) - 1/2\lambda}, \tag{2.12}$$

and the probability distribution $\left|\phi(k_z)\right|^2$ is given by

$$\left|\phi(k_z)\right|^2 \propto \frac{1}{2\lambda}\frac{1}{(k_z - k_{z0})^2 - (1/2\lambda)^2}. \tag{2.13}$$

Equation (2.13) has the form of a Lorentzian function centered at k_{z0} with width $1/\lambda$. The implication is that a photoemission measurement which probes the momentum value k_{z0} actually probes a weighted average of states centered at k_{z0} and with width $1/\lambda$. In the limit of bulk sensitivity, as λ becomes large, Equation (2.13) reduces to a delta function $\delta(k_z - k_{z0})$, implying that such final state broadening mechanisms become less important. In the VUV

range, where $\lambda \sim 1$ nm, the effects of k_z smearing can be quite significant, as is described for example in Ref. [43].

2.4 Quantum Mechanical Description of the Photoexcitation Process

We return to Step 1 of the three-step model, which describes the optical excitation of the electron between initial and final states. The transition probability for such an excitation can be approximated using Fermi's golden rule as

$$w_{fi} = \frac{2\pi}{\hbar} \left| \left\langle \Psi_f^N \middle| \hat{\mathcal{H}}_{int} \middle| \Psi_i^N \right\rangle \right|^2 \delta(E_f^N - E_i^N - h\nu), \tag{2.14}$$

where the Hamiltonian $\hat{\mathcal{H}}_{int}$ describes the interaction between the electron and the electromagnetic field, and takes the form [27]

$$\hat{\mathcal{H}}_{int} \approx \frac{i\hbar}{mc} \left(\mathbf{A} \cdot \nabla \right). \tag{2.15}$$

By assuming that the N body wavefunction can be factored into a Slater determinant of a single electron wavefunction ϕ and an $N-1$ body wavefunction Ψ^{N-1}, and under the assumption that the $N-1$ body system does not interact with the excited photoelectron (the so-called *sudden approximation*) then the combination of Equations (2.14) and (2.15) can be used to derive an expression for the photoelectron intensity:

$$I(\mathbf{k}, \omega) = \sum_{f,i} \left| M_{f,i}^{\mathbf{k}} \right|^2 \sum_m \left| c_{m,i} \right|^2 \delta \left(E_k + E_m^{N-1} - E_i^N - h\nu \right) \tag{2.16}$$

where the summation indices f and i run over all final and initial states, and m runs over all eigenstates of the $N-1$ electron system. In Equation (2.16), $M_{f,i}^{\mathbf{k}} = \left\langle \phi_f^{\mathbf{k}} \middle| \hat{\mathcal{H}}_{int} \middle| \phi_i^{\mathbf{k}} \right\rangle$ represents a

one-electron matrix element describing the photoexcitation, and $\left|c_{m,i}\right|^2 = \left|\left\langle \Psi_m^{N-1} \middle| \Psi_i^{N-1} \right\rangle\right|^2$ represents the probability that following the removal of the electron the initial state will be left in state m. For a non-interacting electron gas, $c_{m,i}$ will be a delta function for a particular eigenstate, whereas in general for an interacting electron system, c_{mi} will have many non-zero values. (For a clear illustration, see Figure 3 of Ref. [44]).

2.4.1 Relationship to Green's Function

The functional form of the photoelectron intensity in Equation (2.16) bears strong resemblance to the Green's function formalism used to describe electron propagation in many-body systems. The single-particle spectral function, formally defined as the imaginary part of the single-particle Green's function $\mathcal{G}(\mathbf{k}, \omega)$, is given by [44]

$$\mathcal{A}(\mathbf{k}, \omega) \equiv -\frac{1}{\pi} \mathrm{Im}\, \mathcal{G}(\mathbf{k}, \omega) \tag{2.17}$$

$$= \sum_m \left|\left\langle \Psi_m^{N-1} \middle| \hat{c}_{\mathbf{k}} \middle| \Psi_i^N \right\rangle\right|^2 \delta(\omega - E_m^{N-1} + E_i^N) \tag{2.18}$$

where $\hat{c}_{\mathbf{k}}$ is the annihilation operator for state with momentum $\mathbf{k}$. By combining Equations (2.16) and (2.18) and noting that $\hat{c}_{\mathbf{k}} \left|\Psi_i^N\right\rangle = \left|\Psi_i^{N-1}\right\rangle$, the total photoelectron intensity can be written as

$$I(\mathbf{k}, \omega) = \sum_{f,i} \left|M_{f,i}^{\mathbf{k}}\right|^2 f(\omega) \mathcal{A}(\mathbf{k}, \omega), \tag{2.19}$$

where the fermi function $f(\omega) = \left(e^{\omega/k_B T} + 1\right)^{-1}$ has been added to explicitly account for the fact the ARPES measures only occupied states. Equation (2.19) shows that the measured photoelectron intensity is directly proportional to the single-particle spectral function.

2.5 Energy and Momentum Distribution Curves

With modern photoemission analyzers, the use of multiplexing lenses enables the simultaneous spectral acquisition from numerous emission angles, producing E vs. k images (band structure plots), e.g., shown in Figure 2.3 . While these images provide a useful overall picture, quantitative analysis is typically performed by 'slicing' these images into lines of constant momentum or energy, producing so-called energy distribution curves (EDCs) or momentum distribution curves (MDCs), respectively. In this section, we will show that analysis of such curves yields quantitative information regarding band dispersion and quasiparticle renormalizations and lifetimes.

For an interacting system, the one-particle Green's function can be expressed in the form of Dyson's equation [45]:

$$\mathcal{G}(\mathbf{k},\omega) = \frac{1}{\omega - \varepsilon_{\mathbf{k}} - \Sigma(\mathbf{k},\omega)} \tag{2.20}$$

where the bare band dispersion is denoted by $\varepsilon_{\mathbf{k}}$ and the correlation effects are accounted for by the complex self-energy, $\Sigma(\mathbf{k},\omega) = \Sigma'(\mathbf{k},\omega) + \mathrm{i}\Sigma''(\mathbf{k},\omega)$. The spectral function then takes the form

$$\mathcal{A}(\mathbf{k},\omega) = -\frac{1}{\pi}\frac{\Sigma''(\mathbf{k},\omega)}{(\omega - \varepsilon_{\mathbf{k}} - \Sigma'(\mathbf{k},\omega))^2 + (\Sigma''(\mathbf{k},\omega))^2}. \tag{2.21}$$

To represent an EDC, for a given $\mathbf{k}$ if we restrict ourselves to ω near the pole energy $E^*_k = \varepsilon_{\mathbf{k}} - \Sigma'(\mathbf{k}, E^*_{\mathbf{k}})$, then we can linearly expand $\Sigma'(\mathbf{k},\omega)$ in ω:

$$\omega - \varepsilon_{\mathbf{k}} - \Sigma'(\mathbf{k},\omega) \approx \frac{1}{Z_{\mathbf{k}}}(\omega - E^*_{\mathbf{k}}) \tag{2.22}$$

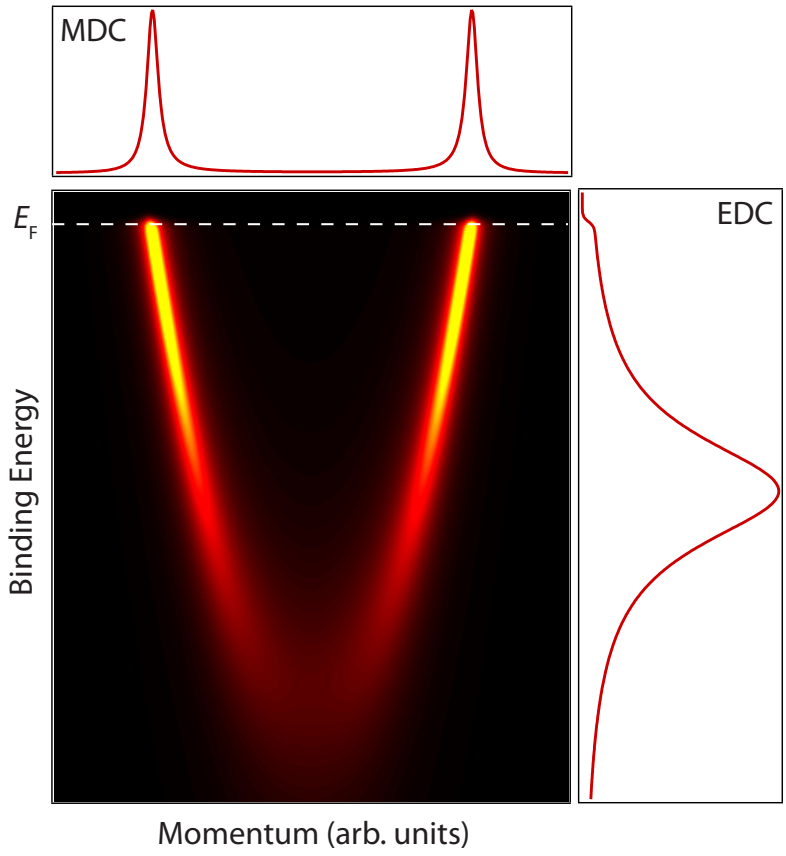

Figure 2.3: Simulated photoemission data illustrating the decomposition of a 2D image into MDCs and EDCs. The MDC represents the momentum distribution at E_F and the EDC represents the energy distribution at $k = 2k_F/3$.

where $Z_{\mathbf{k}}^{-1} \equiv 1 - \partial_\omega \Sigma'(\mathbf{k}, \omega)|_{\omega = E_{\mathbf{k}}^*}$. We then rewrite Equation (2.21) as

$$\mathcal{A}(\mathbf{k}, \omega) = Z_{\mathbf{k}} \frac{\Gamma_{\mathbf{k}}/\pi}{(\omega - E_{\mathbf{k}}^*)^2 + \Gamma_{\mathbf{k}}^2} + \mathcal{A}_{inc}, \tag{2.23}$$

where we have defined $\Gamma_{\mathbf{k}} = Z_{\mathbf{k}} \left|\Sigma''(\mathbf{k}, E_{\mathbf{k}}^*)\right|$. The energy lineshape of Equation (2.23) is a Lorentzian with integrated weight $Z_{\mathbf{k}}$ (referred to as the quasiparticle residue) and width $\Gamma_{\mathbf{k}}$ (the quasiparticle scattering rate). The non-Lorentzian contribution to $\mathcal{A}(\mathbf{k}, \omega)$ is collected the incoherent part of the spectral function, $\mathcal{A}_{inc}$.

Instead if we analyze MDCs, assuming an isotropic (non-directional) linear dispersion, $\varepsilon_k = v_{\mathrm{F}} \cdot (k - k_{\mathrm{F}})$ yields

$$\mathcal{A}(k, \omega) = -\frac{1}{\pi} \frac{\Sigma''(k, \omega)}{\left[\omega - v_{\mathrm{F}} \cdot (k - k_{\mathrm{F}}) - \Sigma'(k, \omega)\right]^2 + \left[\Sigma''(k, \omega)\right]^2} \tag{2.24}$$

$$= -\frac{1}{\pi} \frac{\Sigma''(k, \omega)/v_{\mathrm{F}}^2}{\left[k - k_{\mathrm{F}} - (\omega - \Sigma'(k, \omega))/v_{\mathrm{F}}\right]^2 + \left[\Sigma''(k, \omega)/v_{\mathrm{F}}\right]^2}. \tag{2.25}$$

For a given ω, Equation (2.25) has the form of a Lorentzian distribution centered at

$$k_m = k_{\mathrm{F}} + (\omega - \Sigma'(k, \omega))/v_{\mathrm{F}} \tag{2.26}$$

with half-width at half-maximum

$$W(k) = -\Sigma''(k, \omega)/v_{\mathrm{F}}. \tag{2.27}$$

Equations (2.26) and (2.27) can be solved for the self-energy, $\Sigma(k, \omega)$, giving

$$\Sigma'(k, \omega) = \omega - v_{\mathrm{F}} \cdot (k_m - k_{\mathrm{F}}) \tag{2.28}$$

$$\Sigma''(k, \omega) = -v_{\mathrm{F}} \cdot W(k). \tag{2.29}$$

While the overwhelming majority of self-energy analyses of ARPES data make the assumption of a linear bare band dispersion, it is possible to derive expressions equvalent to Equations (2.28) and (2.29) for a quadratic bare band dispersion [46].

2.6 Coupling to Bosons

One important aspect from the above discussion is that ARPES not only measures band structure (E vs k) for materials, but it is also sensitive to many-body interactions not accounted for in a traditional one-electron description of a crystal. Such interactions include electron-electron interactions as well as coupling between electrons and other particles such as bosons. Here as an illustrative example, we describe the effect of coupling to a phonon on the single-particle spectral function.

Electron-phonon coupling is parameterized by the Eliashberg function, $\alpha^2F(\omega)$ which contains information about the density of phonon states $F(\omega)$ and how strongly they are coupled to the electrons in the system (coupling α). To illustrate the effect of the electron-phonon interaction on the electron self-energy, consider a single dispersionless Einstein phonon ($E = \hbar\omega_E$) which couples isotropically in k-space. The Eliashberg function for this case is

$$\alpha^2F(\omega) = \frac{\lambda\omega_E}{2}\delta(\omega - \omega_E). \tag{2.30}$$

With knowledge of $\alpha^2F(\omega)$, the self-energy can be computed directly [47]:

$$\Sigma'(\omega) = -\frac{\lambda\hbar\omega_E}{2}\ln\left|\frac{\omega + \omega_E}{\omega - \omega_E}\right|, \tag{2.31}$$

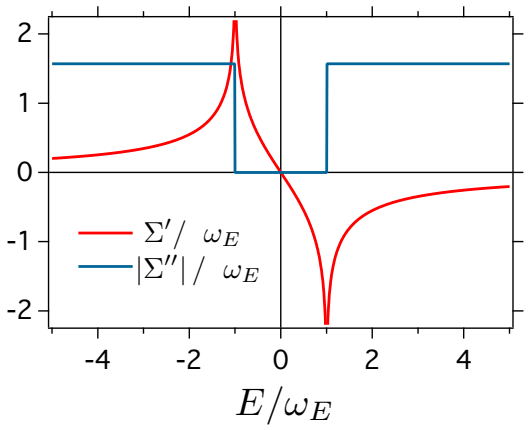

Figure 2.4: Contribution of an Einstein phonon to the electron self-energy at $T = 0$.

and

$$|\Sigma''(\omega)| = \frac{\lambda\pi\omega_E}{2} H\left(|\omega| - \omega_E\right), \tag{2.32}$$

where H is the Heaviside step function. The self-energy is displayed graphically in Figure 2.4. The contribution of Σ'' is an energy-independent broadening at energies higher than the phonon energy, indicating a decrease in quasiparticle lifetime due to phonon scattering. Σ' renormalizes the band dispersion at energies smaller than the phonon energy, producing the so-called "kink" in the band dispersion. The effective mass of the quasiparticle at the Fermi level is enhanced by a factor of

$$-\left.\frac{d\Sigma'(\omega)}{d\omega}\right|_{\omega=0} = \lambda. \tag{2.33}$$

We will discuss a real manifestation of this effect in $SrRuO_3$ in Chapter 10.

Table 2.1: Primary He plasma emission lines available in the VG Scienta VUV5000 lamp.

Line	Transition	Energy (eV)	Intensity (%)
He Iα	$2p\ ^1\mathrm{P}\rightarrow 1s^2\ ^1\mathrm{S}$	21.2	88
He Iβ	$3p\ ^1\mathrm{P}\rightarrow 1s^2\ ^1\mathrm{S}$	23.1	5
He IIα	$2p\ ^2\mathrm{P}\rightarrow 1s\ ^2\mathrm{S}$	40.8	5

2.7 Technical Description of the Cornell ARPES System

In this section we describe some of the technical aspects of the ARPES system designed and constructed in part by the author during the completion of his Ph.D. degree.

2.7.1 Light Sources

While the ideal light source for ARPES experiments is a synchrotron, which offers high intensity with tunable photon energy and often tunable polarization, the prohibitively large cost means that only a small number of such facilities exist in the world. As an alternative, in-lab based systems have been developed to provide ultraviolet photons, typically at only a handful of photon energies. The primary light source used at Cornell is a Scienta VUV5000 plasma discharge lamp, which uses a helium plasma to produce light in the VUV range. The primary emission lines of the He plasma source are tabulated in Table 2.1, and are chosen within the lamp using a rotatable torroidal grating. The He Iα and He IIα emission lines are most frequently used as they differ in energy by enough to probe a substantially different portion of the Brillouin Zone due to probing a different k_z (see Equation (2.6)). The He gas pressure within the plasma cavity is $\sim$ 50 mTorr, and since there are no windows which will transmit VUV light, the plasma cavity is directly connected to the photoemission chamber, typically in the 10^{-11} Torr range. This is accomplished using a series of capillaries and constrictions as well as differential pumping.

In addition to the plasma discharge lamp, the system is equipped with a Specs XR50 dual anode x-ray source, which enables samples to be characterized by x-ray photoemission spectroscopy (XPS) in addition to ARPES. The source contains both Al and Mg anodes which enables the user to select from the primary emission line from each of these elements (Al Kα = 1486.7 eV, Mg Kα = 1253.7 eV).

Finally, the system is equipped with a Xe plasma lamp which is tunable and operates in the photon energy range 5-7.5 eV. The details of the source are described in Ref. [48].

2.7.2 Electron Spectrometer

The most critical piece of equipment in a photoemission experiment is the electron spectrometer or analyzer. In this thesis, we use a VG Scienta R4000 hemispherical analyzer, although numerous other types exist [49, 50]. The R4000 is modified with a special lens system to enable the acquisition of angle-resolved data, with an acceptance window of ±15°.

The R4000 consists of multiple components, illustrated schematically in Figure 2.5. Also shown is a computer rendering of the VG Scienta R4000, the spectrometer used to collect all the data presented in this thesis. Immediately after entering the analyzer nose cone, the electron propagates through an electrostatic lens, which when operating in angular dispersive mode shapes the electron trajectories to physically separate different emission angles (see Figure 2.6). The electron then enters the energy analyzer, which consists of two concentric hemispheres biased relative to one another by a voltage ΔV. An electron propagating through such a potential will travel in a circular orbit with radius R_0, where R_0 is related to the electron kinetic energy by [49]

$$E_p = e\Delta V\left(\frac{R_1R_2}{2R_0(R_2 - R_1)}\right) \tag{2.34}$$

where R_1 and R_2 are the radii of the inner and outer hemispheres, $R_0 = (R_2 + R_1)/2$, ΔV is the voltage between the hemispheres and E_p is known as the *pass energy*. Physically E_p represents the kinetic energy for which an electron will have a radius of orbit R_0 and will therefore propagate around the hemisphere. The detector assembly consists of a multichannel plate, which amplifies the signal of the photoelectron, combined with a phosphor screen producing a visible signal which is imaged by a CCD camera.

One important metric for the quality of a spectrometer is the resolving power. For a hemispherical analyzer, the theoretical resolving power is [49]

$$\mathrm{RP} = \frac{E_p}{\Delta E} \approx \frac{2R}{s}, \tag{2.35}$$

where E_p is the pass energy, ΔE is the energy resolution, R is the mean hemisphere radius, and s is the size of the entrance aperture (slit width). For the R4000, $R = 200$ mm, and the smallest slit width $s = 0.1$ mm, yielding a resolving power of 4000, hence the name of the spectrometer. This means that the theoretical best energy resolution achievable with 1 eV pass energy and 0.1 mm slits is 0.25 meV.

From Equation (2.35) it is clear that the instrumental energy resolution depends on both the pass energy as well as the entrance slit size. In Table 2.2 we show measured values of ΔE depends on both s and E_p. This data was generated by measuring the Fermi edge of polycrystalline gold, and then fitting this data to the function

$$I(E) = [a + b(E - E_\mathrm{F})] f(E, T) * G(E, \Delta E) + c \tag{2.36}$$

which accounts for a linearly increasing density of states truncated by the Fermi-Dirac function $f(E, T)$ all convolved with a Gaussian function G of FWHM ΔE atop a constant

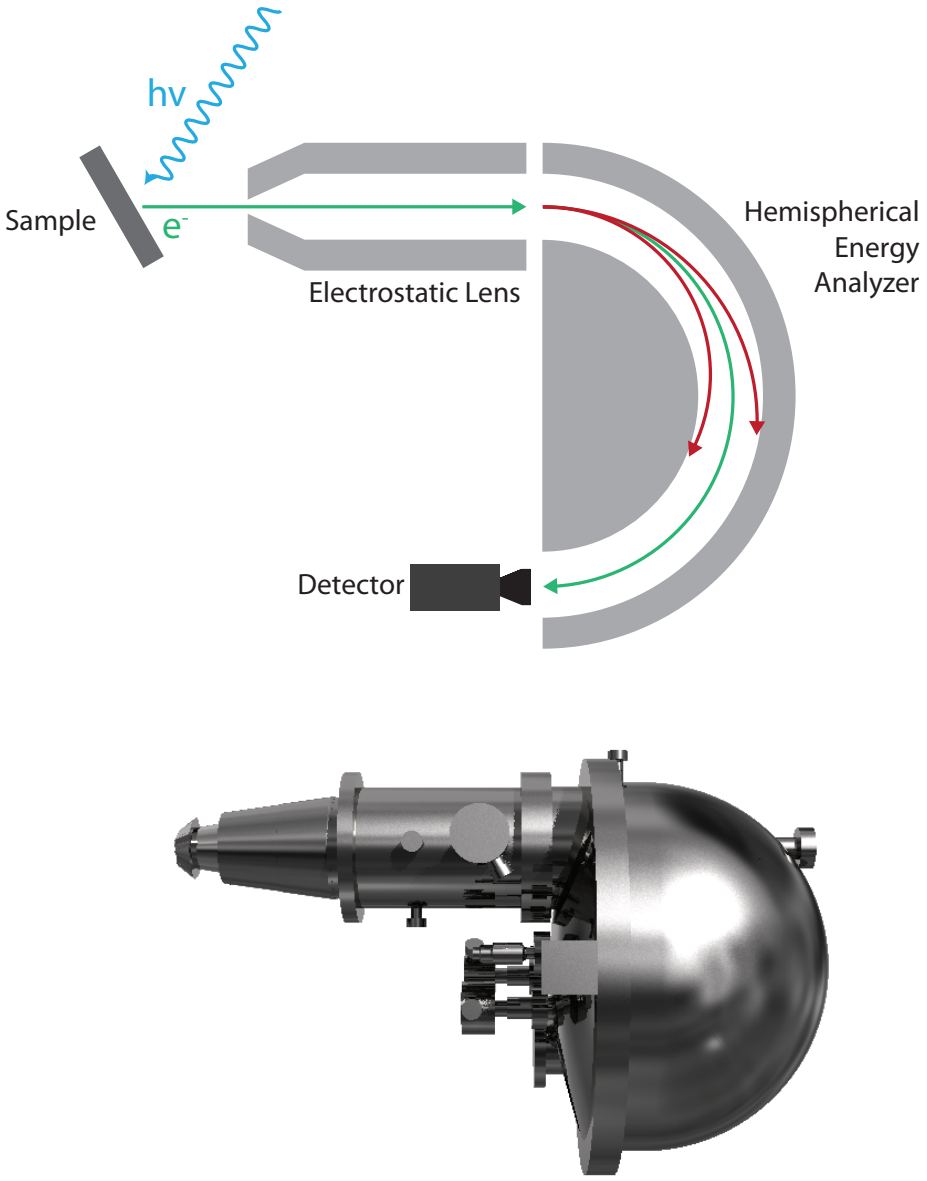

Figure 2.5: (top) Schematic of a hemispherical electron analyzer. Photoelectrons enter the analyzer and propagate through an electrostatic lens before entering the energy-selective hemisphere region. Electrons with the correct kinetic energy (green) will be detected, whereas electrons with too high/low energy (red) will not. (bottom) CAD rendering of the Scienta R4000 spectrometer.

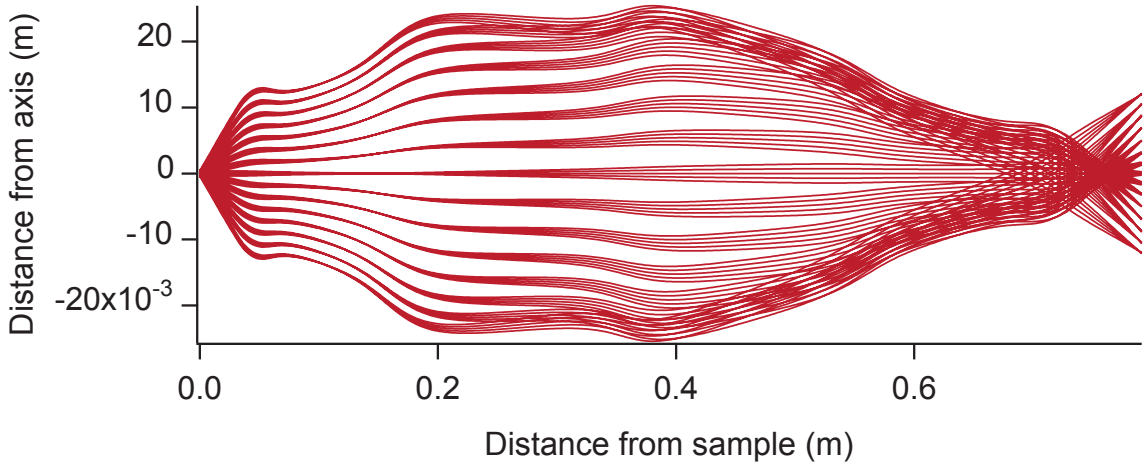

Figure 2.6: Illustration of photoelectron trajectories through an electrostatic lens operating in angle mode. Photoelectrons with the same take-off angle from the sample are mapped onto the same point on the entrance slit to the hemisphere. Reprinted with permission from Ref. [51].

Table 2.2: Measured energy resolution ΔE for various analyzer parameters. Measurements were taken on the Fermi edge of polycrystalline gold at T = 4.2 K.

	Slit Width (mm)				
E_p (eV)	0.1	0.2	0.3	0.5	0.8
1	2.87	2.94	—	—	—
2	3.35	3.5	3.85	—	—
5	—	4.88	5.75	7.63	10.92
10	—	7.17	—	—	—
20	—	12.2	—	—	40

background c. From this fitting function the Fermi level and the instrumental energy resolution ΔE are determined. An example gold Fermi edge is shown in Figure 2.7 along with the fitted data.

2.7.3 Ultra-high vacuum system

The ARPES spectrometer and light source are housed within an ultra-high vacuum (UHV) system which enables photoemission measurements to be undertaken at pressures of

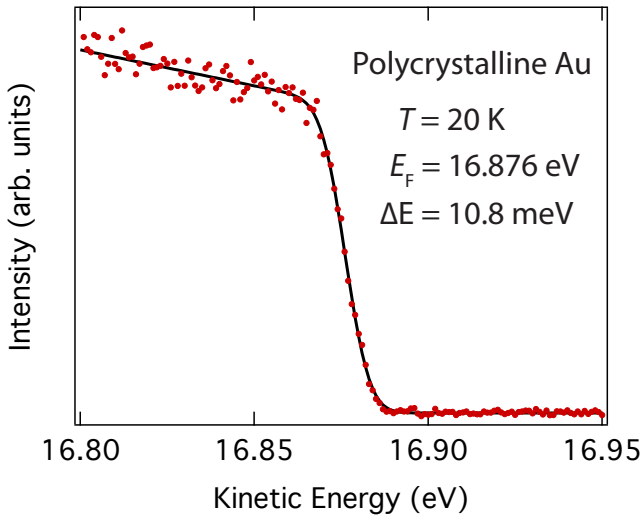

Figure 2.7: Photoemission intensity near the Fermi level for a polycrystalline gold sample, along with fitting result of Equation (2.36) demonstrating the determination of E_F and the energy resolution.

10^{-11} Torr. In Figure 2.8 we show a schematic of the entire photoemission system. The system contains a preparation chamber with a gold evaporator for Fermi level referencing described above. The chamber also contains a alkali metal evaporator for investigation of surface doping effects (see Chapter 8), a low-energy electron diffraction (LEED) system for investigating surface crystal structure (see §4.4.6), and a wobblestick for cleaving and securing samples. The sample is mounted on the end of an open flow liquid helium cryostat which performs from 4.2 K - 425 K. The sample is housed in a custom-built manipulator with three independent rotation axes described in detail elsewhere [52]. The entire manipulator and cryostat assemble is mounted on a linear translation X, Y, Z stage for adjusting sample position and moving between the preparation and measurement chambers.

The measurement chamber consists of a stainless steel chamber containing nested μ metal shields to minimize the magnetic field effects on the photoelectron trajectories. The R4000 electron spectrometer and VUV light source are housed in the lower chamber along with several pumps required to maintain UHV.

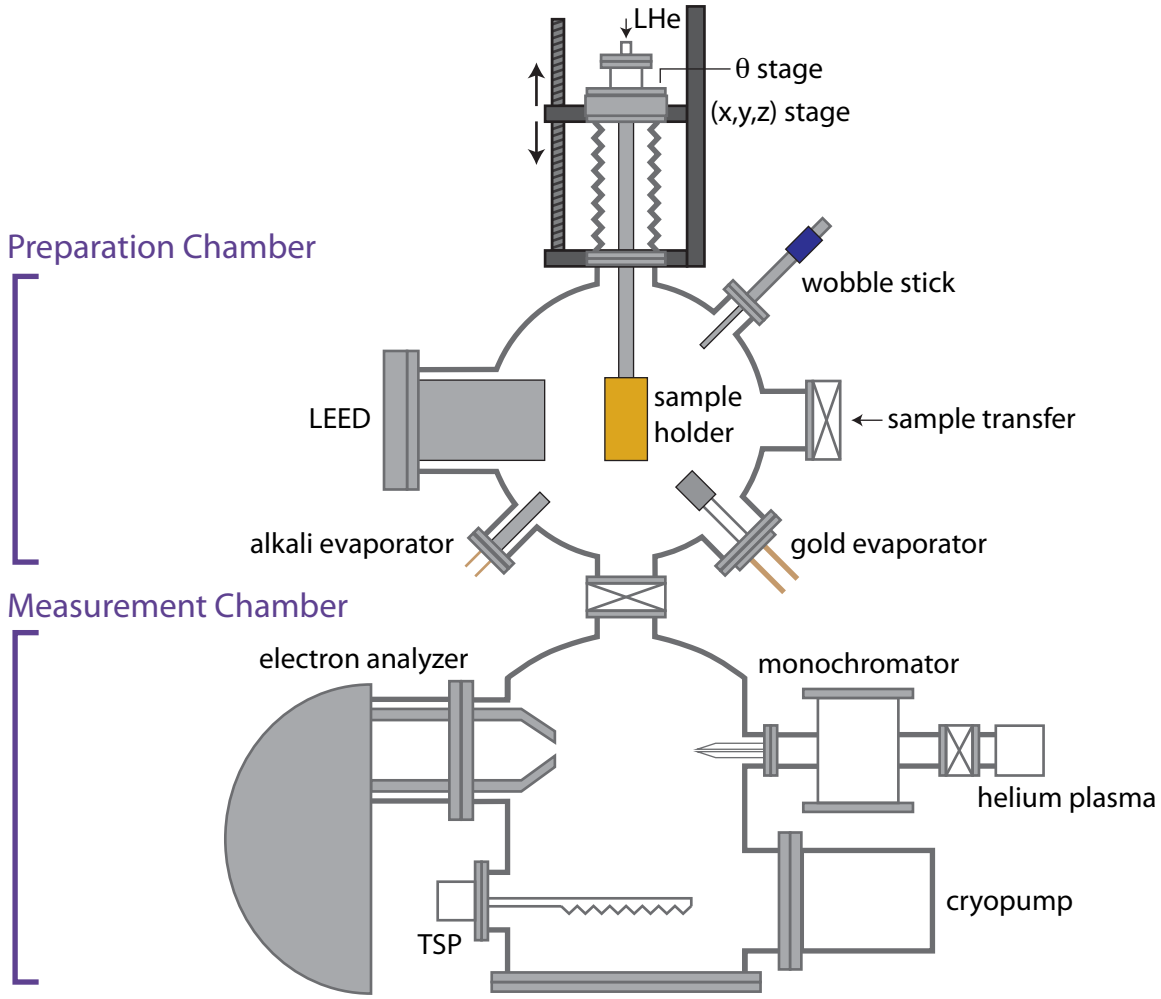

Figure 2.8: Schematic diagram of the UHV chambers composing the Cornell ARPES system. The upper chamber is used for to prepare the sample, which is subsequently transferred into the lower measurement chamber, where photoemission is performed. Schematic provided courtesy Dr. Eric Monkman.

2.8 Interfacing the ARPES system with an oxide MBE

Historically, ARPES measurements have been performed on single crystal samples which are mechanically fractured within UHV to expose a fresh, atomically clean surface. While this approach has been enormously successful for certain materials such as the high-T_c cuprates [44], it is extremely limiting. First, this approach requires samples which can be mechanically cleaved, which excludes many classes of interesting materials. More notably, the reliance on single crystal samples limits one to only study materials which are thermodynamically stable in bulk form, thereby excluding a large number of materials for which large single crystals cannot be synthesized, as well as artificial materials such as superlattices and heterostructures which simply don't exist in bulk.

It would therefore be greatly advantageous if one could study thin films grown by molecular-beam epitaxy (MBE), rather than bulk crystals. Thin films grown *in situ* have atomically pristine surface and therefore do not need to be cleaved, thus circumventing one of the aforementioned limitations of traditional photoemission measurements. Not only does this enable measurement of materials which cannot normally be cleaved, including three dimensional materials such as EuO and $SrRuO_3$, but it also enables us to study artificial heterostructures and superlattices [53], as well as other phases which are not thermodynamically stable as bulk single crystals [54], and it opens up doors to study new control parameters such as epitaxial strain [55] and dimensionality [56].

A significant obstacle necessary for interfacing these two systems is that of the sample holder. Typical photoemission measurements are done on small (~ 1 mm) crystals, to minimize heat load at cryogenic temperatures and to maximize angular resolution. The MBE, on the other hand, is designed to accept 3'' wafers. To overcome this obstacle, we developed a "piggyback" sample holder, which externally resembles the disk used to hold 3'' wafers, but which accepts a much smaller ARPES sample holder on an internal track. The outer

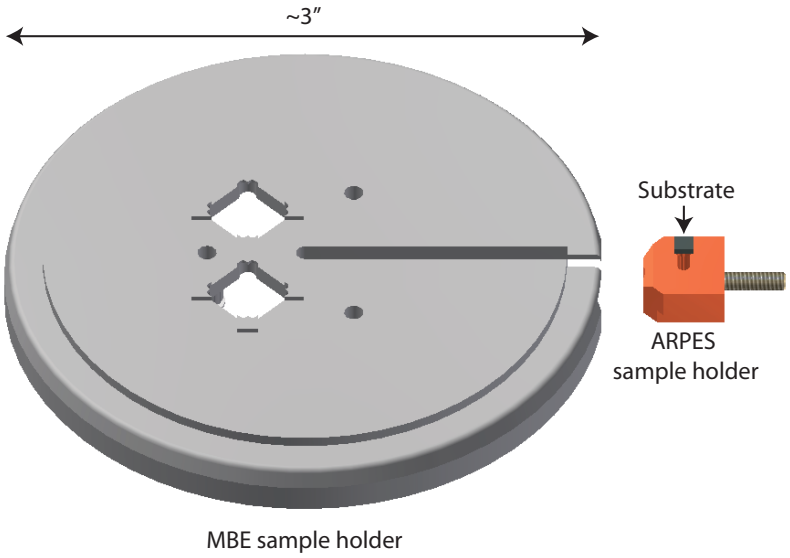

Figure 2.9: Schematic drawing of a joint MBE-ARPES sample holder. The outer disk, made of Haynes 214 is fits inside the MBE sample manipulator, which is designed to hold 3 inch semiconductor wafers. The Haynes sample holder can accommodate the Cu ARPES puck, along with two 10×10 mm companion substrates, used for *ex situ* characterization.

sample holder is composed of Haynes 214 [57], a nickel-chromium-aluminum-iron alloy which is extremely resistant to oxidation, whereas the inner ARPES sample holder is made of oxygen free high conductivity copper and titanium for good thermal conductivity and mechanical robustness, respectively. The sample holder is shown schematically in Figure 2.9. For this model, there is space to grow two 10×10 mm companion samples for additional *ex situ* characterization, such as those that will be described in Chapter 4.

Following the growth of an ARPES sample in the MBE, one must transfer the sample several meters to the photoemission system entirely within UHV, without contaminating the sample surface. This is accomplished through a series of robotically and manually controlled transfer arms. A complete rendering of the combined ARPES and MBE system, along with transfer chambers is shown schematically in Figure 2.10. The MBE-ARPES transfer system is extremely robust, and has enabled hundreds of MBE-grown samples to be measured by

ARPES since its commissioning, and the unique functionality and power of this integrated MBE and ARPES system has been highlighted recently in Ref. [58].

2.9 Conclusions

In this Chapter, we have reviewed much of the background relevant to photoemission spectroscopy, ranging from a theoretical description of the photoemission process, to more practical aspects like surface sensitivity and energy resolution determination. We have described the technical details of the ARPES system constructed in part by the author, and have highlighted the unique capability of this system to accept thin film samples from an oxide MBE system. We now move on to discuss more scientific aspects, beginning with a description of some of the background on one of the materials studied using this system: the ferromagnetic metal-insulator compound EuO.

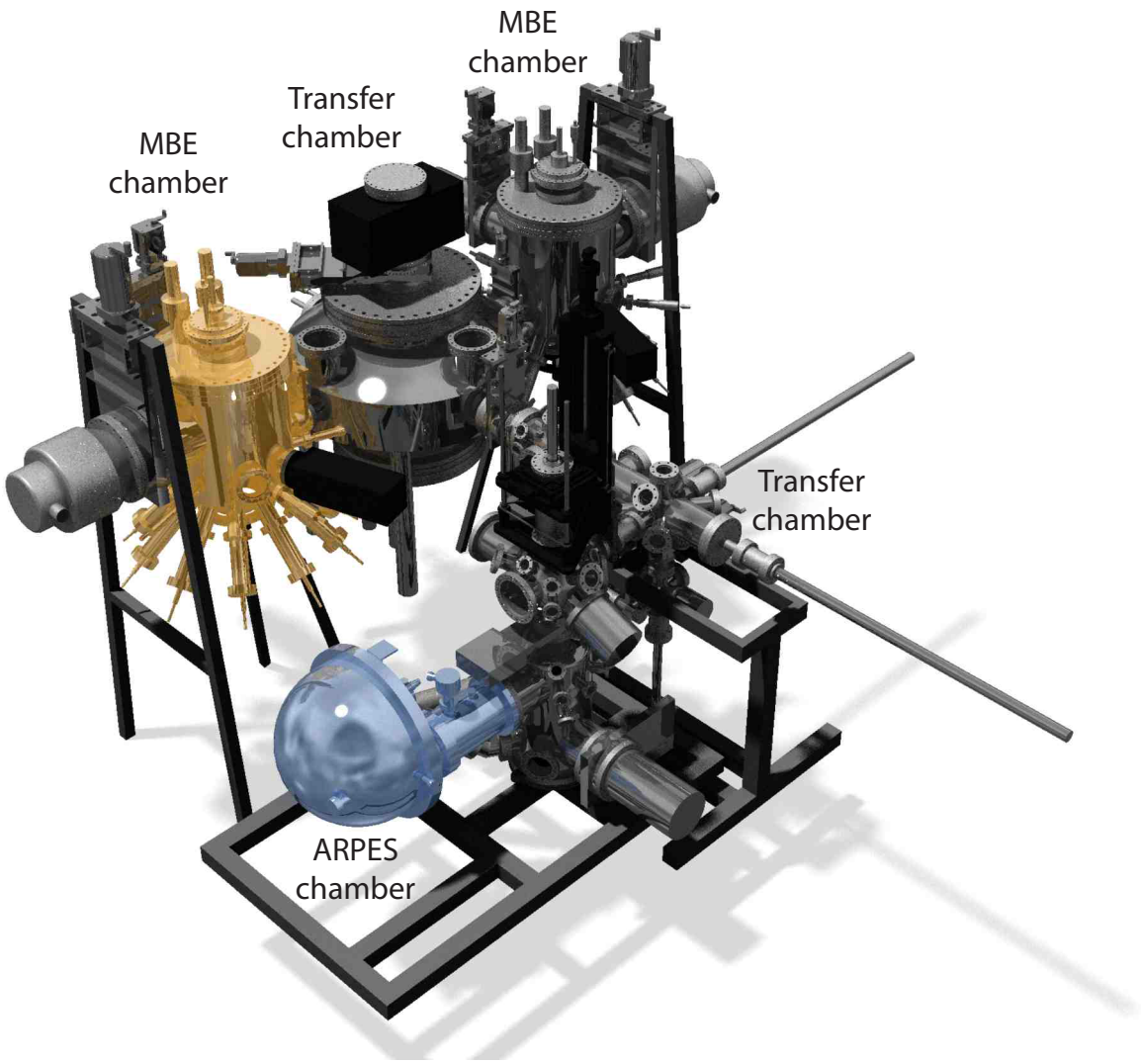

Figure 2.10: CAD rendering of the Cornell MBE and ARPES systems. Image Credit: Dr. Eric Monkman.

CHAPTER 3

Properties of Europium Oxide

For over fifty years, Europium monoxide (EuO) has drawn considerable interest as a result of its remarkable magnetic and electronic properties, which can be tuned by means of chemical doping and epitaxial stain (for a thorough review, see Refs. [59–65]). In this Chapter, we will present an introduction to the properties of EuO and review much of the relevant work performed on this compound.

3.1 Introduction

The entire series of Europium monochalcogenides (EuX, X = O, S, Se, Te) exhibit a wide variety of interesting magnetic phenomena resulting from the presence of Eu^{2+} ions, each containing 7 unpaired $4f$ electrons, aligning in the high spin state. These unpaired electrons result in a large magnetic moment on each cation lattice site, giving rise to magnetic order, ranging from ferromagnetism, multiple antiferromagnetic phases, or ferrimagnetism, depending on the chalcogenide species [59]. The majority of work has concentrated on the oxide, EuO.

EuO was discovered in 1953 by Braur in a solid solution with SrO [66]. It was subsequently isolated [67] and in 1961 was discovered to be ferromagnetic by Matthias *et al.* [68]. This was a surprising result, since the existence of an insulating ferromagnet was debated until the discovery of CrB_3 in 1960 [69], just one year prior to the discovery of ferromagnetism in EuO. The utility of such a material deals with phenomena such as ferromagnetic proximity effects,

where one desires to utilize the large magnetic field produced in close proximity to EuO without introducing an extra channel for conduction. As an example, it was recently proposed that EuO opens a spin-dependent gap in graphene when the materials are grown in close proximity to one another [70]. Thin films of EuO were recently successfully grown on graphene [71], indicating that such theoretical proposals may indeed be realized.

Aside from being a ferromagnetic insulator, much interest has been focused on the remarkable and unique transport properties of doped EuO. Since the early 1970s it has been known that, when doped, EuO undergoes a temperature-dependent metal-insulator transition (MIT), forming a metallic phase at low temperatures concomitant with the ferromagnetic transition [72, 73] . The changes in resistivity between the metallic and semiconducting phases can be quite dramatic, varying by as many as thirteen orders of magnitude [12]. The temperature-dependent resistivity data for electron-doped EuO_{1-x} is shown in Figure 3.4.

Following its initial discovery, research on EuO enjoyed a heyday during the late 1960s and 1970s, with a focus primarily on single crystals. The 1980s and 1990s were a comparatively quiet time for EuO, but more recently there has been a hugely renewed interest, this time focusing primarily on thin films. The shift toward thin films has occurred for a number of reasons, including the ability to characterize them *in situ* or protect them with a thin capping layer to prevent oxidation (see §4.3), the ability of grow very high quality films without the introduction of oxygen vacancies by growing under adsorption-controlled conditions (described in §4.2), and the ability to utilize epitaxial strain as a tool to influence the electronic and magnetic properties of EuO (§3.5). Perhaps most importantly though, is that EuO can be epitaxially integrated on mainstream semiconductors like Si, GaN, and GaAs [15, 16], opening up the possibility to use EuO as a spin injector or spin filter in spintronics applications.

In the remainder of this Chapter, we review previous work performed on EuO, framing

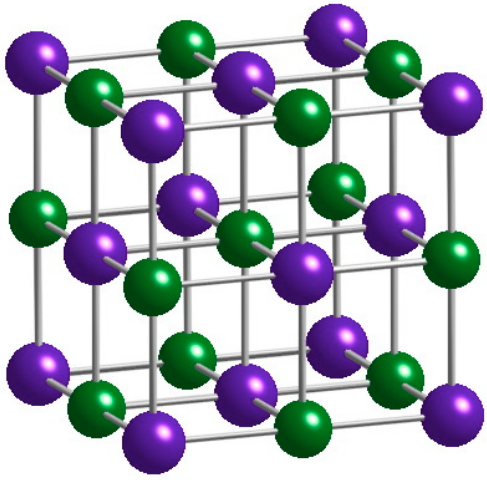

Figure 3.1: Crystal structure of EuO. The crystal is composed of a fcc lattice of Eu atoms, each octahedrally coordinated by oxygen atoms.

the historical background for the research performed in this thesis and illustrating the functional utility of this compound.

3.2 Crystalline Properties

As with all the Europium monochalcogenides, EuO crystallizes at room temperature in the rock salt NaCl structure (space group $Fm\bar{3}m$) [74]. EuO is highly ionic, composed of Eu^{2+} cations and O^{2-} anions. The lattice constant varies from $a = 5.144$ Å to 5.127 Å as the sample is cooled below 300 K to cryogenic temperatures [75]. A depiction of the EuO crystal is shown in Figure 3.1.

EuO forms solid solutions with other rock salt materials, such as SrO and BaO, allowing a systematic evolution of lattice constant and strain-balance in EuO-based superlattices. Additionally, EuO can be doped with a huge variety of cations, with the most heavily studied being La [76–79], Gd [76–78], Lu [11, 78], and Fe [79–82]. Additionally EuO supports the presence of oxygen vacancies, another avenue for electron doping.

By means of first principles calculations, Bousquet *et al.* [83] predicted that EuO is

unstable to a ferroelectric distortion with the application of epitaxial strain of a few per cent in both the tensile and compressive directions. A Si (100) substrate provides nearly +5.6% strain, which according to this calculation should be sufficient to stabilize ferroelectricity, making EuO a potential ferroelectric ferromagnet. Multiferroicity combined with integration with a mainstream semiconductor like silicon has technological implications in the field of spintronics.

3.3 Ferromagnetism

EuO was discovered to be ferromagnetic by Matthias *et al.* in 1961 [68]. The bulk Curie temperature is $T_c = 69$ K. Due to the highly localized nature of the Eu $4f$ electrons, the spin-orbit interaction is relatively strong and crystal field effects are comparatively weak. As a result, the seven $4f$ electrons align parallel according to Hund's rule, producing a net spin moment of $S = 7/2$ per Eu atom. Consequently the saturation magnetization in the ferromagnetic phase is $7\mu_B$/Eu, giving EuO the third highest magnetization off all known ferromagnets (smaller than Dysprosium and Gadolinium, but interestingly larger than pure Europium as the density of Eu in EuO is 44% larger than in Eu metal).

The $4f$ orbitals are spatially more confined as compared to the Eu $5s$ and $5p$ orbitals [84], which leads to a relatively large screening between adjacent Eu $4f$ clouds, implying that the individual magnetic moments can be considered to be completely localized. The temperature-dependent magnetization for undoped EuO, shown in Figure 3.2, very closely follows a Brillouin function derived from a mean field solution to the Heisenberg model, also consistent with a localized moment picture, which has led many to describe EuO as a close realization of an ideal Heisenberg ferromagnet. The description of completely localized spins in EuO has been questioned recently, with recent photoemission measurements [85] which resolved a prominent momentum dependence to the Eu $4f$ band structure, indicating a

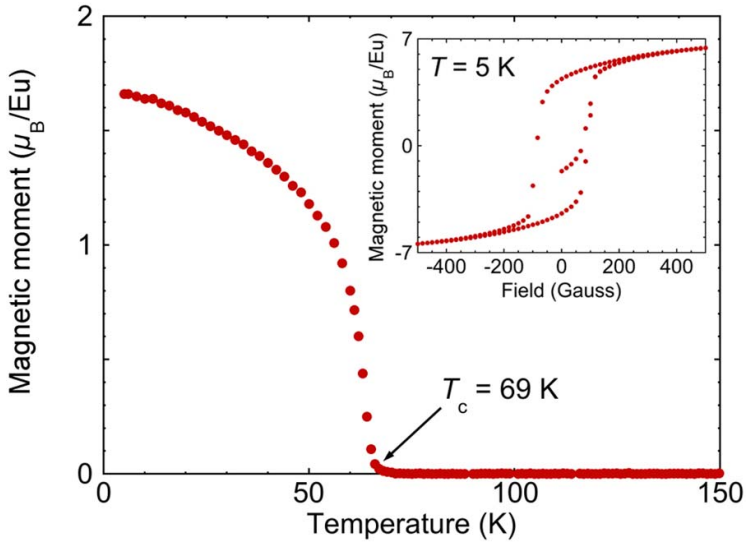

Figure 3.2: Temperature-dependent magnetization of an EuO thin film grown on (110) $YAlO_3$, measured zero field. (inset) Magnetic hysteresis curve taken at T = 5 K illustrating the saturation magnetic moment of nearly 7 μ_B/Eu atom. Reprinted with permission from Ref. [86].

substantial hybridization between adjacent $4f$ orbitals, implying the moments are not completely localized.

When EuO is doped with electrons, the ferromagnetic T_c increases, as was first shown by Shafer *et al.* [76]. The maximum T_c for doped EuO is 200 K, reported both for Fe and La-doped samples [82, 87], although such a high T_c is abnormal. One source of discrepancy stems from the fact that the ferromagnetic ordering temperature is influenced by an applied magnetic field, and not all measurements of T_c reported in the literature are performed in zero field, as discussed by Mairoser *et al.* [78]. An advantage of thin film growth is that one can reduce the presence of oxygen vacancies, thereby reducing the possibility of multiple dopant species. Under these conditions and when measured in zero applied field, T_c typically is maximized around 130 K, shown for example for $Eu_{1-x}Gd_xO$ films in Figure 3.3. Similar results have been reported by numerous groups [88–91].

In contrast to the magnetization curve (M(T)) for undoped EuO (Figure 3.2) which nearly perfectly follows a Brillouin function, the magnetization curve for doped EuO usually results

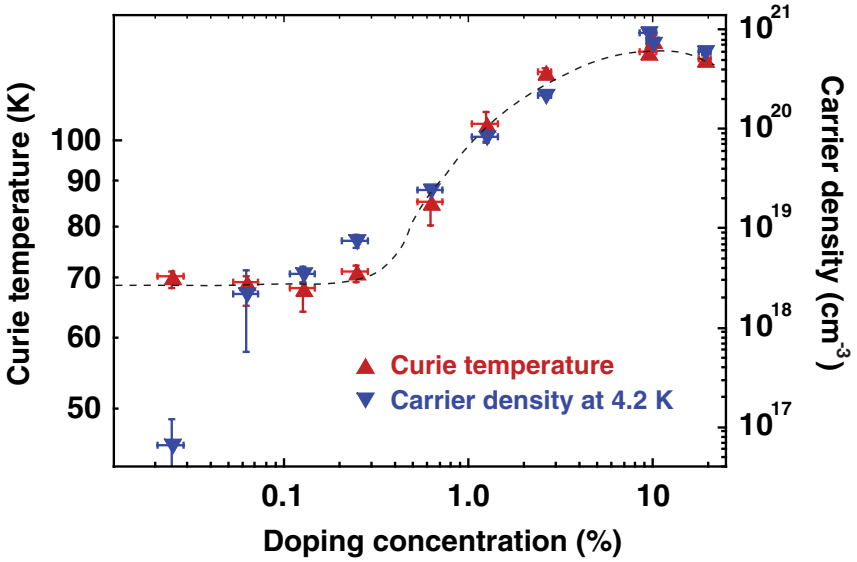

Figure 3.3: Plot of ferromagnetic T_c as a function of Gd doping for $Eu_{1-x}Gd_xO$ thin films, showing a maximum in and subsequent reduction of T_c. Reprinted with permission from Ref. [91].

in a two-domed feature (see Figure 1 in Ref. [87] for a clear comparison between M(T) for doped and undoped EuO). M(T) for doped EuO resembles the magnetization curve for undoped EuO superimposed upon a second curve with a higher T_c, regardless of whether the dopant is from cation substitution (such as $Eu_{1-x}Gd_xO$) [90, 91] or from oxygen vacancies [92, 93]. This shoulder is often interpreted in terms of a so-called bound magnetic polaron, which describes a donor electron coupled to the magnetic Eu^{2+} ions. The electron polarizes adjacent ions thereby balancing the kinetic energy cost to localization with the entropy cost pertaining to ordering the Eu spins.

Recent magnetometry measurements have shown that this additional component to the magnetization is coupled antiferromagnetically to the undoped EuO signal [94], providing evidence that this magnetic component is distinct from the normal ferromagnetic background, although the reproducibility of this result has been questioned by Montiero *et al.*, who reported muon spin rotation measurements supporting a picture of spatially uniform ferromagnetism below T_c [95]. The exact origin of this dopant-induced increase in T_c remains a contentious subject with no clear resolution to date.

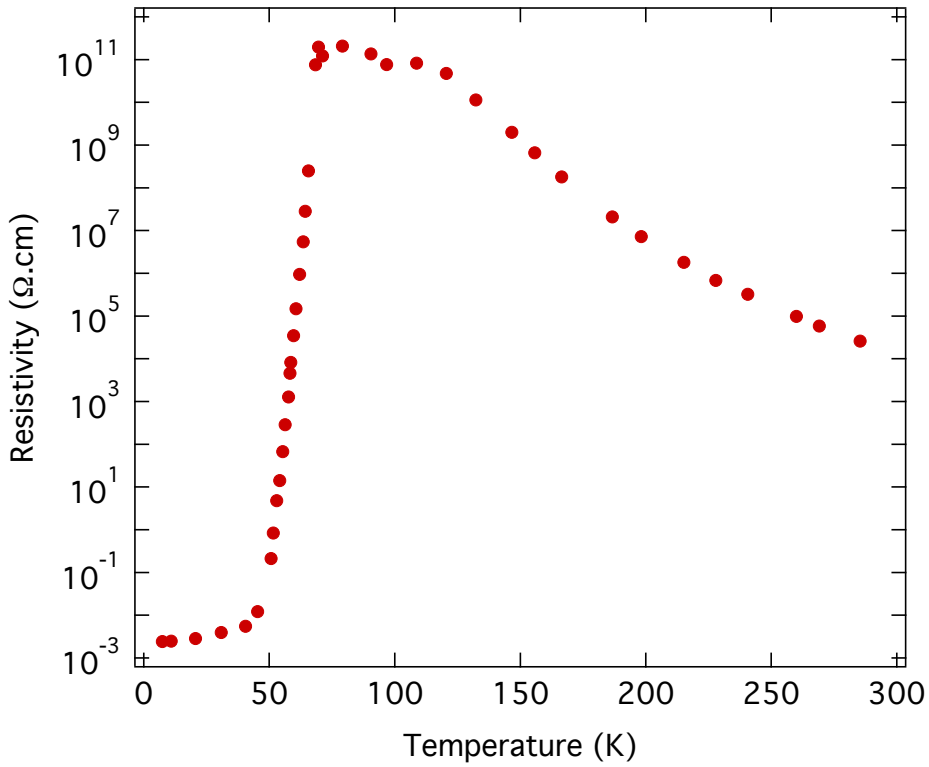

Figure 3.4: Temperature dependent electrical resistivity for a crystal of EuO_{1-x}, showing an enormous metal-insulator transition. Transport data from Ref. [13].

3.4 Metal-Insulator Transition

The second unique property of EuO is related to the transport properties in doped samples. While undoped EuO is highly insulating, doped samples significantly deviate from insulating behavior. When lightly doped with electrons , one finds that sample exhibits activated conduction in the paramagnetic phase (activation gap $\varepsilon_g \sim 0.3$ eV for a sample doped with oxygen vacancies [13]), but when cooled below its ferromagnetic T_c, the system exhibits a precipitous drop in resistivity (as many as 13 orders of magnitude) as shown in Figure 3.4.

The metallic phase in doped EuO below T_c has been proposed to arise from the exchange splitting of the EuO conduction band [73]. When the system orders ferromagnetically, the conduction band splits into two spin populations, and the majority carrier band dips below E_F, forming a metal. For small enough doping, the minority band should therefore be

completely unoccupied, implying that EuO is a half-metal, with fully spin polarized charge carriers.

While the presence of completely spin polarized carriers was postulated from transport measurements in the 1970s [72, 96], the first direct experimental evidence of the accuracy of this picture was provided by Steeneken *et al.* in 2002 [97]. Using spin-resolved oxygen K edge x-ray absorption spectroscopy it was shown by measuring the unoccupied density of states that the EuO conduction band splits into two spin populations, separated in energy by approximately 0.6 eV below T_c. If this value is taken as the ferromagnetic exchange splitting, then the majority spin conduction band would be expected to be lowered in energy by half this value, 0.3 eV, consistent with the activation gap observed in transport measurements, described above. Further to this hypothesis of spin polarized charge carriers in doped EuO, Andreev reflection measurements were carried out first by Schmehl *et al.* [15] and subsequently by others [11] to quantitatively characterize the degree of spin polarization. Through these measurements it was shown that the polarization P of the EuO charge carriers is as high as 96%, implying that EuO is nearly a perfect half-metal.

Half-metals such as EuO are highly desirable in the field of spintronics since they can potentially be used as injectors and filters [17, 98]. A necessary requirement is that the material must be integrable with other device components. The epitaxial growth of EuO on these semiconductor components has been shown previously [15, 99], though a substantial obstacle still to be overcome is the formation of silicides at the EuO/Si interface [100].

Due to its large metal-insulator transition, and its close relationship with ferromagnetism, EuO exhibits large colossal magnetoresistance (CMR) effects. CMR was first discovered in EuO in single crystals by Shapira *et al.* [14, 101]. Near T_c with the application of an external magnetic field, one can induce a change in resistivity of $\Delta\rho/\rho > 10^6$, even larger than what are seen in the archetypical CMR system $La_{1-x}Sr_xMnO_3$ (LSMO). CMR changes of up to five orders of magnitude have been observed in thin films [15].

3.5 Effect of Strain

Lattice strain has been known to prominently effect the magnetic and electronic properties in EuO. Hydrostatic strain applied to single crystals have been shown to increase T_c from 69 K to as high as 200 K at a pressure of 20 GPa [102]. At higher pressures, T_c begins to decrease again. Simultaneously, the appearance of a drude peak in the optical reflectivity [103] and change in the high temperature resistivity [104] indicate that at this pressure the system undergoes a pressure induced metal-insulator transition. First principles calculations [105] have reproduced the hydrostatic pressure-induced increase in T_c and indicate that the metal-insulator transition is a result of the closing of the Eu $4f$-$5d$ band gap, which would generate a mixed-valence state, which is not tractable with density functional theory.

A potentially more useful approach is to use epitaxial strain on thin films. By growing EuO epitaxially on substrates with a lattice parameter that is different from that of EuO, the film can be strained biaxially. For an excellent review of the various substrates and thin film growth parameters used in the literature for EuO, the reader is directed to Ref. [106].

Of all the commercially available substrates (001) EuO is most closely lattice matched to yttria-stabilized zirconia (YSZ), a ZrO_2 crystal with a tetragonal phase stabilized through the introduction of $\sim 9.5\%$ Y_2O_3. The YSZ lattice constant of $a = 5.142$ Å amounts to an in-plane compressive strain to EuO of $< 0.5\%$ at room temperature, making YSZ an ideal substrate for EuO structurally. Nevertheless YSZ is a well-known oxygen ion conductor [107], which has negative consequences for the stability of the Eu^{2+} oxidation state in EuO. For EuO grown on YSZ without formation of higher order Eu oxidation states, the surface of YSZ must either be treated through annealing in an oxygen environment [108] or a buffer layer (e.g., SrO) must be introduced to prevent migration of the mobile oxygen from the substrate into the film.

For these reasons all of the films used in this dissertation were grown on the orthorhombic perovskite $YAlO_3$. (001) EuO grows on the (110) face of $YAlO_3$ with a lattice mismatch

amounting to ~ 2% tensile strain. The growth of EuO on non-commercially available substrates with closer lattice match such as (110) $LuAlO_3$ (~ 1% tensile strain) [109] and diamond (~ 2% compressive strain) [110] has also been demonstrated recently.

3.6 Conclusions

In this Chapter, we have reviewed the historical development and primary electronic and magnetic properties of EuO. These properties include the existence of ferromagnetism in an insulator, which is highly sensitive to parameters such as doping and strain. Furthermore, the large spin-polarized metal-insulator transition makes EuO ideally suited for applications in the field of spintronics. Consequently, EuO has attracted great interest in being utilized in numerous heterostructures and devices which leverage these properties. For example, in addition to its potential multiferroicity and spin injection described above, it has been proposed that a spin-polarized two-dimensional electron gas is supported at the heterointerface of $LaAlO_3$ and EuO [111], similar to the oft-cited $LaAlO_3$ on $SrTiO_3$ system. Aside from the obvious advantages of spin-polarization, LAO/EuO does not involve $SrTiO_3$ which is known to produce unclear results due to its propensity toward oxygen vacancy formation. EuO has also attracted interest in the field of non-trivial band topologies. Recent theoretical predictions indicate that CdO/EuO superlattices and quantum wells could exhibit topologically non-trivial surface states [112]. Furthermore, when grown in conjunction with existing known topological insulators such as Bi_2Se_3, EuO's sister compound EuS has been shown to induce significant exchange coupling effects in topological surface states [113].

Yet despite this interest in utilizing EuO, and long history of work studying it, there has been no direct experimental evidence of the momentum-resolved electronic structure through the metal-insulator transition and no clear understanding of the nature of the dopant states above and below T_c, and how this electronic structure evolves as a function of

doping. This information is critical to an accurate description of the charge carrier dynamics in EuO, yet has remained out of reach until recently due to experimental difficulties. The combination of thin film synthesis used in conjunction with a momentum-resolved probe such as ARPES represents and ideal tool to answer these questions, as will be shown in the next several Chapters of this thesis.

CHAPTER 4

Growth of EuO Thin Films by Molecular-Beam Epitaxy

In this Chapter, we will discuss some of the general aspects of thin film growth by MBE, placing particular emphasis on the points most relevant for growing EuO. We will also discuss many of the primary characterization tools used to assess film quality and stoichiometry.

4.1 General Principles of MBE

Molecular-beam epitaxy, or MBE, is a technique for depositing epitaxial thin films on single crystal substrates. Colloquially referred to as "atomic spray painting," MBE involves the growth of films by depositing elemental constituents in doses to achieve the desired stoichiometry. Elemental constituents are generated by thermal evaporation of high purity sources in ultra-high vacuum (UHV). When sources are heated to the point where there is a substantial vapor pressure, source material travels ballistically toward the substrate in atomic or molecular beams. The use of thermal evaporation in UHV, combined with the precise stoichiometric control and atomically-resolved layer-by-layer growth achieved using individual shuttered elemental sources enables MBE grown films and heterostructures to be of extremely high quality with minimal defects.

MBE was developed by J.R. Arthur and A.Y. Cho at Bell Laboratories in the 1960s and was first used with the growth of semiconductors such as GaAs and $Al_xGa_{1-x}As$ [114], and subsequently for the growth of high quality metals and insulators. More recently, MBE was extended to the growth of complex oxides [23]. Through the use of a gaseous oxygen source, one can react oxygen with elemental sources at the substrate to deposit an oxide thin film.

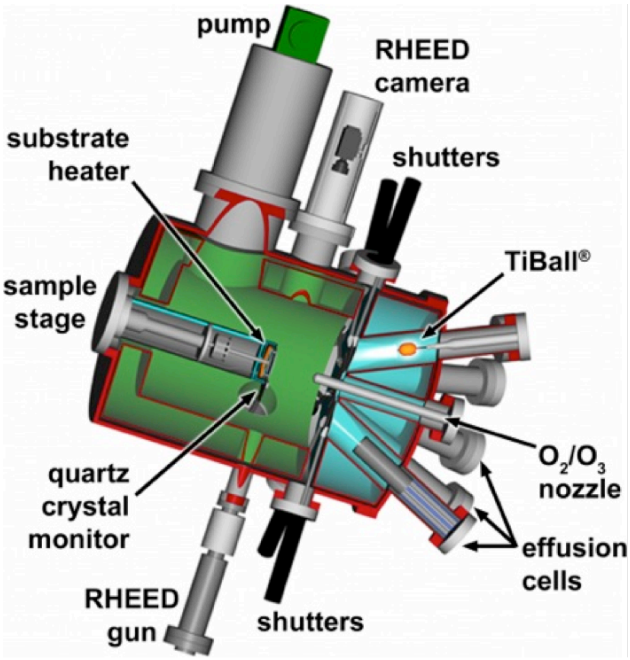

Figure 4.1: Schematic of an oxide MBE system, illustrating the relevant functional components for deposition and monitoring during thin film growth. Reprinted with permission from Ref. [23].

The use of gaseous sources is therefore referred to as "reactive MBE." The first example of an oxide being grown by MBE dates to 1985 [115], and the growth of oxides has subsequently flourished into an active research field.

An MBE chamber is shown schematically in Figure 4.1. It consists of a UHV chamber, combined with a UHV pump, elemental sources, and growth monitoring apparatuses. The chamber is pumped by a combination of devices, including a cryopump, turbo molecular pump, and the source material itself. Additionally the chamber is lined with a cryoshroud which can be filled with liquid nitrogen, enabling the user to achieve extremely low pressures ($10^{-9} - 10^{-10}$ Torr scale).

Metallic source material is evaporated from a Knudsen effusion cell, which consists of a crucible surrounded by a heating element. For materials with very low vapor pressures requiring growth temperatures in excess of 2000 °C, an electron beam evaporator can be used. The source material flux (typically # atoms/area/time) must be calibrated very accurately to

grow high quality films. Typically this involves a multi-stage process. The first tool to calibrate flux is a quartz crystal microbalance (QCM). The general principle of a QCM is that it uses a piece of piezoelectric quartz which resonates at a particular frequency, which changes as the mass of the crystal changes. It is therefore sensitive to small amounts of material deposited on top of it. While the QCM provides an good starting point for flux calibration, its accuracy ($\sim 5\%$) is typically insufficient for the high precision growth of MBE. Usually QCM calibration is used as a starting point for more accurate calibrations such as oscillations in the reflection high-energy electron diffraction (RHEED) intensity.

RHEED is a surface sensitive analysis technique, whereby a high energy (~10 keV) beam of electrons diffract off the surface of a sample at a grazing angle ($\sim 5°$). The resulting diffraction pattern can be monitored during growth in real time. As material is deposited on a crystalline surface, the intensity of the monitored diffraction pattern changes as a result of the sequential roughening and completion of individual atomic layers and also as the surface material changes for systems with more than one layer. The oscillation in the diffraction intensity can be used to further calibrate both the monolayer dosage as well as relative amounts of individual elements [116, 117]. It should be noted that oscillations are not present for all materials, but when this method of calibration is used, it can result in source fluxes determined to better than 1% accuracy, which can be essential for materials requiring extremely high precision.

4.2 Growth of EuO thin films by MBE

The most straightforward way of thinking about thin film growth by MBE is in a flux matched growth mode. With flux matched growth, the flux of each individual source is calibrated and adjusted to provide doses in stoichiometric ratios to the desired material. This can be done in so-called codeposition, where all materials are provided simultaneously,

or in a shuttered growth mode, which can produce layered structures which are not thermodynamically favored. The growth of EuO by a flux matched technique is possible although difficult. To illustrate this, we consider the Eu↔O binary phase diagram generate for the growth of bulk crystals [118]. This phase diagram, shown in Figure 4.2, illustrates that EuO forms only when Eu and O are supplied in nearly 1:1 doses. Deviating slightly to the O rich side of the phase diagram results in higher oxidation states such as Eu_3O_4, whereas the Eu rich side results in Eu metal precipitates. While this phase diagram is not strictly applicable to the growth of thin films, it illustrates the expected difficulty in controlling stoichiometry when growing flux matched EuO.

When high growth temperatures can be permitted, it is advantageous to make use of the adsorption-controlled growth mode. Adsorption-controlled growth, or sometimes referred to as molecular distillation, makes use of the extremely high vapor pressures of some elemental components. The technique was first popularized with the growth of GaAs in 1968 [119]. When the vapor pressure of a source component (As in the case of GaAs) is much higher than the vapor pressure of the resulting film, growth can be achieved in a regime where the substrate temperature is high enough to prevent As deposition, but which permits the

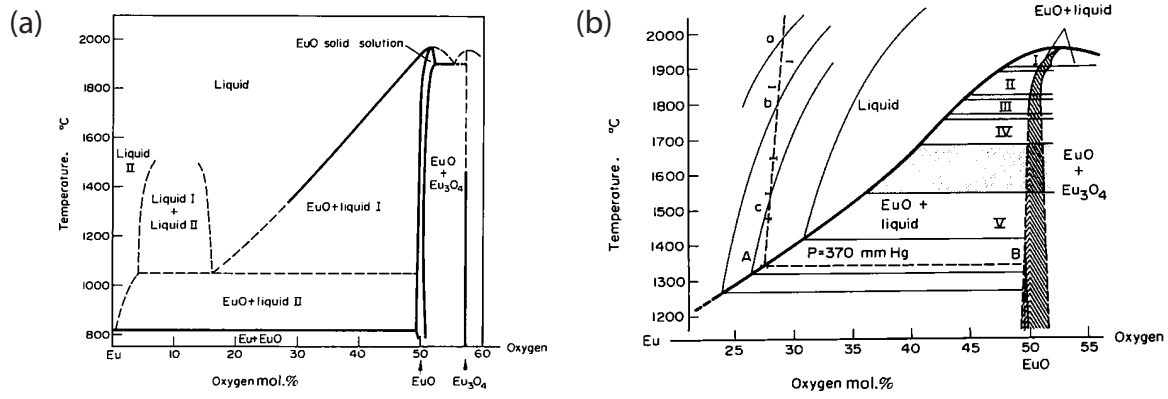

Figure 4.2: Eu-O Phase diagram. (a) Full range of the Europium rich phase diagram. (b) Phase diagram near perfect stoichiometry, highlighting the region in which EuO forms. Reprinted with permission from Ref. [118].

deposition of GaAs. In this case, an overpressure of As is supplied and Ga is used as the rate limiting component.

The first evidence for adsorption-controlled growth of EuO was provided in 2002 by P.G. Steeneken [120] who observed that metallic conductivity was suppressed when the growth temperature of EuO was raised. For EuO, substrate temperatures above $\sim 280^{\circ}$C [92] cause pure Eu metal to desorb rapidly, but EuO will remain. Thus, if an overpressure of Eu is supplied, only EuO will form, with the growth rate limited by the oxygen partial pressure. Proof of adsorption controlled growth was subsequently provided by Ott [89], Ulbricht [86], and Sutarto [108]. The use of adsorption-controlled growth provides films with high crystallinity and reduces the likelihood of forming oxygen vacancies, allowing one to controllably dope the sample with a single dopant species. All of the EuO films characterized in this thesis were grown by Alexander Melville in the adsorption-controlled regime.

4.3 Obstacles in Characterization of EuO

One of the major obstacles in studying EuO is its extreme sensitivity to oxidation. In the presence of excess oxygen, Eu forms higher oxidation states such as Eu_3O_4 and Eu_2O_3 [121]. While these higher order oxides usually self-passivate [122], for thin film samples, often the entire film can be consumed before such passivation occurs. As a result, any *ex situ* characterization of EuO thin films requires a protective capping layer. Prior works have utilized a number of capping materials such as amorphous Si [11, 78, 91], polycrystalline Al [99, 108], and Al_2O_3 [17]. For all of the data presented in this thesis, films were capped with 20 nm amorphous Silicon.

As an example of the extreme sensitivity EuO has to oxidation, we show in Figure 4.3 an image of an $(EuO)_1/(BaO)_1$ superlattice capped with 50 nm amorphous $LaAlO_3$ after its

Figure 4.3: Image of 30 nm $(EuO)_1/(BaO)_1$ superlattice capped with 50 nm amorphous $LaAlO_3$ grown on a 3″ Si wafer. The film is showing significant signs of degradation despite the protective capping layer. Image credit: Dr. Rainer Held.

removal from the growth chamber. Despite the protective capping layer the film is showing severe signs of degradation.

Even when an EuO sample is contained within ultra-high vacuum, surface degradation still occurs at a non-negligible rate. In Figure 4.4, we show x-ray photoemission spectra (XPS) of the Eu 3*d* multiplet which clearly shows an increasing ratio of Eu^{3+}/Eu^{2+} over time. While the presence of a small Eu^{3+} signal is expected due to final state effects [123], the time evolution of this spectrum undeniably proves the existence of surface aging even in UHV.

This rapid in-vacuum aging has significant effects on the spectra near E_F in ARPES measurements as well. As such, great care needs to be taken, especially when cycling temperatures to ensure that the acquired spectra are truly representative of EuO.

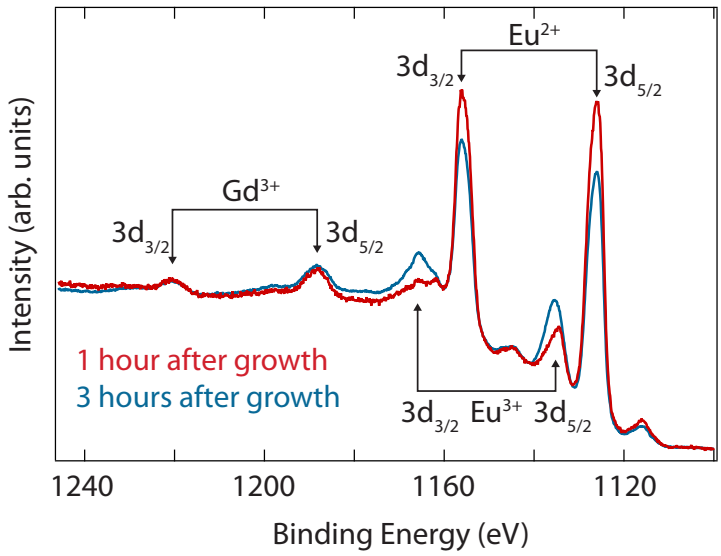

Figure 4.4: XPS spectra of the Eu and Gd 3*d* multiplets. Gd is present in the 3+ oxidation state, whereas over time there is a shift from Eu^{2+} to Eu^{3+}, presumably due to surface aging. For the duration of the measurement, the chamber pressure was 2×10^{-9} Torr.

4.4 Characterization techniques of EuO thin films

During and following the growth of EuO films, a number of experimental probes are used to characterize the resulting films. These techniques are described below.

4.4.1 RHEED

RHEED was described earlier in this Chapter as a means to accurately calibrate source flux. Additionally, however, during and after film growth, RHEED is used to characterize film surface quality. Here, RHEED was used to monitor the growth of EuO films grown immediately before or after those used in this thesis. Exemplary RHEED images are shown in Figure 4.5(a) for a bare $YAlO_3$ substrate and in Figure 4.5(b) after the deposition of a 35 nm thick $Eu_{0.95}Gd_{0.05}O$ film. The RHEED shows no evidence of second phases or excessive surface roughness.

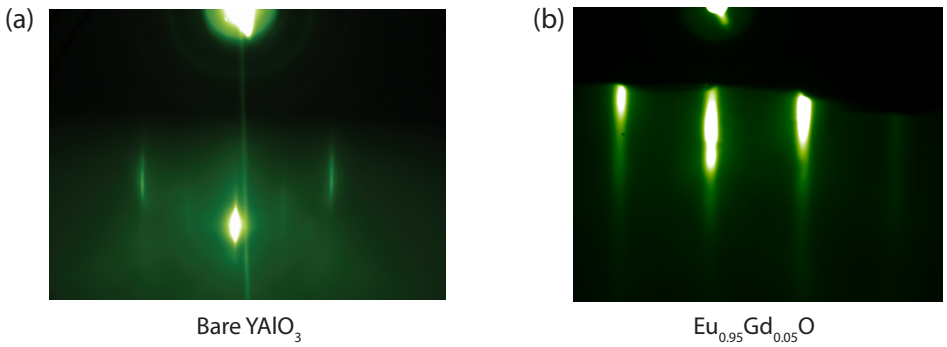

Figure 4.5: RHEED pattern (a) for a bare $YAlO_3$ substrate and (b) after the deposition of 35 nm $Eu_{0.95}Gd_{0.05}O$. Reproduced with permission from Ref. [124].

4.4.2 X-ray Diffraction

Companion films capped with a amorphous silicon to prevent oxidation (see §4.3) were characterized by x-ray diffraction. $\theta - 2\theta$ scans are shown in Figure 4.6 for samples with a measured Gd content of $x = 0.007$, 0.013, and 0.049. All films are (001) oriented and show no evidence of extra phases.

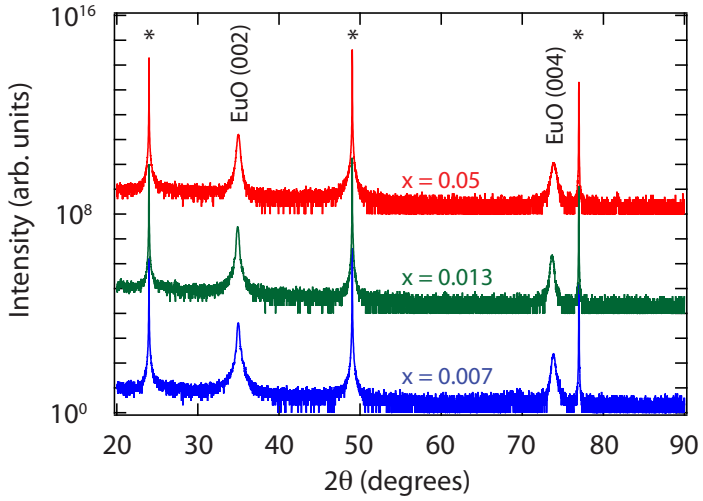

Figure 4.6: X-ray diffraction $\theta - 2\theta$ scans for $Eu_{1-x}Gd_xO$ films with $x = 0.007$, 0.013, and 0.05, showing phase pure, oriented (001) films. $YAlO_3$ substrate peaks are marked with an asterisk (*). Reproduced with permission from Ref. [124]

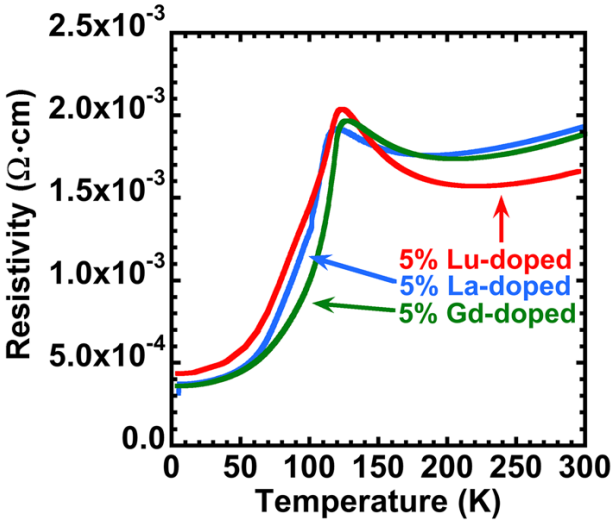

Figure 4.7: Temperature-dependent resistivity for $Eu_{0.95}R_{0.05}O$, where R = La, Gd, Lu. Reprinted with permission from Ref. [11].

4.4.3 Electrical Transport

Due to the extreme sensitivity of EuO to oxidation, conventional *ex situ* transport measurements cannot be performed. Instead, films are capped with a protective insulating layer, typically 20 nm amorphous Si, and then electrical contacts are made using photolithography and a combination of *in situ* ion etching and sputter deposition [91]. Exemplary resistivity measurements for doped EuO are shown in Figure 4.7.

4.4.4 X-ray absorption spectroscopy

X-ray absorption spectroscopy (XAS) was used to determine the Gd content x in a companion series of $Eu_{1-x}Gd_xO$ films. XAS was performed on the Eu and Gd $M_{4,5}$ edges between 1100 eV and 1245 eV at the SGM beamline at the Canadian Light Source. The Gd content was determined by comparing the integrated intensities of the Gd $M_{4,5}$ edges versus the Eu $M_{4,5}$ edges, following the method described by Sutarto *et al.* [90]. Measurements were performed using total electron yield (TEY) and inverse partial fluorescence yield (IPFY) with samples

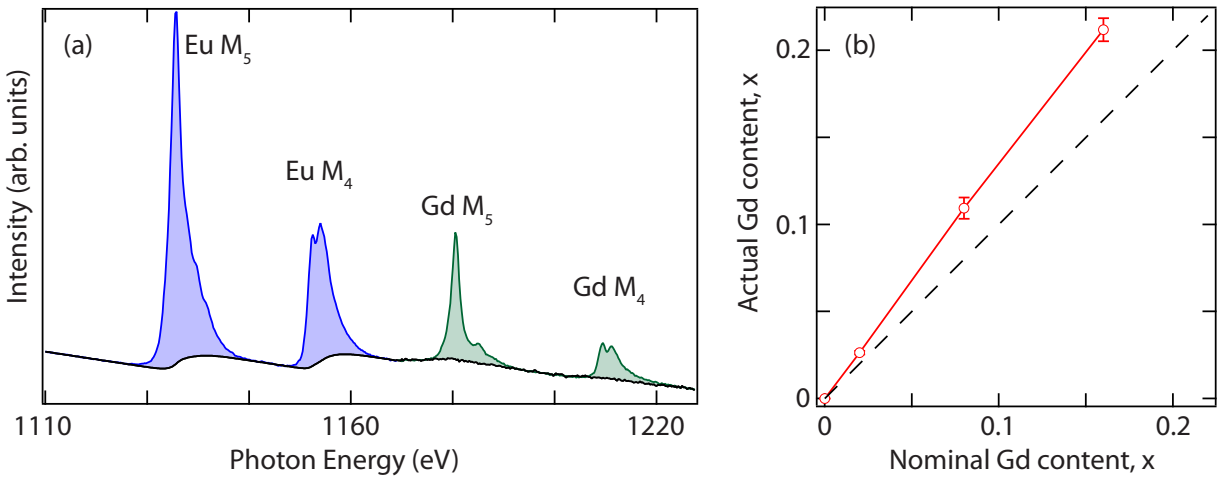

Figure 4.8: (a) Exemplary XAS spectrum taken in total electron yield (TEY) from a nominally 16% Gd-doped EuO sample. The blue (green) shaded area representing the integrated intensity of the Eu (Gd), respectively, and the background shown as a solid black line. (b) Extracted doping values x as a function of nominal doping values for a series of $Eu_{1-x}Gd_xO$ films. Reproduced with permission from Ref. [124].

grounded through the contacts. To perform our analysis, we subtracted off a linear sloping background (from the Si capping layer) and the extended x-ray absorption fine structure (EXAFS), and used a simple empirical Shirley background to account for the increased absorption after each edge. An example spectrum taken in TEY mode is shown in Figure 4.8. The extracted doping values are tabulated in Table 4.1.

As IPFY is a relatively newly developed technique [125, 126], we will briefly describe it here and discuss why it is useful for studying EuO. With IPFY, one monitors the non-resonant emission from a transition which is lower in energy than the adsorption line being resonantly excited. Given incident photons of energy E_i and intensity $I_0(E_i)$, the fluorescence intensity of photons with energy E_f is given by

$$\frac{I(E_i, E_f)}{I_0(E_i)} = C \sum_X \int_0^\infty \omega_X(E_i, E_f) \frac{\mu_X(E_i)}{\sin\alpha} e^{-\left(\frac{\mu(E_i)}{\sin\alpha} + \frac{\mu(E_f)}{\sin\beta}\right)z} dz, \tag{4.1}$$

where $C = \eta(E_f)\Omega/4\pi$ and

X = specific emission line from a specific element
ω_X = probability that a photon with energy E_i will induce fluorescence of a photon from element/line X and energy E_f
μ_X = Contribution of atom/line X to total absorption coefficient
α = angle between incident photon direction and sample plane
β = angle between fluoresced photon direction and sample plane
$\mu(E)$ = total linear absorption coefficient at energy E
$\eta(E)$ = fluorescence detector efficiency at energy E.

For a semi-infinite, homogeneous sample, Equation (4.1) is easily evaluated:

$$\frac{I(E_i, E_f)}{I_0(E_i)} = C \sum_X \frac{\omega_X(E_i, E_f)\mu_X(E_i)}{\mu(E_i) + \mu(E_f)\frac{\sin\alpha}{\sin\beta}}. \tag{4.2}$$

With the use of an energy sensitive detector, a specific emission line Y can be selected, eliminating the sum over X in Equation (4.2). If this emission line is non-resonant, then it is reasonable to assume that ω_Y and μ_Y are both independent of the incident photon energy E_i. In this case Equation (4.2) simplifies to

$$\text{PFY} \approx C \frac{\omega_Y(E_f)\mu_Y}{\mu(E_i) + \mu(E_f)\frac{\sin\alpha}{\sin\beta}}. \tag{4.3}$$

Inverting Equation (4.3), we arrive at the inverse partial fluorescence yield (IPFY):

$$\text{IPFY} = \frac{I_0(E_i)}{I(E_i, E_f)} = A(\mu(E_i) + B), \tag{4.4}$$

with $A = 1/C\omega_Y(E_f)\mu_Y$ and $B = \mu(E_f)\frac{\sin\alpha}{\sin\beta}$. Thus, the IPFY measured on a non-resonant emission line is proportional to the total linear absorption coefficient.

For EuO, we have measured the x-ray fluorescence while scanning the indident photon energy through the Eu and Gd $M_{4,5}$ edges, shown in Figure 4.9(a). In Figure 4.9(b) we show the fluorescence spectrum acquired using an energy sensitive silicon drift detector. In Figure

4.9(c) we show the O K_α partial fluorescence yield (PFY) and in 4.9(d) we show the inverse of this, the IPFY, which closely resembles the TEY measurements in Figure 4.8. Also in 4.9(d), we show the total fluorescence yield (TFY). Clearly there are large inaccuracies in the TFY data which result from self-absorption effects [127] from the dense Eu atoms. Using the extracted IPFY spectra, we compute the Gd content x using the same analysis described for the TEY data above. The extracted doping values are tabulated in Table 4.1. To corroborate these measurements, a third independent measurement of another companion series of films was performed using Prompt Gamma Activation Analysis (PGAA)[1] with results also included in Table 4.1.

The IPFY technique has some experimental advantages specific to EuO samples due to the necessity of the protective capping layer. Since TEY relies on the emission of electrons from the sample surface and subsequent replenishment of these electrons through a grounded connection, the measurements reported here required electrical contacts to be patterned through the insulating Silicon layer. For samples with thicker metallic capping layers, the number of electrons extracted from the EuO film is extremely small and TEY measurements cannot be performed. In these cases, IPFY measurements would be virtually unaffected.

While the TEY and IPFY-derived values are in good agreement, they can be improved by accounting for the finite thickness of the EuO films (an assumption which was made in deriving Equation (4.2) from (4.1)). Such an analysis is beyond the scope of this thesis, however. For the remainder of this thesis, we use the TEY measurements to calibrate the Gd content in our films. For instances where other dopants (such as La and Lu) are used, we state the nominal doping calibrated by quartz crystal microbalance, since no XAS calibration for these film has been carried out to date.

In addition to quantitative determination of dopant concentration, our XAS measurements also yield information regarding oxidation states. By comparing with existing spectra for

[1]PGAA measurements performed by L. Canella, Universität München.

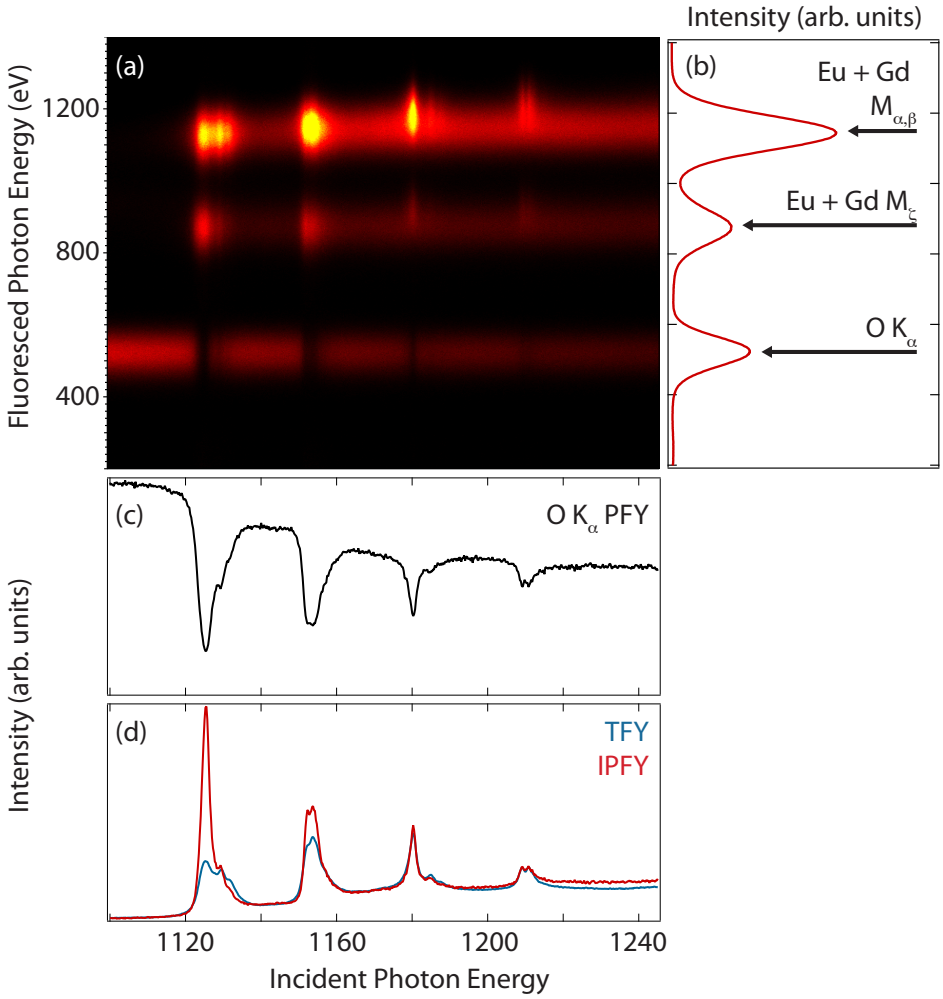

Figure 4.9: (a) XAS data for an $Eu_{1-x}Gd_xO$ film taken with an energy dispersive silicon drift detector. (b) Total emission spectrum, integrated over an incident photon energy of 1100-1245 eV. (c) O K_α partial fluorescence yield. (d) O K_α inverse partial fluorescence yield plotted along with the total fluorescence yield.

Table 4.1: Extracted doping values x in $Eu_{1-x}Gd_xO$. Comparison between nominal x and values extracted from x-ray adsorption spectroscopy (TEY, IPFY) and PGAA.

Nom. x	TEY	IPFY	PGAA
0.02	0.026	0.027	—
0.05	—	—	0.042
0.08	0.11	0.095	0.082
0.16	0.21	0.18	0.16

EuO and Eu_2O_3 in the literature [128], we use our XAS measurements to determine the oxidation state of Eu in EuO. While our surface sensitive TEY measurements show a small component of Eu^{3+} combined with a prominent Eu^{2+} signal, our bulk sensitive IPFY measurement shows nearly entirely Eu^{2+}. This behavior is consistent with the surface of EuO oxidizing, either from pinhole leaks in the protective capping layer, or while electrodes were deposited on the film. Despite the later process occurring in vacuum, the EuO surface can still oxidize due to residual gas, as was already shown in §4.3.

4.4.5 X-Ray Photoelectron Spectroscopy

Similar to XAS, x-ray photoelectron spectroscopy, or XPS, is used to characterize oxidation states in the doped EuO films. XPS involves the photoexcitation of a core electron with binding energy which is sensitive to the chemical environment of the crystal [27]. Typically the binding energy and often the lineshape of the resulting spectra are indicative of the atomic oxidation state from the element involved in the excitation. As an example, in Figure 4.10 we show the photoemission intensity of the Lu 4*d* core level multiplets for $Eu_{0.96}La_{0.04}O$, Lu metal, and Lu_2O_3. Lutetium metal was deposited at room temperature MBE and measured immediately, and Lu_2O_3 was formed by keeping the lutetium metal in vacuum with a background pressure of 2×10^9 Torr for at least 1 hr prior to measurement. Comparing the peak positions to those reported in the literature [129] confirms that Lu in EuO is in the 3+ oxidation state. A similar analysis was performed on Gd-doped EuO, shown already in Figure 4.4 and for La-doped EuO (not shown).

4.4.6 Low-energy electron diffraction

Low-energy electron diffraction (LEED) is used to characterize the surface crystal structure of EuO films following ARPES measurements. An exemplary LEED image is shown in Figure

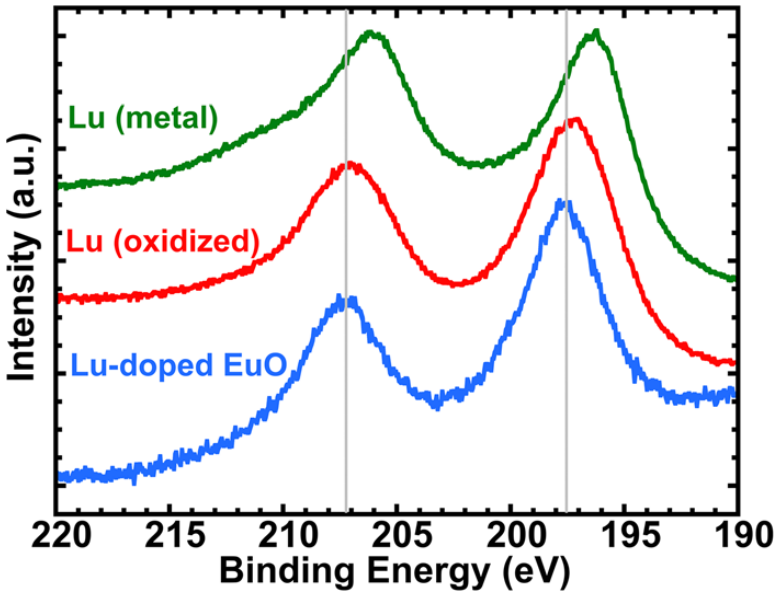

Figure 4.10: Comparison of XPS intensity of the Lu 4*d* core-level for $Eu_{0.96}Lu_{0}.04O$ (blue), Lu metal (green), and oxidized lutetium (red). The vertical grey lines are included as guides to the eye. Reproduced with permission from Ref. [11].

9.4, taken on a $Eu_{0.95}Gd_{0.05}O$ film. The image shows clear diffraction spots, indicating a well ordered surface, and no evidence of superstructure or surface reconstructions. Further information of about LEED characterization and using LEED I-V to determine surface crystal structure is included in Appendix A.

4.5 Conclusions

In this Chapter, we have described the growth of EuO thin films by MBE, starting with a generic description of the film deposition process and then focusing the on the special adsorption-controlled growth regime utilized for EuO, which produces high quality films free of oxygen vacancies. We have additionally discussed the extreme sensitivity of EuO to oxidation, highlighting one of the greatest challenges to studying this material. We have finaally discussed a number of experimental techniques used to characterize the quality of these films, ranging from structural probes such as RHEED, LEED, and XRD to electronic

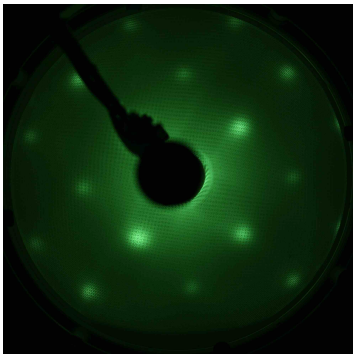

Figure 4.11: Low-energy electron diffraction (LEED) image of an $Eu_{0.95}Gd_{0.05}O$ film grown on $YAlO_3$. The electron beam energy is 100 eV. Reproduced with permission from Ref. [124]

probes, such as charge transport, XAS, and XPS. After establishing the high structural quality and macroscopic electronic properties of our films, we will proceed to relate these to the underlying electronic structure which we measure using ARPES, as will be described in subsequent Chapters.

CHAPTER 5

Electronic Structure of Europium Oxide[1]

There is an intriguing dichotomy between the real space and electronic structure of EuO. As a binary oxide which crystallizes in the rock salt structure, notably without complexities typically present in correlated oxides such as octahedral rotations and superstructure, EuO is a comparatively simple material structurally. Yet a complete description of its electronic structure presents formidable challenges, as it includes strong correlations via localized Eu $4f$ valence electrons and temperature-dependent magnetic effects.

Some insight can be gained into the electronic structure from an electron counting perspective. The electronic structure of free Eu and O atoms is

$$[\mathrm{Eu}] = [\mathrm{Xe}]4f^7 6s^2 \qquad [\mathrm{O}] = [\mathrm{He}]2s^2 2p^4 \tag{5.1}$$

but when incorporated into the highly ionic EuO crystal, the elements adopt oxidation states of ±2 which results in an electronic structure consisting of

$$[\mathrm{Eu}^{2+}] = [\mathrm{Xe}]4f^7 \qquad [\mathrm{O}^{2-}] = [\mathrm{He}]2s^2 2p^6 = [\mathrm{Ne}]. \tag{5.2}$$

While the $2p$ shell of the O^{2-} ion is completely filled, the outermost $4f$ shell of Eu^{2+} is only half filled. This may lead one to erroneously conclude that EuO is a metal, as is illustrated

[1] Much of the data presented in this Chapter has been published in D.E. Shai *et al.* Phys. Rev. Lett. **108**, 267003 (2012) and is reproduced here with permission.

schematically in Figure 5.1(a). However, strong on-site correlations of the $4f$ orbitals cause a large energy splitting between the spin-up and down components, giving rise to a ferromagnetic ground state. The large splitting of the Eu $4f$-derived orbitals also results in an energy gap between Eu $4f$ and Eu $5dt_{2g}$ which classifies EuO as a charge transfer insulator, illustrated in Figure 5.1(b).

In this Chapter, we will use photoemission spectroscopy to directly measure the electronic structure of $Eu_{1-x}Gd_xO$. We will map out the Fermi surface in the low temperature metallic state, and compare it to first principles calculations which predicts a half-metal. We also reveal the existence of a feature just below E_F at the Brillouin zone center, which likely corresponds to an electrically inactive bound state. Upon warming into the paramagnetic state, we will reveal a strong momentum-dependent evolution of the electronic structure, where the low temperature metallic states at are replaced by pseudogapped states which coexist at the Brillouin zone center with the bound states identified below T_c.

5.1 Experimental Details

35 nm thick $Eu_{1-x}Gd_xO$ films were grown[2] in both Veeco 930 and Veeco GEN10 oxide molecular-beam epitaxy (MBE) chambers on (110) terminated $YAlO_3$ substrates in adsorption-controlled conditions at a temperature of 350 °C [86, 90], where stoichiometric EuO can be produced without detectable concentrations of oxygen vacancies. The Eu flux was 1.1×10^{14} atoms/cm^{2}s, and the Gd flux was varied to achieve different doping levels (x). Immediately following growth, the films were transferred to the ARPES chamber in less than 300 seconds under ultra-high vacuum (2×10^{-10} torr). ARPES measurements were performed using a VG Scienta R4000 spectrometer, with an instrumental energy resolution $\Delta E = 25$ meV, He Iα photons ($h\nu = 21.2$ eV) and a base pressure typically better than 6×10^{-11} torr. Film quality

[2]Films were grown by A. Melville.

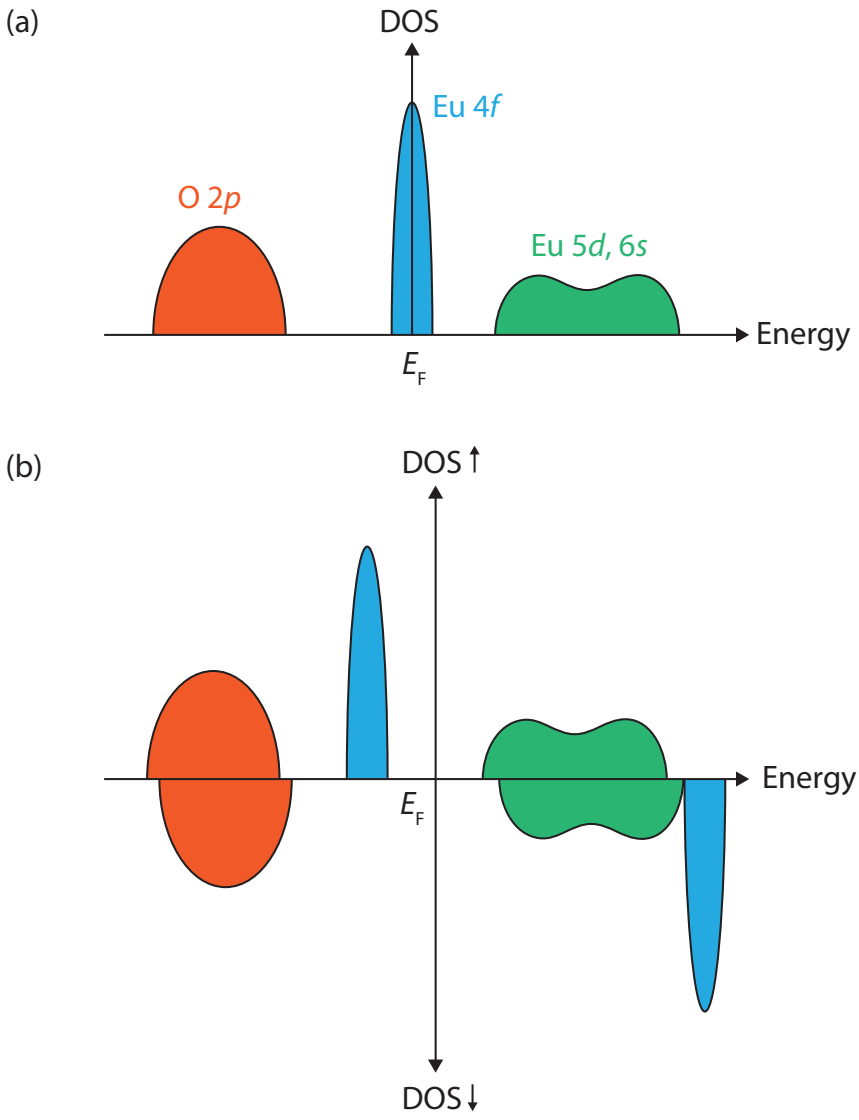

Figure 5.1: (a) Schematic density of states for EuO neglecting electron correlations, predicting metallic conductivity. (b) EuO density of states accounting for on-site Coulomb repulsions of the Eu 4f states. The large energy splitting ($U \sim 8$ eV) results in 7 fully spin polarized f electrons.

was monitored during growth using reflection high-energy electron diffraction (RHEED) and after ARPES measurements using low-energy electron diffraction (LEED), which shows a 1×1 surface structure. Results were confirmed by repeating measurements on over 35 individual samples and temperature-dependent measurements were confirmed by cycling samples from 140 K to 10 K and back to 140 K without noticeable degradation. Fermi surface (FS) maps were verified on multiple samples to check against the possibility of degradation. Additional *ex situ* characterization was performed on films capped with amorphous Si using x-ray absorption spectroscopy at the SGM beamline at the Canadian Light Source to determine the true Gd concentration and x-ray diffraction to verify the film structure and phase purity (as described in Chapter 4).

5.2 General Electronic Structure

In Figure 5.2(a), we show the valence band for $Eu_{0.94}Gd_{0.06}O$ with a nominal T_c of 123 K, which consists of O $2p$ states between 4-6 eV and Eu $4f$ states around 1-3 eV binding energies, consistent with measurements on single crystals [130] and undoped EuO films [85]. In Figure 5.2(b), we show the near E_F spectra for x = 0.007, 0.013, and 0.06 doped samples at 10 K, exhibiting a monotonic increase in spectral weight with Gd (electron) doping. Films with $x < 0.007$ were highly insulating, did not exhibit near E_F spectral weight, and charged up electrostatically upon exposure to the photon beam; we could not observe evidence of metallic surface states predicted for undoped EuO [131]. Shown in Figure 5.2(c) is the temperature dependence of the $4f$ peak in $Eu_{0.95}Gd_{0.05}O$ around $(k_x, k_y) = (0, 0)$, which shifts to lower binding energies as the sample is cooled below T_c (also reported by Miyazaki *et al.* [85]), while its lineshape remains largely unchanged. The temperature-dependent shift of the peak maximum is in close agreement with the optical redshift for a bulk sample of similar

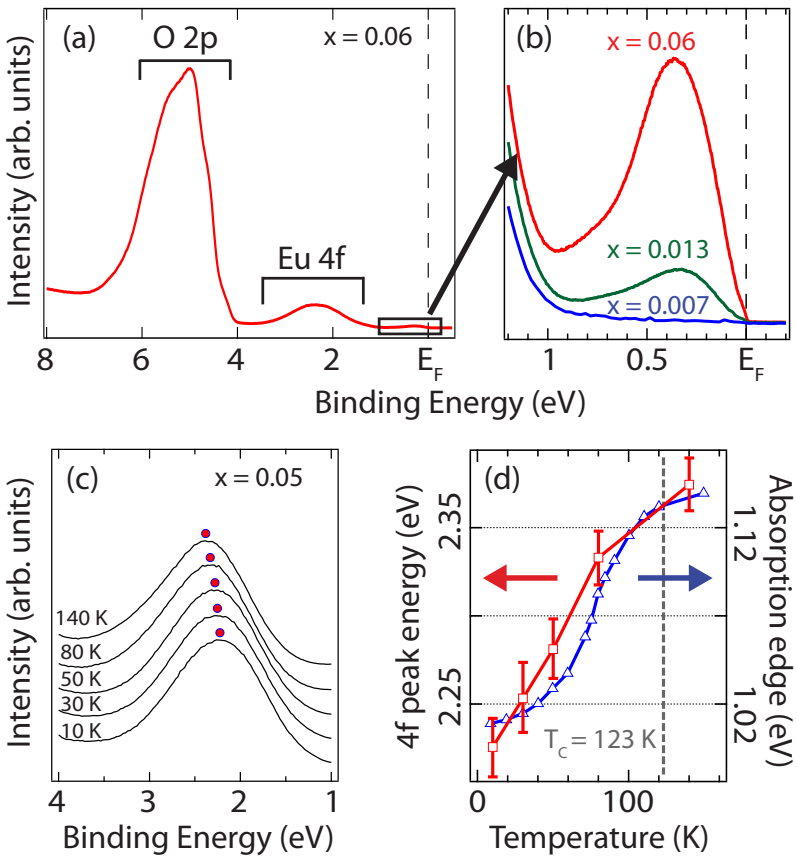

Figure 5.2: (a) Valence band of $Eu_{0.94}Gd_{0.06}O$ at 10 K, integrated within a $k = 0 \pm 0.3$ Å^{-1} window along the line $k_x = k_y$, showing the Eu $4f$ states along with the O 2p states at higher binding energies. (b) Near E_F states for $Eu_{1-x}Gd_xO$ films at 10 K with $x = 0.007$, 0.013 and 0.06, integrated within a window of ± 0.5 Å^{-1}. (c) Temperature dependence of the Eu $4f$ band in $Eu_{0.95}Gd_{0.05}O$, showing a shift to lower binding energies with decreasing temperature. (d) Comparison of the $4f$ shift with the bulk redshift measured optically [132].

carrier concentration [132] shown in Figure 5.2(d), indicating that our ARPES measurements are consistent with bulk properties measured using optical absorption.

5.3 Ferromagnetic Metallic State

In order to address the nature of the spin-polarized metallic carriers in the FM state, we focus on the near E_F states at 10 K and will discuss the data above T_c later in the text. A Fermi surface (FS) map is shown in Figure 5.3(a). The map clearly exhibits small elliptical pockets

centered around the X point ($(0, 2\pi/a)$ in the 2D BZ) at the zone boundary. A perpendicular cut through this pocket in Figure 5.3(b) reveals an electron-like band with a sharp Fermi cutoff at E_F, indicating metallic states. Additionally, we also observe a low energy feature located near the Γ point ($(0, 0)$ in the 2D BZ), shown in Figure 5.3(b). We attribute these to more deeply bound states (DBS) which are likely defect-derived and centered at a binding energy of 0.45 eV and exhibit only very weak dispersion and no appreciable spectral weight at E_F, and therefore are not visible in the FS map.

In Figure 5.4, we compare our low temperature ARPES results to electronic structure calculations for $Eu_{1-x}Gd_xO$. The calculations were performed using density functional theory (DFT) with the generalized gradient approximation plus on-site Coulomb interactions (GGA+U), based on the parameters determined by Ingle and Elfimov [105]. In Figure 5.4(a), we plot the band structure along high symmetry lines, showing the minimum of the spin-polarized conduction band at the X point. To treat the effect of carrier doping in the simplest manner possible, we perform a rigid shift of the chemical potential into the conduction band. Figure 5.4(b) shows the calculated 3D FS consisting spin-polarized electron pockets centered around X. In Figure 5.4(c), we present a simulated ARPES FS intensity map for $x = 0.025$ (we will return to discuss our choice of the doping level later in the text). To generate Figure 5.4(c), we average the calculated Fermi surface along k_z, weighted with a Lorentzian of width $1/\lambda$, where $\lambda = 8$ Å is the photoelectron mean free path. The location in k_z was determined based on the synchrotron-based photoemission measurements in Ref. [85], wherein it was reported that at $(k_x, k_y) = (0, 0)$, states near $k_z = 6\pi/c$ (the X point in the extended fcc Brillouin zone) are probed with 38 eV photons, and states at $k_z = 8\pi/c$ (the Γ point in the extended fcc Brillouin zone) are probed with 78 eV photons. In the context of the nearly free electron model [41], the location probed in k_z is determine by the inner potential V_0 through Equation (2.6). Combining Equation (2.6) and the photoemission measurements discussed above, the inner potential for EuO is $V_0 - \phi = 13.2$ eV.

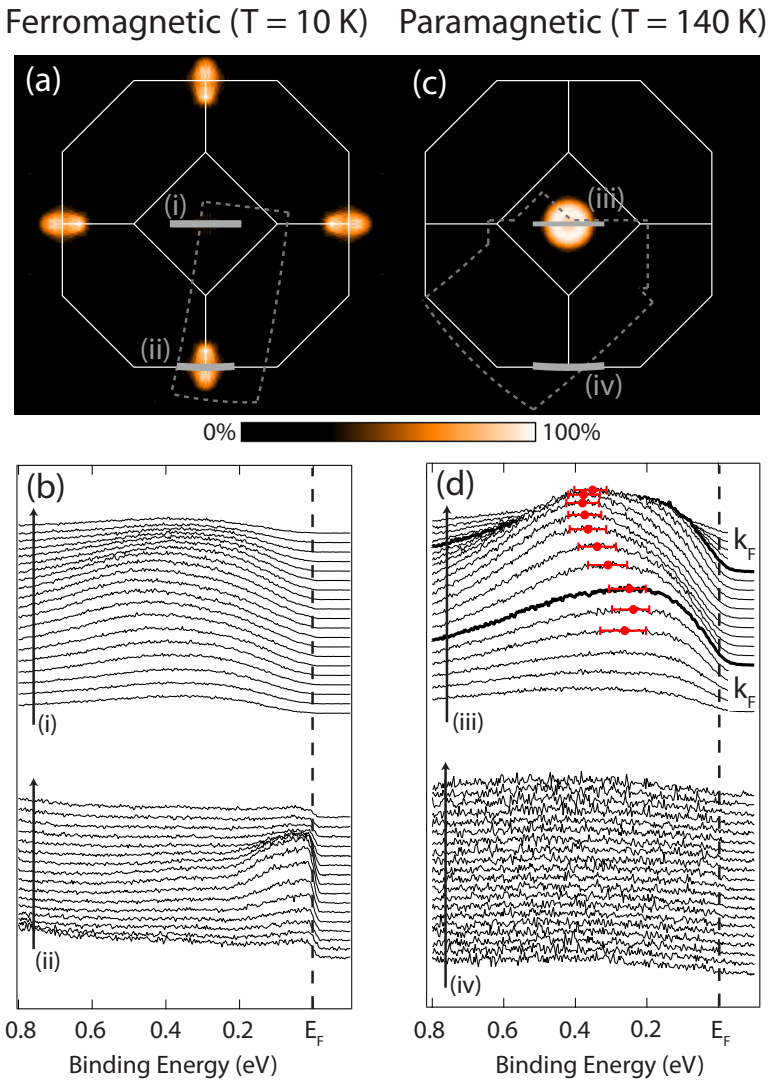

Figure 5.3: Temperature-dependent near-E_F spectra for $Eu_{0.95}Gd_{0.05}O$. (a) Fermi surface map taken in the FM state at T = 10 K, with an integration window of $E_F \pm$ 30 meV. The raw data were collected in the region within the dashed lines and symmetrized according to the 2D-projected BZ. (b) Energy distribution curves (EDCs) taken at T = 10 K along cuts through the BZ boundary $(0, 2\pi/a)$ and BZ center (0, 0). The reciprocal space location of the cuts are indicated in (a). (c) Fermi surface map taken above the Curie temperature at T = 140 K. (d) EDCs at the BZ center and boundary taken at 140 K. The points for cut (iii) show the dispersion of the EDC peak and k_F is determined by fitting the peaks in the momentum distribution curves at E_F. EDCs in (i) and (iii) are normalized to the $4f$ band peak intensity, and EDCs in (ii) and (iv) are normalized so the background at 1 eV matches (i) and (iii).

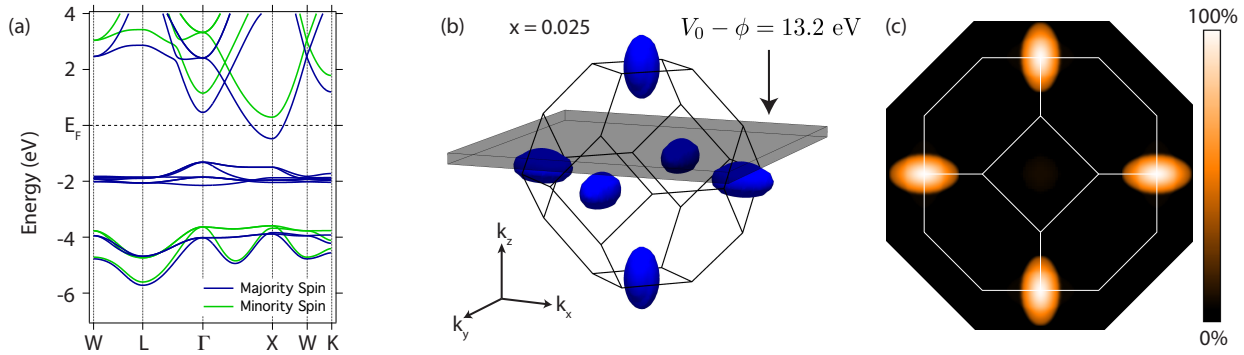

Figure 5.4: (a) Bandstructure for EuO along high symmetry directions in the fcc Brillouin zone. (b) Calculated spin-polarized Fermi surface for EuO, assuming a rigid shift of the Fermi level. The grey box of width $1/\lambda$, where $\lambda = 8$ Å represents the integration window to account for the final state broadening (Equation (2.6)). (c) Calculated ARPES Fermi surface, generated by averaging the data shown in (b) in the out-of-plane (k_z) direction (see text for details).

The predicted ARPES FS is composed of spin-polarized, elliptical electron pockets centered at $(0, 2\pi/a)$ of primarily Eu 5*d* character. Although this is a simplified approach, the calculated FSes nevertheless appear to capture qualitatively the FS features experimentally observed in Figure 5.3(a). The qualitative agreement between the simulation and experiment demonstrates that DFT based approaches [105, 133] can accurately treat the mobile carriers in the FM metallic state. This finding supports the numerous theoretical studies of EuO, including the possible effects of epitaxial strain on T_c [105], realizing a new multiferroic from strained EuO [83], and predictions for spin-polarized 2D electron gases at the interfaces of EuO-based superlattices [111]. This agreement can also be taken as supporting evidence that the FM metal-insulator transition arises from an indirect exchange interaction between the Eu 5*d* conduction band and the FM ordered Eu 4*f* moments which lowers the bottom of the majority spin conduction band below E_F.

The more localized DBS states near (0, 0) are beyond the scope of our simple rigid band approximation. The DBS states exhibits some momentum dependence, indicating that these states comprise a defect band which is not completely localized in real space. Nevertheless, due to their vanishing spectral weight at E_F, shown by the momentum

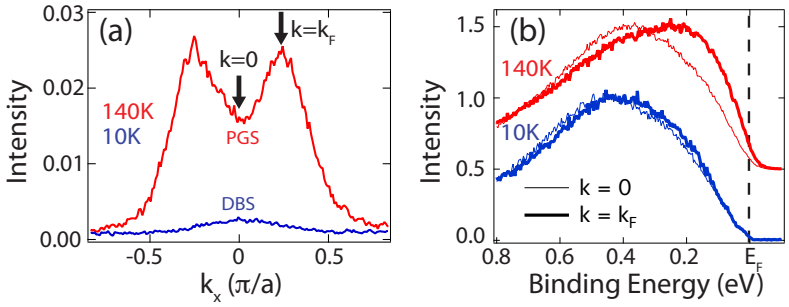

Figure 5.5: (a) Momentum distribution curves (MDCs) measured along $k_y = 0$ at 140 and at 10 K for $Eu_{0.95}Gd_{0.05}O$. MDCs have been integrated within a ± 10 meV window about E_F, and data has been normalized to the peak Eu $4f$ intensity. (b) Energy distribution curves taken at $k = 0$ and $k = k_F$ (indicated in (a)) above and below T_c. Spectra in (b) have been normalized to their peak intensity between 0.2-0.5 eV binding energy.

distribution curve (MDC) in Figure 5.5(a), the DBS likely play a negligible role in the low temperature conductivity, which is dominated by the metallic states at $(0, 2\pi/a)$.

5.4 Paragmagnetic Insulating State

Upon warming into the PM insulating state (140 K), the FS map changes dramatically (Figure 5.3(c)). Around $(0, 2\pi/a)$, the metallic states are lifted above E_F (shown in Figure 5.3(d)) due to the vanishing FM exchange splitting. Spectral weight is transferred to the BZ center, contributing to the ring of intensity around (0, 0), also shown in Fig 5.3(d). The contrast between the behavior of carriers at (0, 0) versus at $(0, 2\pi/a)$ underscores the importance of employing a momentum-resolved probe in studying the properties of carrier doped EuO.

Our comparison of the lineshape at the BZ center below and above T_c shown in Fig 5.5(b) shows that the DBS (10 K) consist of broad and only weakly dispersive spectral weight. In contrast, while the spectra above T_c also exhibit the broad signature of the DBS at higher binding energy, they show an additional more highly dispersive component of spectral weight which sits closer to E_F, indicating that another population of carriers has formed between the DBS and E_F, which we call the pseudogapped states (PGS). The small but finite

spectral weight of the PGS near E_F is likely responsible for the transport properties observed in the PM phase for films in this doping regime, which exhibit "bad metal" conduction at high temperatures, followed by a slight exponential upturn in the resistivity above T_c, indicating the formation of a small (<10 meV) activation gap [134, 135]. Such a gap is much smaller than our combined instrumental (ΔE = 25 meV) and thermal broadening at 140 K and therefore cannot be detected in our measurements. This activated behavior in $Eu_{1-x}Gd_xO$ is notably different from the variable range hopping conduction observed in the similar ferromagnetic metal-insulator compound $Ga_{1-x}Mn_xAs$ [136].

5.5 Discussion

Despite the increased intensity near E_F, the PGS are still broad in energy and strongly suppressed in intensity within 200 meV of E_F, forming a pseudogap reminiscent of features seen in the high-T_c cuprates [137], Fe_3O_4 [138], and the manganites [139, 140], all of which exhibit insulating behavior resulting from strong electron correlations. For the case of $Eu_{1-x}Gd_xO$, such pseudogapped behavior could arise from incoherent carrier hopping, as will be discussed further in Chapter 7. The spectral weight transfer that we observe through the metallic transition is related to the transferring of electrons from the PGS to spin-polarized electron pockets at the BZ boundary. This non-trivial behavior is unexpected and demonstrates that doped electrons in EuO do not simply enter non-dispersive donor impurity states.

Our observation of two populations of carriers above T_c is consistent with the recent Hall measurements by Mairoser *et al.* [91] which indicate that less than 50 % of the Gd dopants are electrically active at 10 K. The PGS electrons which are closer to E_F are electrically active above T_c and are transferred to the EuO conduction band below T_c. On the other hand, the electrons comprising the DBS well below E_F appear to remain inactive at all temperatures.

The percentage of dopants that enter PGS and in DBS can be estimated by comparing the photoemission intensity about the BZ center at T = 10 K and 140 K (Figures 5.3(b)(i) and 5.3(d)(iii)). The data was integrated in energy over the near-E_F states to produce momentum distribution curves of the dopant-induced states below E_F. These curves represent the photoemission intensity along a 1-dimensional line through the 3-dimensional Brillouin zone. Assuming a spherical geometry and that $k_z = 0$, the total photoemission intensity I at a given temperature T can be represented as an integral of the momentum distribution curve at that temperature, $MDC_T(k)$:

$$\begin{aligned} I(T) &= \iiint MDC_T(k)\, k^2 \sin(\theta) dk d\theta d\phi \\ &\approx 2\pi \int_{-\pi/a}^{\pi/a} MDC_T(k)\, k^2 dk. \end{aligned} \tag{5.3}$$

By comparing the spherically-integrated number of states at 140 K and 10 K, the number of dopants entering electrically active states can be computed as

$$\text{Active dopants} = \frac{I(140) - I(10)}{I(140)}. \tag{5.4}$$

Using the data shown in Figure 5.3(b) and 5.3(d), we find that 50 ± 10% of the dopants enter PGS, while the remaining carriers enter the inactive DBS.

This incomplete carrier activation is why we have presented calculations for $x = 0.025$ rather than the experimentally determined doping of $x = 0.05$ in Figure 5.4. Future work is needed to determine the origin of the segregation of carriers into active and inactive populations, but one possibility is that the DBS represent the formation of a defect band resulting from Gd dopant clustering or Gd-induced oxygen vacancies. We hope that our experimental observations will inspire more detailed experimental and theoretical studies of these bound states.

The behavior we have described in $Eu_{1-x}Gd_xO$ exhibits striking similarities to the colossal magnetoresistive manganites. In both $Eu_{1-x}Gd_xO$ and the manganites, sharp metallic features at E_F are clearly observed by ARPES in the FM metallic state, but upon warming into the PM insulating state, only broad, dispersive, pseudogapped features remain [139]. One profound difference between these systems is that in the manganites the pseudogapped bands in the PM state track the **k**-space locations of the erstwhile FS in the FM state [139, 140], while in $Eu_{1-x}Gd_xO$, the FM metallic and PM pseudogapped states exist in completely different regions of momentum space. This is somewhat unexpected, as dopants in n-type semiconductors would be expected to form below the conduction band minimum [141]. This momentum-space dichotomy between the states at $(0, 0)$ and those at $(0, 2\pi/a)$ suggests that the DBS and PGS have extremely weak hybridization with the low-temperature metallic states and may explain the dramatic metal-insulator transition at low dopings.

5.6 Conclusions

Our findings are summarized in the schematic in Figure 5.6. Below T_c, metallic carriers are observed in the spin-polarized conduction band at $(0, 2\pi/a)$ in addition to minimally dispersive deeply bound states at $(0, 0)$. Upon warming, the exchange splitting of the conduction band is reduced to zero and the metallic carriers and spectral weight at $(0, 2\pi/a)$ are transferred to $(0, 0)$, where they populate a second dopant-induced state just below E_F, the PGS. These high temperature carriers exhibit a pseudogapped but dispersive lineshape, naturally explaining the increase in resistivity through the metal-insulator transition. Our work reveals for the first time the nature of the FM metal-insulator transition in carrier doped EuO and uncovers an unusual momentum space dependence to the evolution of the electronic structure.

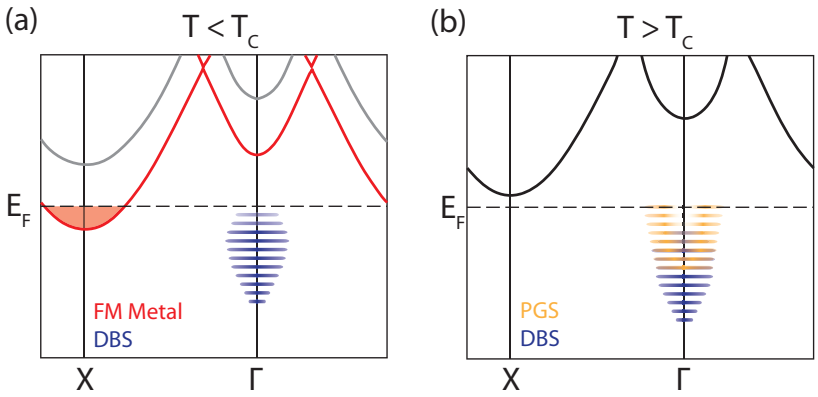

Figure 5.6: (a) Momentum space electronic structure in the ferromagnetic metallic phase and (b) in the paramagnetic semiconducting phase. In (a), metallic carriers are indicated at X, while the DBS are shown at Γ. In (b) the PGS form at Γ between the DBS and E_{F}.

CHAPTER 6

Doping Evolution of the Valence Band in EuO

In Chapter 5, the main characteristics of the EuO valence band were discussed, primarily for a single doping value (5%). The valence band was identified as exhibiting features related to O $2p$ and Eu $4f$ derived states and the temperature dependence of the valence band was found to track the optical redshift observed previously. In this Chapter, we will discuss how the valence band evolves as the Gd doping content is varied. In §6.2 we will revisit the concept of a temperature-dependent redshift and show that the magnitude of this shift decreases systematically with increasing charge carrier density. By examining the low temperature properties of the valence band as a function of doping, we will show in §6.3 that the band gap is modulated as more Gd is incorporated into the crystal. Through comparison with density functional theory calculations, we will show that this band gap reduction is related to compressive strain induced by the cation mismatch between the Gd dopant atom and the Eu cation. These results prove that chemical doping has a prominent effect on the electronic structure in EuO and suggest that strain can be used to significantly alter the properties of this material.

6.1 Experimental Details

Experimental details related to the growth and characterization of the films studied in this Chapter can be found in §5.1. Data presented in this Chapter were acquired using both He Iα (hν=21.2 eV) and He IIα (hν=40.8 eV) photons. Temperature cycling was always performed

from high to low temperature to avoid the possibility of surface degradation. In several cases, after cooling, sample temperatures were again cycled back to high temperature to confirm the reproducibility of the experimental results.

6.2 Redshift

As we discussed in §5.2, EuO undergoes an optical redshift with decreasing temperature, which has previously been interpreted as a shrinking band gap resulting from the ferromagnetic exchange splitting of the EuO conduction band. In §5.2 we showed that this redshift can be observed experimentally with photoemission, by tracking the peak position of the Eu $4f$ band as a function of temperature, and that the overall shift agrees well with what has been reported using optical measurements.

Here, we discuss how this redshift evolves as a function of cation doping. In Figure 6.1(a), we show large energy range valence band scans for $Eu_{1-x}Gd_xO$, $x = 0.013$ taken at $T = 140$ K and $T = 10$ K with 21.2 eV photons. As the sample is cooled, an energy shift is observed over the entire measurement energy range. The inset shows the behavior of the Eu $4f$ band which has a lineshape that remains relatively unchanged and is therefore ideally suited for a quantitative analysis of this redshift.

In Figure 6.1(b) we show the Eu $4f$ band at high and low temperature for $Eu_{1-x}Gd_xO$ with $x = 0.013$, 0.05, 0.11, and 0.21, illustrating the presence of a redshift for all measured doping values, although it is clear from this data that the overall magnitude of the energy shift diminishes as a function of increased doping level. In Fig 6.1(c) we quantify the magnitude of this shift as a function of Gd content. The abscissa is the free carrier density as measured by low temperature Hall effect [91] on a set of companion samples grown in parallel with those used in our photoemission measurements. When displayed as a function of carrier density rather than dopant concentration, the overall magnitude of the redshift is found to decrease

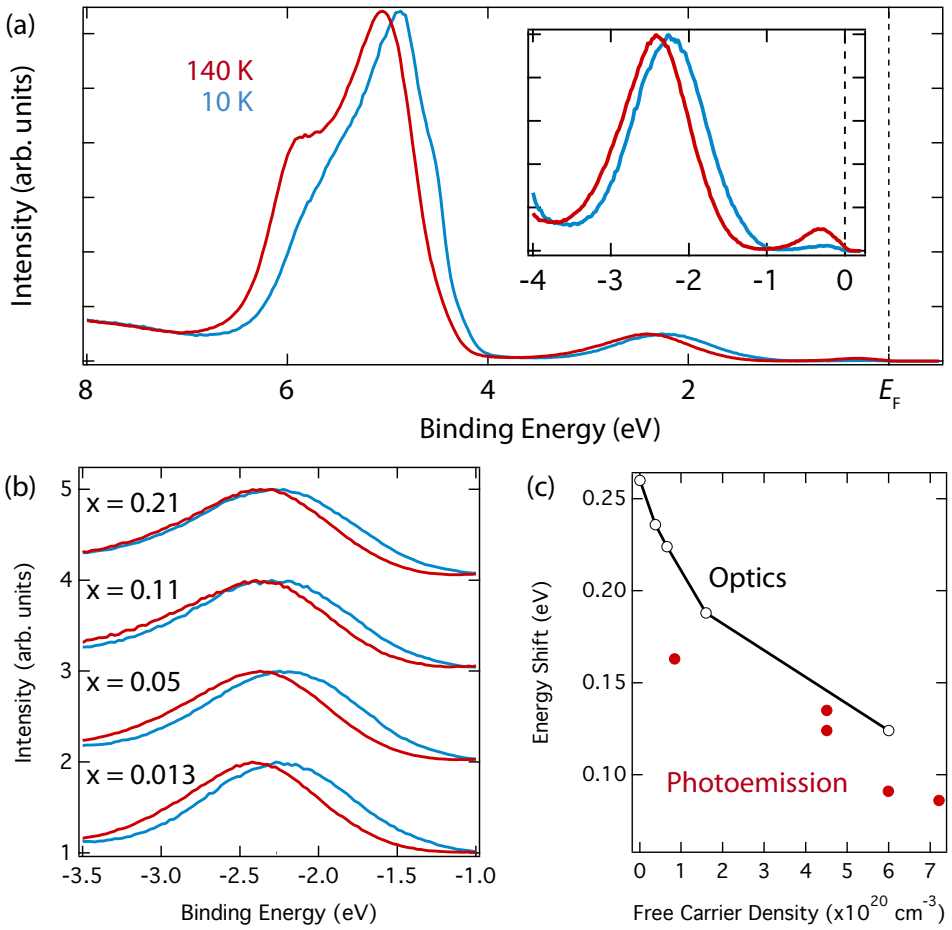

Figure 6.1: Doping dependence of the redshift in $Eu_{1-x}Gd_xO$. (a) Large energy range valence band scan for $x = 0.013$ taken both above and below T_C, showing the shift of the entire valence band with temperature. (inset) Close-up view of the Eu $4f$ valence band and the charge carriers near E_F. (b) Temperature dependent Eu $4f$ spectra for four different doping values. (c) Extracted total energy shift from the the data reported in (b), along with the redshift determined from previous optical measurements on bulk crystals [132].

linearly as a function of free carrier density by approximately 50% over the measured carrier density range. This systematic decrease is remarkably similar to what has been reported previously via optical absorption measurements, which have also been reproduced in Figure 6.1(c). This exceptional agreement with optical spectroscopy provides further evidence that our photoemission measurements are representative of the bulk electronic structure in EuO.

6.3 Band gap

Our measurements of the $Eu_{1-x}Gd_xO$ valence band additionally provide insight into the effect of doping on the host material band gap. While photoemission probes only the occupied electronic states, measurements on very lightly elecron-doped samples should provide an accurate depiction of the band gap since E_F should be pinned very close to the bottom of the conduction band. For these measurements we have chosen to acquire data using He IIα photons at normal emission, which places the probed value of k_z near the X point ($k_z = 2\pi/c$), and according to our DFT calculations (Fig 5.4) this should be representative of the direct (optical) band gap. The data is taken at low temperature ($T = 20$ K) to ensure that E_F is pinned at the bottom of the bulk conduction band, also at X.

In Figure 6.2(a) we show the valence band of $Eu_{1-x}Gd_xO$, $x = 0.013$ taken with He IIα photons. As compared with our He Iα data, there are clear differences in the structure of the valence band, due to the different k_z value probed, as well as the overall intensity of the O $2p$ and Eu $4f$ bands, which results from the photon energy dependence of the photoionization cross-section [142]. In Figure 6.2(b) we show the same data, this time focusing on the valence band structure at the top (low binding energy side) of the Eu $4f$ states. We find the photoemission intensity decreases nearly linearly in this region, and by fitting a straight line to this data, we find it intersects the abscissa at an energy of ~ 1.1 eV, a value which

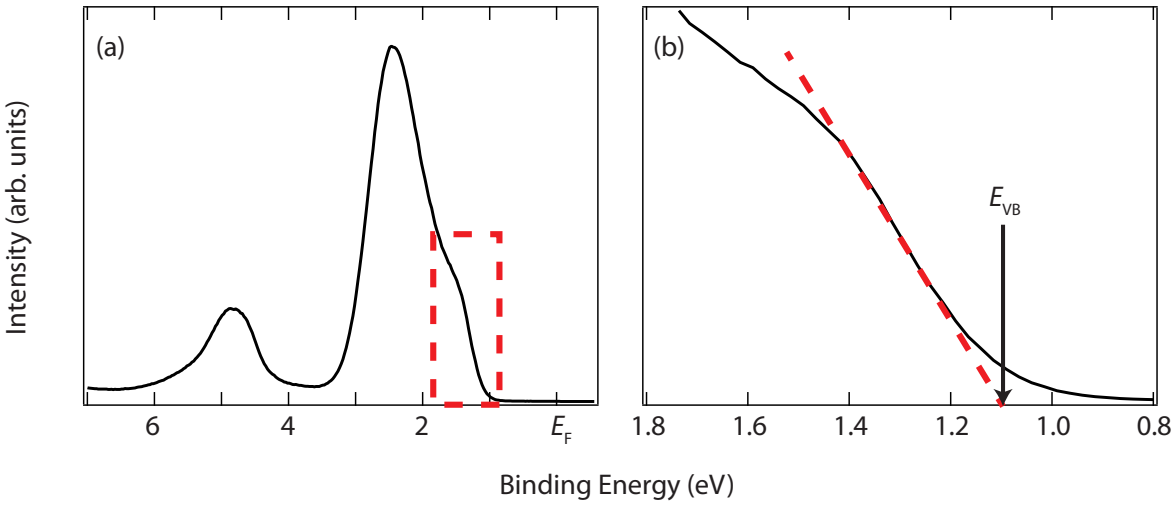

Figure 6.2: (a) Valence band of $Eu_{1-x}Gd_xO$, $x = 0.013$ taken with He IIα photons. (b) Close-up showing the determination of the valence band maximum, E_{VB}.

we denote as E_{VB}. This value is in remarkably close agreement with the measured low temperature optical gap of 0.9 eV [132].

Having established the validity of our photoemission measurements in determining the band gap of EuO, we now focus on the effect of doping on the gap. In Figure 6.3(a-b) we show the EuO valence band for various Gd concentration. By examining the spectra near the valence band maximum, it is clear that there is a systematic evolution of the valence band toward the Fermi level with increasing Gd content. This is in clear contradiction to what one would expect from a rigid band shift, where the addition of charge carriers would push the Fermi level away from the valence band maximum and therefore result in a increase of E_{VB} with x. This result indicates a reduction of the Eu $4f - 5d$ band gap with doping.

We quantify this doping-dependent shift of the valence band in Figure 6.3(c), where we plot the extracted relative shift in E_{VB} as a function of nominal Gd content x. We find that E_{VB} decreases monotonically with x (and not with carrier density n), suggesting that this modulation of the band gap is structural in origin and stems from the presence of a Gd atom. Similarly, the intensity peak position of the Eu $4f$ band shifts toward E_F by approximately

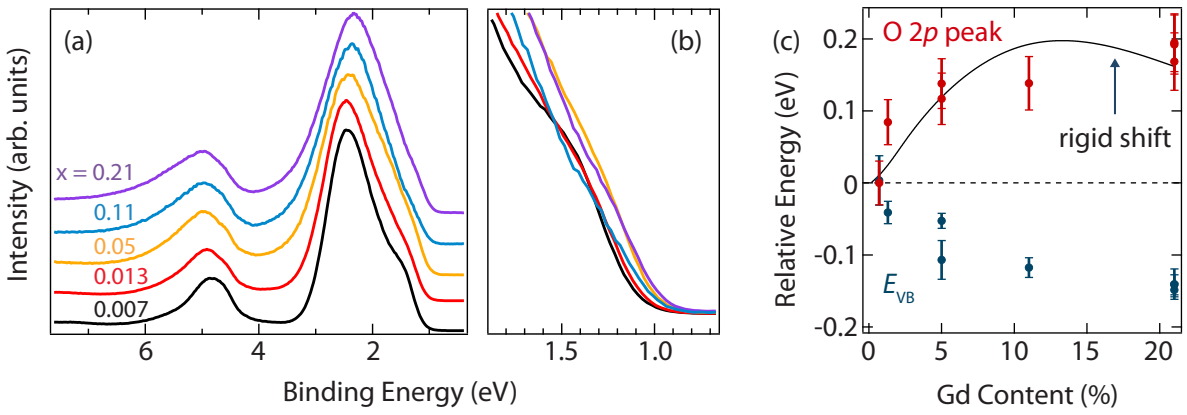

Figure 6.3: (a) Large energy range valence band scans of $Eu_{1-x}Gd_xO$ taken with He IIα photons for various doping levels x. The curves are offset for clarity. (b) Same as (a) but zoomed in near the valence band maximum to illustrate the doping-dependent trend in E_{VB}. (c) Relative energy shift of the valence band maximum (E_{VB}) along with the O 2p band with increasing Gd content. Also included is the expected energy shift utilizing a rigid band shift density functional theory calculation (see text for details).

100 meV with increasing Gd content, although there is comparatively more scatter in the data using this metric. For comparison, we also include in Figure 6.3(c) the relative position of the O 2p band (determined by the point of maximum intensity of this band) as a function of Gd content. The O 2p band shifts to higher binding energy (away from E_F) with increasing Gd concentration. Additionally, we include the expected relative energy shift for a rigid band system. To calculate this, for a given Gd content, we have taken the corresponding experimentally-measured charge carrier density [91] and have used this to extract the carrier-density-dependent Fermi level shift using first principles density function theory calculations (§5.3). The rigid energy shift is non-monotonic with Gd content (x) because the charge carrier density (n) does not increase monotonically with x. The O 2p band appears to shift in close agreement with what one would expect from this simple rigid band shift, whereas the Eu 4f band shifts in the opposite direction.

Given that the Gd^{3+} ionic radius (1.078 Å) is ~ 18% smaller than the Eu^{2+} ionic radius (1.31 Å) [143], the possibility of a strain induced change in electronic structure must be considered. Such a cation mismatch would induce a local strain field in the EuO, which has

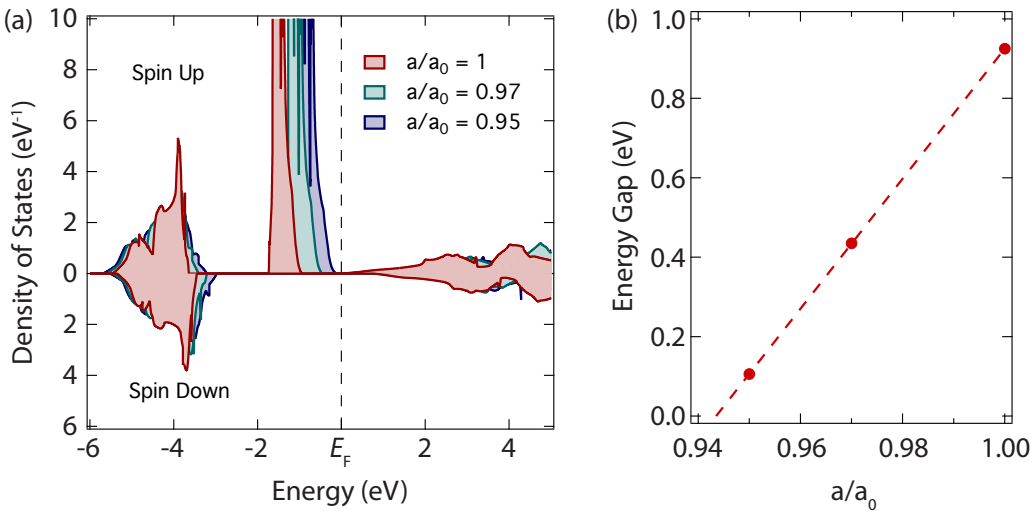

Figure 6.4: (a) Calculated strain dependent density of states for EuO. (b) Calculated Eu $4f - 5d$ energy gap as a function of reduced lattice constant a/a_0.

been shown to respond sensitively to strain with first principles calculations [105] and experimentally with magnetometry [109]. To explore the effect of strain on EuO, we have carried out first-principles calculations of the EuO density of states as a function of cubic lattice constant, a, varied relative to the equilibrium lattice constant, a_0. In Figure 6.4(a) we show the DFT calculated density of states for various amounts of compressive strain, $a/a_0 \leq 1$. Our results are based on and very similar to the calculations originally reported by Ingle and Elfimov [105]. In each case the Fermi level has been pinned at the bottom of the EuO conduction band. Careful examination of Figure 6.4(a) shows that while the position of the O $2p$ states is relatively insensitive to strain, aside from an increase in bandwidth, the Eu $4f$ states respond very strongly. As the lattice constant is reduced, the $4f$ band is pushed toward the Fermi level until it ultimately reaches and overlaps the bulk conduction band at a value of $a/a_0 \approx 0.94$ (Figure 6.4(b), very close to the value reported in Ref [105]). While this calculation neglects the additional charge carriers added by the dopant atoms, it shows that the effect of dopant-induced strain is fully consistent with our experimental results, which show that the energy separation between the Eu $4f$ and O $2p$ increases as a function of x

The idea of a dopant atom causing a local strain has been suggested before for EuO. Recent x-ray adsorption spectroscopy measurements combined with first-principles calculations have reached similar conclusions by studying unoccupied states in Gd-doped EuO [144]. There, it was suggested that the dopant induced strain could account for the increased ferromagnetic T_c observed experimentally realtive to that calculated by first principles for an unstrained sample. Moreoever, recent structural measurements on both Gd [93] and Sc-doped films (with 32% mismatch in ionic radius) [145] have shown that the c-axis lattice constant systematically decreases with increasing dopant substitution. This effect is also seen in bulk, e.g, in the SrO-EuO solid solution [146].

6.4 Conclusions

In this Chapter, we have identified several effects that doping has on the large energy scale valence band electronic structure. We have shown using ARPES that the overall magnitude of the magnetic redshift decreases with increasing charge carrier density, consistent with previous optical measurements. Furthermore, the Eu $4f - 5d$ band gap has been shown to shrink proportionally to the Gd content x, suggesting that it is derived from a lattice effect, rather than a carrier density effect. Our first-principles calculations suggest that this effect could be a result of strain induced in the lattice due to the cation size mismatch between Eu and the dopant species.

These results indicate that cation substitution could provide an route to controllably manipulate the optoelectronic properties of EuO. For instance, EuO is well-known for its significant magneto-optical effects such as the extremely large Faraday rotation [147], and photo-induced metal-insulator transition. Dopant-induced valence band modifications would also be expected to effect the photoinduced ultrafast spin dynamics observed recently [148].

While our measurements here have explored the effect of strain induced by cation size mismatch, it is suggested that a further avenue for exploring these effects would be to use epitaxial strain. Strain offers a 'clean' control parameter to systematically investigate lattice effects without considering changes in carrier density. Potentially suitable substrates on which the epitaxial growth of EuO has already been established include (001) 9.5 mol % yttria-stabilized cubic zirconia (-0.05% strain) [149], (110) $LuAlO_3$ (+0.4 to +1.5% strain) [150], and (110) $YAlO_3$ (+1.4 to +2.2% strain) [151]. Furthermore, one could investigate carrier density effects without the application of strain by utilizing field-effect-like electrostatics, discussed in Chapter 8.

CHAPTER 7

Doping Evolution of the Near E_F states in EuO

As we have shown in Chapters 5-6, chemical doping has profound effects on the valence band and the near E_F electronic structure in EuO. Notably, we have identified several unusual charge-carrier-derived features near the center of the Brillouin Zone which are not expected from standard electronic structure calculations. These features consist of broad and relatively non-dispersive deeply bound states (DBS) at low temperatures, and a significantly more dispersive feature existing at high temperatures, which we denoted pseudogapped states (PGS). In this Chapter, we will explore how these features evolve as a function of doping and use this information to draw conclusions regarding their origin.

7.1 Experimental Details

Experimental details related to the growth and characterization of the films studied in this Chapter can be found in §5.1. Temperature cycling was always performed from high to low temperature to minimize the possibility of surface degradation.

7.2 Doping Evolution of the Deeply Bound States

In Figure 7.1, we present ARPES measurements for $Eu_{1-x}Gd_xO$ near E_F as a function of Gd content, x ranging from 0.013 to 0.21. The upper panels in (a)-(c) are taken at T = 10 K in the ferromagnetic metallic phase and represent the deeply bound states (DBS), introduced in

Chapter 5. Across the measured doping range, we observe an evolution from relatively non-dispersive broad spectral weight ($x = 0.013$) to features clearly exhibiting dispersive character, yet with intensity strongly suppressed near E_F. This trend can be understood qualitatively on the grounds that if the DBS truly represent localized or bound states there will be a doping threshold above which these states will overlap and begin to hybridize and form a band. This condition is dependent on whether any adjacent cation sites are occupied with similar DBS, which can be quantified in terms of the average nearest neighbor occupancy. Accounting for the twelve-fold coordination of the face centered cubic EuO lattice, we can compute the doping-dependent DBS nearest-neighbor occupancy, $n_{\mathrm{DBS}}(x)$ as

$$n_{\mathrm{DBS}}(x) = 12x\left(1 - \frac{n_{\mathrm{Hall}}}{n_{\mathrm{Eu}}}\right), \tag{7.1}$$

where x is the doping content, and $(1 - n_{\mathrm{Hall}}/n_{\mathrm{Eu}})$ represents the number of inactive dopants. For the doping values studied here, we find n_{DBS} to be approximately 0.16 ($x = 0.013$), 0.55 ($x = 0.05$), and 2.97 ($x = 0.21$). Thus at the highest doping values measured here, there are on average more than 2 nearest neighbors with an inactive Gd atom, implying substantial overlap, which could explain the dispersive characteristics observed in our photoemission measurements.

7.3 Doping Evolution of the Pseudogapped States

In addition to the DBS, in Chapter 5 we also revealed that the active charge carriers occupy an enigmatic pseudogapped state (PGS) at (0, 0) above T_C. Here, we image how these states evolve as a function of doping at a constant $T = 140$ K (Figure 7.1(a)-(c), lower panels). There is a clear progression from a weakly visible dispersive band for the sample with $x = 0.013$ to a prominently dispersive feature at $x = 0.21$.

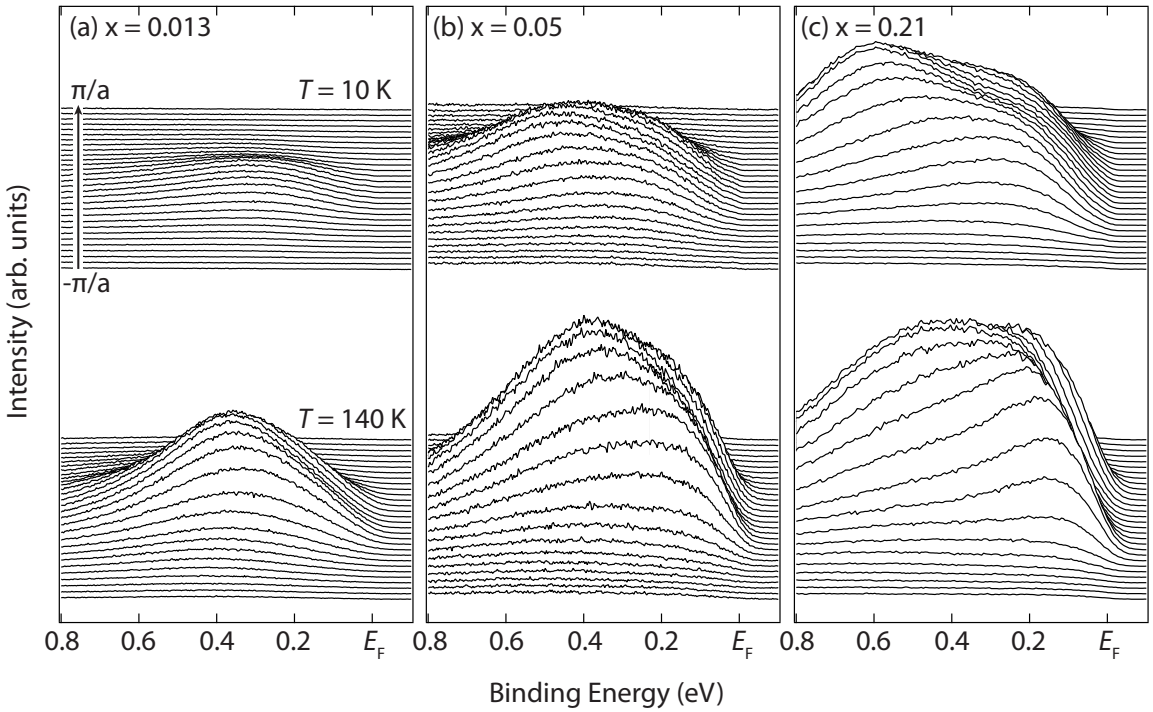

Figure 7.1: Doping-dependent evolution of near E_F states in $Eu_{1-x}Gd_xO$, for (a) $x = 0.013$, (b) 0.05, and (c) 0.21. Data at the top of each panel are taken at $T = 10$ K in the ferromagnetic metallic phase, and bottom are taken at $T = 140$ K in the paramagnetic phase.

Our doping dependent measurements of the PGS illustrate how the photoemission intensity evolves as a function of carrier concentration. From this data, we can extract a doping dependent Fermi wavevector, k_F, which we define as the distance between two peaks in the MDC at E_F, illustrated in Figure 7.2(a). In Figure 7.2(b) we show the extracted values of k_F as a function of Gd content. There is a clearly increasing trend with doping ranging from $k_F = 0$ (no states observable) at $x = 0.007$ to $k_F \approx 0.2$ Å^{-1} at $x = 0.21$. While our measurements of k_F give an indication of the Fermi surface volume and therefore the charge carrier density via Luttinger's theorem [152, 153], they cannot be used to directly calculate a carrier density since they probe at a non-zero value of k_z (Figure 5.4). If one assumes a spherical Fermi surface, then a truly accurate estimate can only be made by measuring k_F at $k_z = 0$. If, however, we assume the probed value of $k_z \approx 0$, then assuming spin-degenerate

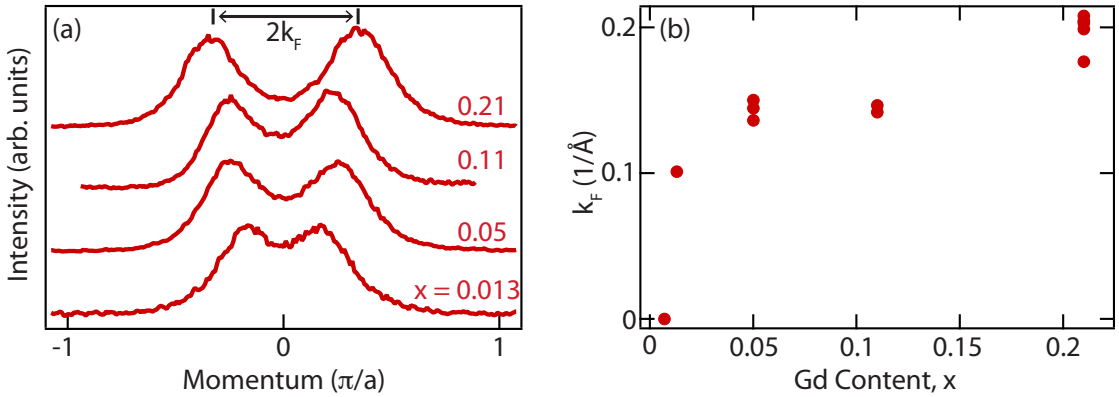

Figure 7.2: (a) MDCs (offset for clarity) taken at $E_F \pm 20$ meV as a function of doping, illustrating the increase in FS size with doping. The double-headed arrow defines the quantity k_F. (b) Extracted values of k_F as a function of nominal Gd content, x.

carriers we calculate for $x = 0.21$ a carrier density of $n_{\text{Luttinger}} \approx 2.7 \times 10^{20}$ cm^{-3}, which is within a factor of two value reported for Hall effect measurements performed at 4.2 K [91].

While the measurements presented in this section characterize how the PGS evolve with x, the exact nature of these states is still unclear. An important consideration while discussing the high temperature charge carriers comes from the doping dependent carrier density above T_c. If one considers the high-temperature charge carrier density relative to the carrier density at low temperatures in the ferromagnetic metallic phase (Figure 7.3), it is clear that there exists a critical doping value above which the high-temperature charge carrier density above T_c is nonzero. Thus, EuO undergoes a doping-dependent metal-insulator transition in addition to the temperature-dependent transition considered already. In the following section, we will discuss this transition along with the nature of the high temperature PGS in terms of the concept of 'semi-localized' charge carriers.

7.4 Semi-Localization

The concept of a doping-induced semiconductor to metal transition was originally developed by Mott [154]. It is frequently discussed in the context of traditional semiconductor systems

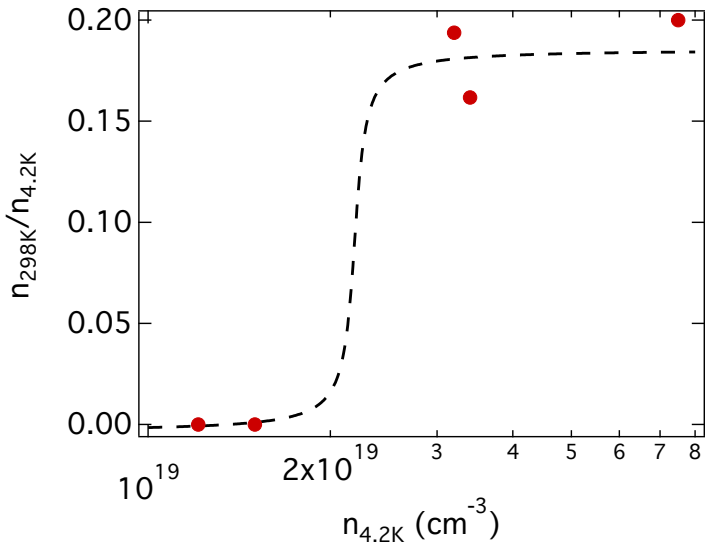

Figure 7.3: Ratio of the charge carrier density in the paramagnetic phase n_{298K} relative to the density in the ferromagnetic phase, $n_{4.2K}$ as a function of $n_{4.2K}$ for $Eu_{1-x}Gd_xO$. Data was taken from Ref. [14] and the dashed line is included as a guide to the eye.

such as Si:P and other group IV elements [155], and has been shown to hold for an even larger group of systems [156]. The general idea is that a donor charge carrier embedded in a semiconducting matrix will be localized near the donor nucleus within a radius a_B which is the crystal Bohr radius. It is not until a critical number of donors are added to the system and begin to overlap that a continuous conducting path is formed triggering an insulator-to-metal transition. Within Thomas-Fermi screening theory [157], this amounts to the condition that

$$a_B \cdot k_s \geq 1, \tag{7.2}$$

where

$$a_B = \frac{\kappa_0 \hbar^2}{m^* e^2} \tag{7.3}$$

is the crystal Bohr radius and

Table 7.1: Compilation of critical charge carrier densities, n_c for Gd- and oxygen vacancy-doped EuO reported in the literature.

Work By	Compound	n_c (cm^{-3})	Technique
Petrich *et al.* [12]	EuO_{1-x}	>2.4E19	Hall effect
Oliver *et al.* [158]	EuO_{1-x}	4E19	Optical absorption
Shapira *et al.* [14]	$Eu_{1-y}Gd_yO_{1-x}$	2E19	Hall effect
Mairoser *et al.* [91]	$Eu_{1-x}Gd_xO$	1E19	T_c vs x
Godart *et al.* [159]	$Eu_{1-x}Gd_xO$	8E19	Hall effect

$$k_s = \frac{6\pi e^2 n}{\kappa_0 E_F} \tag{7.4}$$

is the inverse screening length. In the above, κ_0 is the static dielectric constant, m^* is the electron's effective mass, and n is the charge carrier density. Through some straightforward manipulation, Equation (7.2) can be shown to be equivalent to the condition that a metallic phase is formed in a doped semiconductor when

$$a_B n_c^{1/3} \geq 0.25. \tag{7.5}$$

Equation (7.5) is known as the *Mott criterion* and provides a relation between a_B and the critical charge carrier density, above which a metallic phase is formed. In EuO, the critical charge carrier density n_c has been determined by a number of different techniques, which are tabulated in Table 7.1. The most relevant of these data are those from Ref. [91], as those samples were fabricated using the same experimental system as those used in this study.

Given a charge carrier density of $n_c \sim 1 \times 10^{19}$ cm^{-3} one would expect from Equation (7.5) a crystal Bohr radius in the vicinity of ~12 Å. An electron doped into such a state can sample multiple lattice sites and is therefore not truly localized, which would result in an impurity band dispersed uniformly throughout momentum space. Yet as it is bound to a donor atom

in the dilute doping limit, it does not represent a fully itinerant charge carrier either. Instead, these carriers are expected to occupy a regime in which neither the local nor itinerant picture adequately depicts their nature.

The concept of a so-called 'semi-localized' state has been explored theoretically recently, with the advent of computational methods used to unfold first-principles band structure supercell calculations [160, 161]. Herng *et al.* [162] performed supercell calculations on Cu doped ZnO_{1-x} samples and showed that while Cu impurities formed truly localized states with uniform impurity bands throughout the Brillouin zone, the effect of oxygen vacancies was to create an impurity band with intensity located only near the Γ point. This area of intensity was interpreted as a semi-localized oxygen vacancy with a real space dimension of $\sim 2.25a$, where a is the lattice constant. Similar conclusions were drawn by Berlijn *et al.* [163] while examining the $BaFe_2As_2$ system.

Semi-localized states have also been observed experimentally in the semiconductor $\beta-Ga_2O_3$ doped with Si. It was first shown using scanning tunneling microscopy measurements that individual Si donor atoms could be resolved on a spatial length scale extending $\Delta r \sim$ 9-16 Å [164]. Subsequent ARPES measurements [165] revealed a dispersionless spectral function enclosed in a Gaussian envelope, the width of which was $\Delta k \sim 1/\Delta r$, the inverse of this real space length scale.

If we assume semi-localized states are present in EuO, then our measurements provide insight into this phenomenon in an entirely different carrier density regime. Whereas the $\beta-Ga_2O_3$ measurements were performed on samples estimated to be doped exactly to their critical carrier densities (1×10^{19} cm^{-3}), all of our EuO measurements were taken on samples with densities $\geq 10 \cdot n_c$ [91], a regime which should lead to significant overlap between donor

states and the formation of dispersive features[1]. This observation could explain why our measurements reveal dispersive PGS states above T_c.

We will now show that a system containing semi-localized states in the doping regime where spatially extended donor electron clouds begin to overlap can produce results which are consistent with our ARPES data[2]. For simplicity we will consider a system on a discrete lattice. In a traditional tight-binding picture, a lattice creation operator for an impurity state is given by $d^\dagger_{is}$, which creates an impurity electron with spin s at site i. Instead, for a doped semiconductor like EuO, let us consider a state that is spatially extended on a real-space length scale r_0 such that its creation operator is given by

$$\psi^\dagger_{dis} = \sum_j e^{-\frac{(\mathbf{r}_i - \mathbf{r}_j)^2}{2r_0^2}} d^\dagger_{js}. \tag{7.6}$$

where $\psi^\dagger_{dis}$ creates an impurity state with spin s localized around site i with localization radius r_0. The Hamiltonian for the impurity states can then be expressed as

$$\mathcal{H}_{\text{imp}} = \sum_{ij} t_{ij} \psi^\dagger_{dis} \psi_{djs} + \epsilon_D \sum_i \psi^\dagger_{dis} \psi_{dis} \tag{7.7}$$

where ϵ_D is the impurity state energy. As the states are spatially extended, we also account for extended hopping using

$$t_{ij} = e^{-\frac{(\mathbf{r}_i - \mathbf{r}_j)^2}{2r_0^2}}. \tag{7.8}$$

An important consequence of the extended nature of these states comes from the

[1]We note that attempts to measure samples at lower doping above T_c were unsuccessful as the samples charged up electrostatically.

[2]This model was conceived by M.H. Fischer and is included here for completeness.

momentum-space representation of the creation operator, $\psi^\dagger_{d\mathbf{k}s}$, given by (switching to integral form for simplicity)

$$\psi^\dagger_{d\mathbf{k}s} = \sum_i \langle dis|d\mathbf{k}s\rangle\, \psi^\dagger_{dis} \tag{7.9}$$

$$= \sum_i \left(\int d\mathbf{k} \sum_j e^{-\frac{\left(\mathbf{r}_i - \mathbf{r}_j\right)^2}{2r_0^2}} e^{i\mathbf{k}\cdot\mathbf{r}_i} \right) \psi^\dagger_{dis} \tag{7.10}$$

$$= e^{-\frac{\mathbf{k}^2 r_0^2}{2}} \sum_i e^{i\mathbf{k}\cdot\mathbf{r}_i} \psi^\dagger_{dis}. \tag{7.11}$$

From Equation (7.11) it is clear that the momentum-space representation of the impurity state is modulated by a gaussian with maximum intensity centered around $\mathbf{k} = 0$.

To help visualize this behavior, we have simulated the spectral function for a ferromagnetic semiconductor like EuO. Our model consists of a 1D lattice of spins coupled ferromagnetically to a conduction band (the so-called $s - f$ Hamiltonian) which then hybridizes with the doped, spatially extended impurity states. The full Hamiltonian is given by

$$\mathcal{H} = \mathcal{H}_\mathrm{c} + \mathcal{H}_\mathrm{f} + \mathcal{H}_\mathrm{cf} + \mathcal{H}_\mathrm{imp} + \mathcal{H}_\mathrm{hyb} \tag{7.12}$$

where $\mathcal{H}_\mathrm{c}$ describes the EuO conduction electrons, $\mathcal{H}_\mathrm{f}$ describes the f electrons, $\mathcal{H}_\mathrm{cf}$ accounts for the ferromagnetic interaction between the two, $\mathcal{H}_\mathrm{imp}$ describes the spatially extended impurity states (Equation (7.7)), and $\mathcal{H}_\mathrm{hyb}$ describes the hybridization between impurity states and the conduction band. The full details of the calculation will be described elsewhere [166]. We show the calculated spectral function for only the extended impurity states in the paramagnetic regime at three different doping values in Figure 7.4(a)-(c), which clearly illustrates the formation of a dispersive impurity band, along with the intensity suppression away from $\mathbf{k} = 0$. In Figure 7.4(d)-(f), we show the integrated MDCs for each doping value.

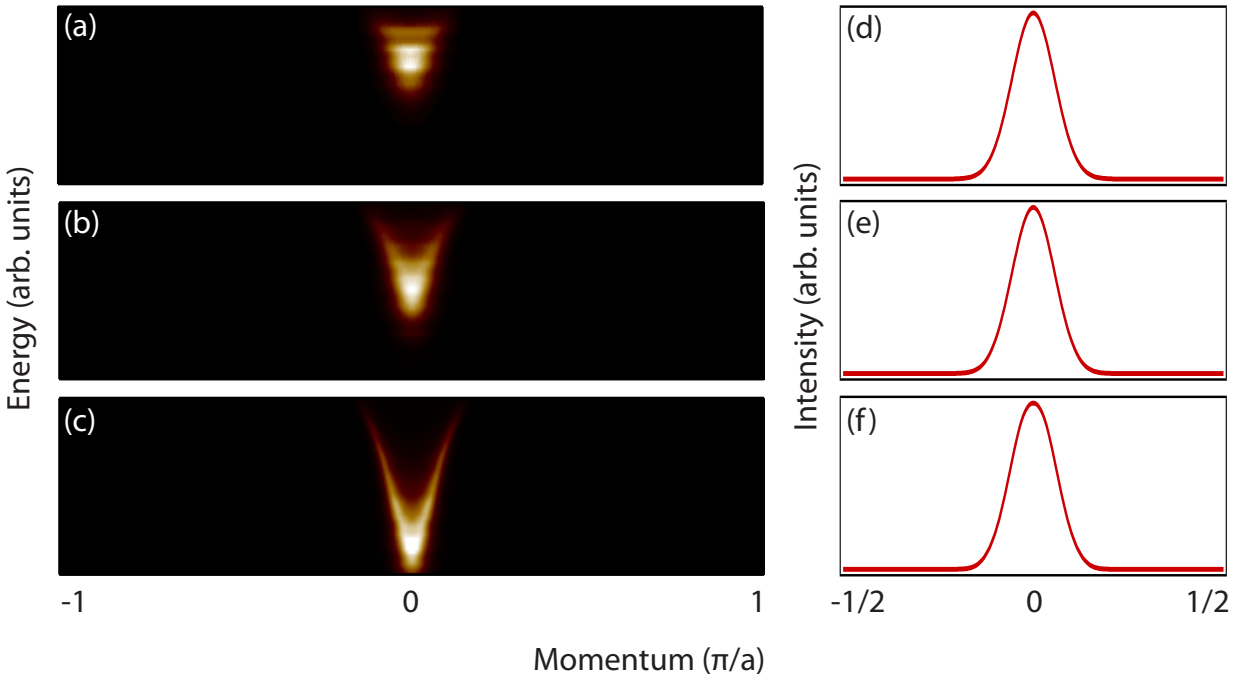

Figure 7.4: Simulated spectral function for a system consisting of spatially extended impurity states at doping values of (a) 1/8, (b) 1/4, and (c) 1/2, embedded within a ferromagnetic semiconductor above T_c. (d)-(f) Integrated MDCs for doping values of 1/8, 1/4, and 1/2, respectively. All MDCs are gaussian and have the same width.

In each case, the MDC is a gaussian function with width parameterized by r_0 (Equation (7.11)).

To compare this model to our experimental data, we have examined MDCs for $Eu_{1-x}Gd_xO$ over multiple doping values. Using the photoemission data shown in Figure 7.1, we generate MDCs by integrating over the entire near E_F spectral weight, from −1 to +0.1 eV. These MDCs are presented in Figure 7.5 (a)-(c). To extract the MDC representative of the PGS, we subtract the 10 K MDC from its 140 K counterpart, also shown in Figure 7.1.

In Figure 7.6, we plot the PGS MDCs on the same axes, each normalized to their maximum intensity. While there are small intensity variations at high k, it is noteworthy that the FWHM of each curve is nearly identical (0.39 $Å^{-1}$), despite having k_Fs differing by as much as a factor of two. This result is strongly suggestive that there is a k-dependent

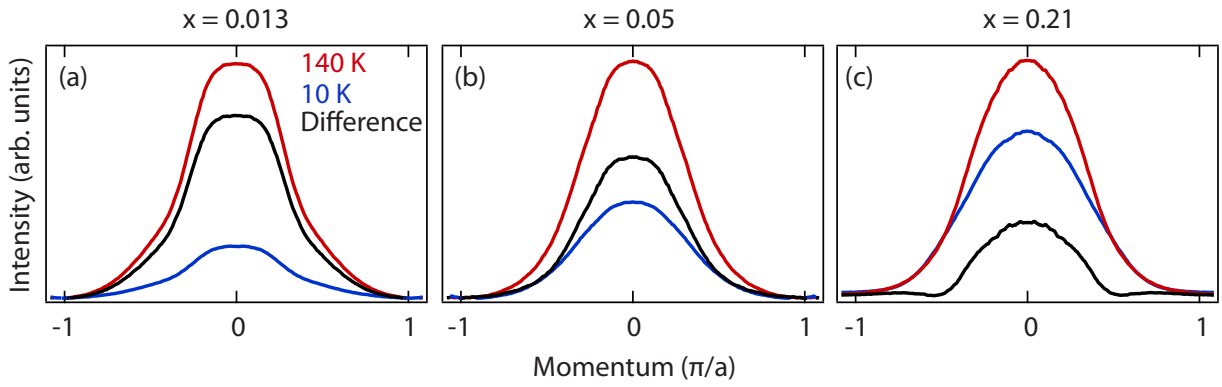

Figure 7.5: Momentum distribution curves for doped EuO. Curves are integrated from -1 eV to +0.1 eV, at 140 K (red) and 10 K (blue) for (a) $x = 0.013$, (b) 0.05, and (c) 0.21. The difference between the high and low temperature curves is plotted in black. In all cases, spectra are normalized in intensity relative to the peak intensity of the Eu $4f$ band.

suppression in the spectral function, as predicted by the argument described above (Equation 7.11). The uniform momentum-space width described above would correspond to a value of $r_0 = 4.26$ Å and correspondingly a real space FWHM of $\Delta r = 10.0$ Å. This result is remarkably close to the value for a_B predicted above using Equation (7.5). We note that by applying the same analysis to the DBS MDCs in Figure 7.5, we do not find a momentum-independent width. Rather, the MDC FWHM varies from 0.38 Å^{-1} ($x = 0.013$) to 0.48 Å^{-1} ($x = 0.21$). This x dependence indicates that our semi-localized state description does not accurately encompass the physics of the DBS.

Taken together, the presence of the PGS with maximal intensity at (0, 0) along with the doping-independent MDC width is suggestive that such a semi-localized state could accurately describe the charge carriers in doped paramagnetic EuO above T_c. A definitive experimental corroboration to this hypothesis could be achieved by atomically resolved scanning tunneling microscopy. Such as measurement has been carried out recently on an EuO_{1-x} thin films by Klinkhammer *et al.* [167], who showed that under tunneling conditions which sample the electronic rather than structural environment, an oxygen vacancy was found to have a real space extent with FWHM ~ 7.5 Å. Considering that STM measures the

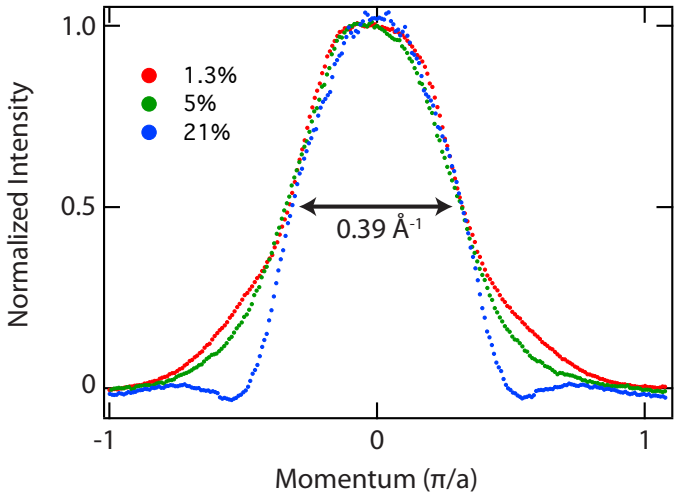

Figure 7.6: Difference MDCs (140 - 10 K) from Figure 7.5 plotted on the same intensity scale, illustrating identical widths irrespective of doping value/k_F.

square modulus of a real space wave function, $|\psi(x)|^2$, this would imply a wave function parameterized by $\Delta r \approx 10.6$ Å, again in excellent agreement with our k-space measurements.

While our measurements strongly suggest the presence of a semi-localized state, they do not elucidate the mechanism of localization. The primary source in conventional semiconductors is the dielectric background of the semiconducting host. This length scale is computed using Equation (7.3). The static dielectric constant of undoped EuO at room temperature is $\kappa_0 = 23.9$ [74]. The effective mass of EuO has been previously estimated by numerous groups with results ranging from $m^* = 0.35 - 1.1\ m_e$ [132, 168, 169]. From our ARPES measurements of the $x = 0.21$ sample where the dispersion of the PGS is most clear, we directly extract $m^* = 0.6\ m_e$, although this measurement is obfuscated somewhat due to the presence of the DBS. Using our experimentally measured value of m^* in conjunction with Equation (7.3), we calculate $a_B \approx 21$ Å, roughly twice as large as our previous estimates. This discrepancy could arise from a change in the dielectric constant of EuO with doping, or it is possible that there is another source of localization. Much attention has been devoted to the idea of magnetically induced localization (i.e., a magnetic polaron) forming at high temperatures [170, 171], where the electron is localized owing to its coupling to a

disordered magnetic background, although the accuracy of this picture has been questioned recently by Monteiro *et al.* who performed muon spin rotation measurements which suggest the complete absence of a magnetized state above T_c [95]. We have additionally performed measurements of the Eu $4f$ band position above T_c which do not reveal any abrupt changes in the magnetic redshift at high temperatures, consistent with previous optical data [132], and suggesting that if any short ranged magnetic order is present above T_c, it is not substantially affected by temperature.

7.5 Conclusions

In this Chapter, we have examined the doping evolution of the near E_F states in $Eu_{1-x}Gd_xO$. By examining the inactive DBS at low temperatures, we have identified a transition from non-dispersive impurity states to a more complex structure exhibiting signs of dispersion at the point where inactive sites begin to overlap and hopping is permitted. Furthermore we have imaged how the PGS evolve above T_c. Our measurements suggest that the unique structure of the PGS are a result of semi-localization of the active charge carriers due to the semi-conducting nature of the EuO lattice. By using a momentum space probe and comparing with a simple model calculation, we reveal that these carriers are localized on a real space length scale of ~10 Å, in agreement with multiple independent probes such as doping dependence of the charge carrier density and STM measurements. In this Chapter, we have also highlighted several other systems for which a semi-localized description of charge carriers seems appropriate (β-Ga_2O_3, ZnO, and $BaFe_2As_2$). We expect that these results are generalizable to describe an even larger class of systems described by doped impurities in a semiconductors. Our results show that by using a k-space probe such as ARPES, we are able to determine not only the band structure of the host system, but also to ascertain details about the real-space structure of these dopant species. This information

would be useful in making quantitative predictions about the effects of doping on the macroscopic charge transport properties of semiconductor systems.

CHAPTER 8

Formation of a two-dimensional free electron gas on the EuO surface using Cs deposition

As we discussed in Chapter 5, increasing the charge carrier density in EuO could lead to an increase the its ferromagnetic Curie temperature, and as a byproduct increase its utility as a component in spintronics based devices. While one common method to increase charge carrier density is the use of chemical chemical doping as described in Chapter 5, a more commonly used technique to modulating charge carrier density is to introduce or remove carriers electrostatically through the application of a gate voltage through a device such as a field effect transistor. While an EuO-based field effect transistor would be an enormously useful tool, both in terms of studying fundamental properties of EuO as well as for functional utility, generation of such a device has proven difficult in part as a result of its instability in air (see §4.3). Moreover, and the ability to electrostatically modulate charge carrier density through the application of a gate voltage is typically performed *ex situ*, preventing the simultaneous acquisition of photoemission spectra which provides valuable insight into the charge carrier dynamics as a function of carrier density.

A commonly used alternate approach to field effect devices is to utilize surface deposition of largely electropositive or electronegative atoms or molecules to modify the charge carrier density in a sample by means of bonding between the substrate and adatom(s). The most common materials used to accomplish this are the alkali metals, such as sodium, potassium, rubidium, and cesium. Historically, alkali metal deposition has been limited to the field of surface science, where modulation of a sample's surface electronic properties such

as the work function have important technological implications in the manufacture of photocathodes (e.g., Cs+O on GaAs [172]) as well as in surface catalysis [173].

The first description of the electronic process involved in alkali metal deposition on a sample surface was given by Langmuir [174], who postulated that at low coverages, the interaction between the alkali adsorbate and the sample surface would result in charge transfer provided the alkali metal ionization potential was smaller than the sample work function. In this picture, the single alkali metal *s* valence electron is transferred to the substrate, forming a surface dipole between the positively charged alkali nucleus and its image charge within the substrate. As the surface coverage is increased, depolarizing fields from adjacent dipoles will reduce the amount of charge transfer between the overlayer and substrate, resulting in a more metallic overlayer film residing on, but only weakly interacting with the underlying substrate. This picture was subsequently modified by Gurney [175] after it was discovered that Ba, Ca, and Sr deposited on W behaved similarly, despite the ionization potential of these materials all being smaller than the W work function. Gurney pointed out that as the alkali approaches and interacts with the substrate, its valence energy level will be modified and lifetime broadened, which can result in only partial charge transfer, even in materials where the substate work function is smaller than the alkali ionization potential. Together, this Langmuir-Gurney model was considered a paradigm for the explanation adsorbate-metal interactions [176] since its inception eighty years ago, although its accuracy has been called into question recently, as will be discussed later in this Chapter.

While photoemission has routinely been used as a characterization tool to study the effects of alkali deposition on substrates, it was only recently that the photoemission community began to use alkali deposition as a tool to aid in photoemission measurements of other materials. A result of the charge transfer between adsorbate and substrate is that the charge carrier density of the substrate is modulated. In the dilute coverage limit, one can measure spectra of the underlying substrate as a function of charge carrier density — often

reversibly — simply by varying the amount of adsorbate present on the sample surface. This approach has been shown to be successful in a number of systems including $YBa_2Cu_3O_{7-\delta}$ (YBCO) [177], Bi_2Se_3 [178], Na_2IrO_3 [179], 1*T*-TaS_2 [180], Au/Si(111) [181], MoS_2 [182], $MoSe_2$ [183], and graphene [184].

In this Chapter, we will explore how Cs deposition on the surface of EuO affects its electronic structure. We will present a systematic study of the evolution of both the valence band and Fermi surface as a function of Cs content in the high ($\sim$ 1 ML) coverage regime. We will additionally discuss the implications on the surface crystal structure of the adsorbed layer. Finally we will suggest several future experiments to further explore the unique characteristics of this system.

8.1 Experimental Details

Thin films of $Eu_{1-x}La_xO$ with $x \sim 0.04$ were grown[1] on (110) $YAlO_3$ substrates, as described in Chapter 4. Cs was evaporated from a commercial SAES alkali metal dispenser at a constant current of 5.0 amps, which was outgassed at 5.5 amps for 40 minutes prior to the measurements. During the measurements, Cs was deposited on the EuO film at both 140 K and 20 K, with qualitatively similar results. All photoemission data was taken with He Iα photons. Due to the unique geometry of the experimental chamber and the absence of a quartz crystal microbalance, the actual Cs flux on the sample is unknown, though it can be estimated as follows. The evaporation rate from a commercial Cs source run at 5.0 amps has been measured to be $\sim$ 40 μg/min [185]. At a distance R from the source, a substrate with area A subtends a solid angle of A/R^2. In our chamber, $R \approx 8$ inches, indicating a flux on the sample of $\Phi_{Cs} = 5.8 \times 10^{11}$ atoms/cm^2·s. The deposition rate of metallic cesium (density

[1] Films were grown by A. Melville.

$\rho_{Cs} = 8.8 \times 10^{21}$ atoms/cm^3) at this flux would be $\Phi_{Cs}/\rho_{Cs} \approx 0.04$ nm/min assuming a sticking coefficient of unity.

8.2 General Electronic Structure

We begin our discussion of the Cs/EuO system by analyzing the large energy scale valence band features. In Figure 8.1(a) we present valence band spectra over a wide energy range for EuO dosed with Cs for varying intervals. In all cases the Eu $4f$ and O $2p-$derived features (*c.f.* Figure 5.2) are present between 1-6 eV binding energy. With increasing Cs deposition, a prominent manifold of peaks appear in the 9-14 eV binding energy region. By comparing with previous photoemission measurements on Cs-based systems, we attribute these features to a Cs $5p_{3/2}$ level at 12.1 eV binding energy, along with an Auger transition ($O_{III}VV$) [186] at an apparent binding energy of 10 eV [187]. While the Cs $5p_{1/2}$ is also present around 14 eV binding energy, it is less resolved as a result of increased lifetime broadening due to Coster-Kronig transitions [187] and is masked by the large increase in secondary electron intensity. We also note that the O $2p$-derived band significantly broadens with Cs deposition, which would be consistent with increased scattering rates as a result of the Cs overlayer.

A low binding energy shoulder to the Cs $5p_{3/2}$ is apparent in the inset of Figure 8.1(a). Prior work has shown that this could be indicative of cesium oxide formation [186], although this is questionable here due to the extremely low base pressure in the measurement chamber (which is low enough to preserve EuO). A second possible explanation is that this shoulder results from a surface core level shift, as was suggested previously [187].

In Figure 8.1(b) we integrate the area of the Cs-derived valence band peaks relative to the Eu $4f$ peak (illustrated in Figure 8.1(a, inset)) and plot it as a function of Cs deposition time. The intensity of the Cs-derived peak can be expressed as

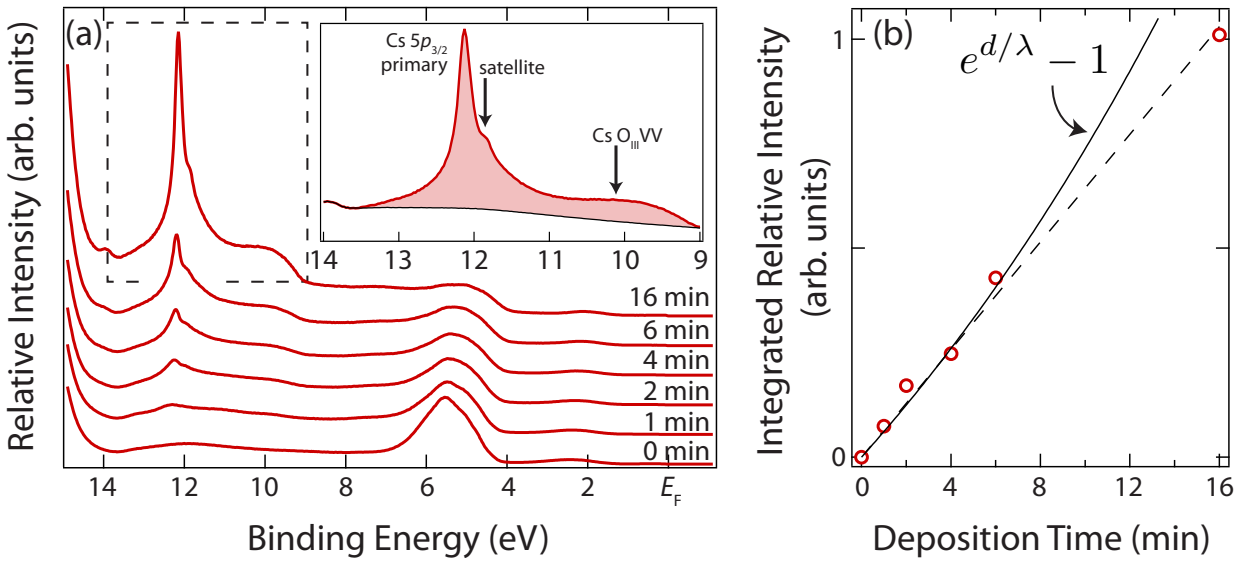

Figure 8.1: (a) Valence band spectra of EuO dosed with various amounts of Cs. Spectra have been normalized to the peak intensity of the Eu $4f$ peak near 2 eV and are vertically offset for clarity. (inset) Zoomed region for the 16 minute deposition illustrating the structure and integration of the Cs-derived peaks. (b) Integrated intensity of the Cs $3p_{3/2}$ core level and Auger $O_{III}VV$ peak between 9-14 eV binding energy as a function of Cs deposition time. The black dashed line serves as a guide to the eye, while the black solid line represents the predicted behavior from Equation (8.3), where we have chosen λ=1 nm and d to be the product of the estimated growth rate (0.04 nm/min) and the deposition time.

$$I^d_{\mathrm{Cs}} \propto \left(1 - e^{-d/\lambda}\right) \tag{8.1}$$

where d is the film thickness, and λ is the inelastic mean free path for a photoelectron propagating through the film. In contrast, the intensity from the EuO with a Cs overlayer of thickness d, I^d_{EuO}, is represented by

$$\mathrm{I}^d_{\mathrm{EuO}} \propto e^{-d/\lambda} \tag{8.2}$$

where the exponential function accounts for the attenuation of the photoelectrons by the presence of the adlayer. The ratio of the Cs $5p_{3/2}$ intensity to the Eu $4f$ intensity is therefore given by

$$\frac{\mathrm{I}^d_{\mathrm{Cs}}}{\mathrm{I}^d_{\mathrm{EuO}}} \propto \left(e^{d/\lambda} - 1\right) \tag{8.3}$$

$$\approx \left(d/\lambda + O(d^2/\lambda^2)\right). \tag{8.4}$$

Thus for film thicknesses $d/\lambda \ll 1$, the intensity ratio of Cs $5p$ to Eu $4f$ should increase linearly with Cs thickness. From our flux estimate in §8.1, even after 16 minutes of deposition, the expected film thickness would be ~0.64 nm, less than typical values for λ (see Figure 2.2). As is seen in Figure 8.1(b), the experimentally-measured ratio agrees well with Equation (8.3), although some deviation occurs for the most heavily doped sample. This could indicate either that d is slightly smaller than that based on our flux estimate, or that λ is larger than 1 nm. Nevertheless, our measurements clearly indicate the presence of a Cs overlayer in a thickness regime where d is large enough to produce both a bulk and surface component to the $5p_{3/2}$ core level yet still yield a linearly increasing intensity with deposition time.

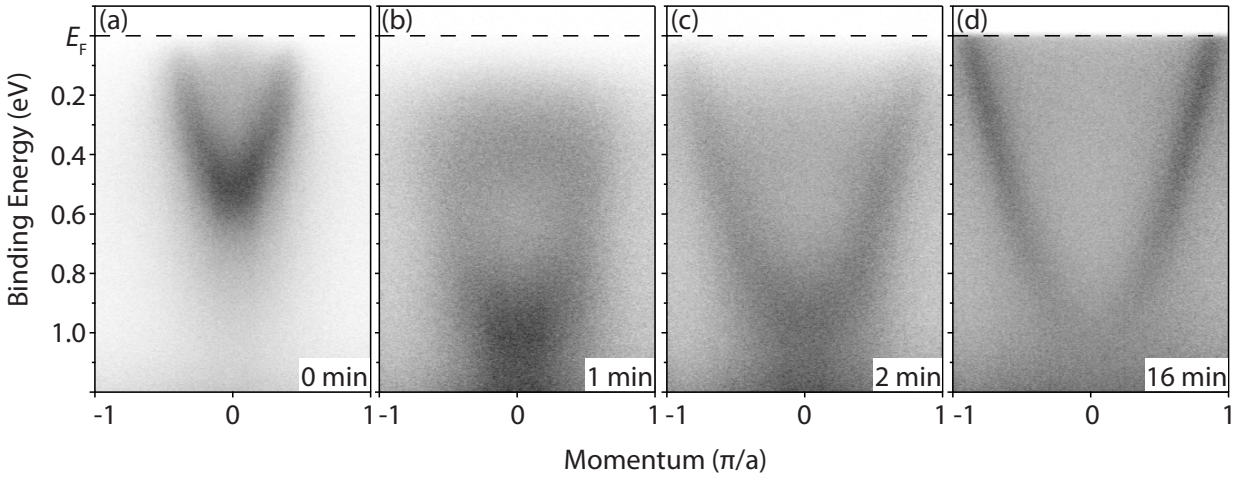

Figure 8.2: Evolution of the near E_F states in EuO as a function of cesiation time. All data taken at $T = 20$ K.

8.3 Fermi Surface

Having established the presence of Cs on the surface of the EuO films, we now turn our attention to the effect of Cs deposition on the electronic structure near the Fermi level. In Figure 8.2, we show the evolution of the near E_F states as a function of Cs deposition time. Figure 8.2(a) shows a pristine $Eu_{0.96}La_{0.04}O$ film showing a particularly clear image of the DBS described in Chapter 5. Following 1 minute of Cs deposition, these states become significantly blurred and the appearance of a new feature bottoming out around 1 eV is apparent (Figure 8.2(b)). After 2 minutes of Cs deposition, the original DBS feature is nearly indistinguishable from the background and has been replaced by an electron-like band, shown in Figure 8.2(c). Following the initial 2 minutes of Cs deposition, this electron-like feature no longer changes at a qualitative level, as is evidenced by the similarity to data taken after 16 minutes of deposition shown in Figure 8.2(d).

The abrupt appearance of a large electron pocket (LEP) at $(k_x, k_y) = (0, 0)$, particularly one which saturates in size, rather than a continuous evolution of the DBS is unexpected. More surprisingly, however, is the absence of the original electron pockets from EuO conduction

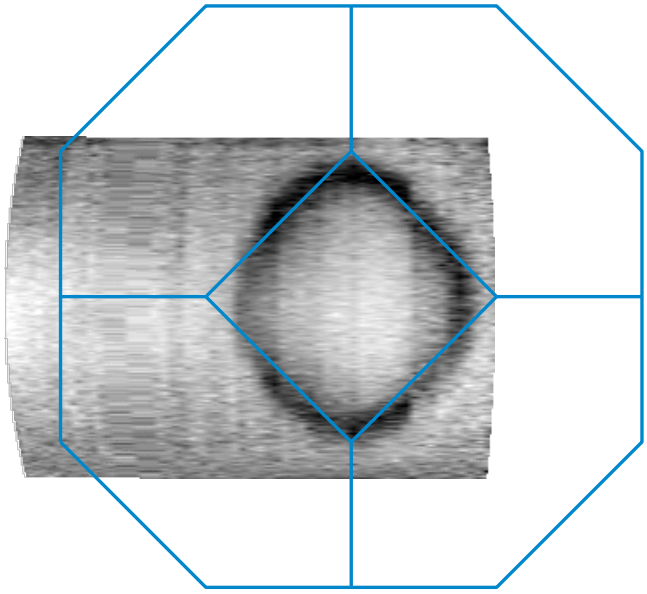

Figure 8.3: Fermi surface intensity map integrated within $E_F \pm 30$ meV, taken at $T = 20$ K after 13 minutes of Cs deposition. Overlaid is the EuO fcc Brillouin zone projected into two-dimensions.

band (*c.f.* Figure 5.3(a)), as can be seen in the Fermi surface intensity map, presented in Figure 8.3. It is clear that the LEP composes a large circular Fermi surface centered at (0,0), and no other features are discernible crossing E_F.

To further investigate the properties of the Cs/EuO system, we now focus on a quantitative analysis of the band dispersion of the LEP. By fitting momentum distribution curves (MDC) with two Lorentzians (Equation 2.25), we extract MDC peak position as a function of binding energy, shown along with the original data in Figure 8.4. The MDC peak positions are subsequently fit by a parabolic band dispersion,

$$E = \frac{\hbar^2 k^2}{2m^*} - E_0, \tag{8.5}$$

where the fitting parameters were found to be $E_0 = 1$ eV and $m^* = 1.0\ m_e$, very close to the thermal mass reported for Cs metal ($1.29\ m_e$) [188]. Such close agreement is suggestive that

the observed features near the Fermi level are at least partially attributable to free-electron-like Cs 6*s* orbitals. This hypothesis is further supported considering that the Fermi surface of Cs is nearly perfectly spherical [189], and centered at Γ in the Brillouin Zone.

To assess the degree of out-of-plane (k_z) dispersion, we compare the extracted MDC dispersion of the LEP taken with both He Iα and He IIα photons. The dispersion curves, shown in Figure 8.4(b), are nearly identical, implying that the LEP does not disperse in k_z direction, and rather is representative of two-dimensional charge carriers. Considering both the absence of k_z dispersion and the effective mass determined above, we denote this system as a two-dimensional free electron gas. Given the two-dimensional nature of the LEP Fermi surface, the area enclosed by the surface in Figure 8.3 can be used in conjunction with Luttinger's theorem [152, 153] to compute the charge carrier density of this Fermi surface sheet. Assuming non-spin polarized charge carriers, the average Fermi wavevector (0.49±0.04 Å^{-1}) corresponds to a 2D charge carrier density of $N_{2D} = k_F^2/2\pi = 3.82 \pm 0.6 \times 10^{14}$ cm^{-2} or 0.52 ± 0.08 electrons per Eu atom.

8.4 Surface Crystal Structure

From our results in §8.2-8.3 we have established the presence of a thin layer of Cs on the EuO surface and that this layer results in significant changes in the electronic properties measured by photoemission. We now address the structural aspects of this adsorbed Cs layer. Our Fermi surface map in Fig 8.3 indicated a charge carrier density of ~1/2 electron per Eu atom, alluding to the potential presence of an ordered Cs overlayer. While it may seem surprising that a material deposited at cryogenic temperatures would result in an ordered phase, the high surface diffusivity of alkali metals has been established previously [190] and Cs atoms have been shown to form ordered phases previously on other metallic substrates when deposited at temperatures as low as 100 K [191].

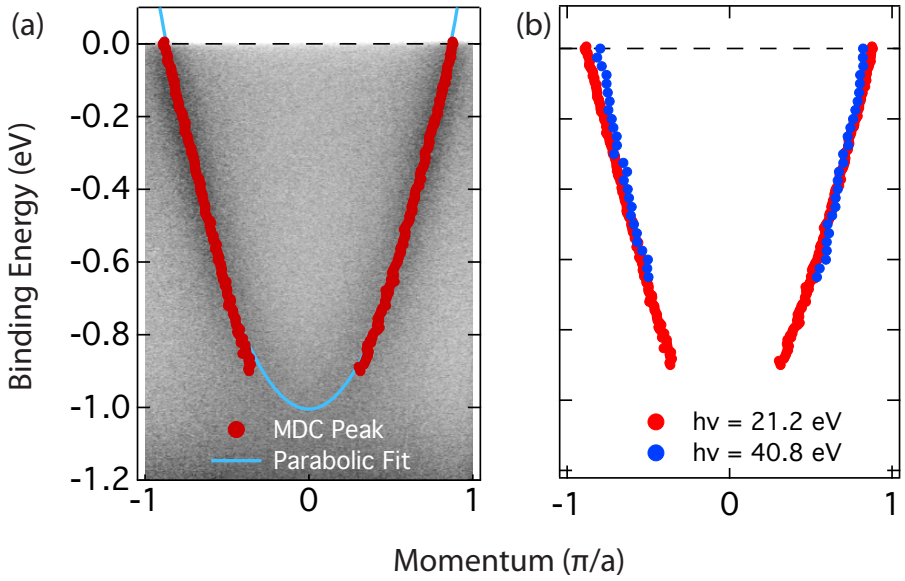

Figure 8.4: (a) Extracted band dispersion of the LEP (data taken with 21.2 eV photons) overlaid with a parabolic fit. (b) Comparison between band dispersion taken at $h\nu$ = 21.2 eV and 40.8 eV.

The presence of such an ordered phase would result in a change in the low-energy electron diffraction (LEED) pattern, which is sensitive to the surface crystal structure. For example, in Figure 8.5, we show a schematic version of the (001) EuO crystal in both real and momentum-space. We additionally show the (001) EuO surface with additional cesium atoms on top in an ordered phase which would give rise to a measured charge carrier density of 1/2 electron per Eu atom (note that while the Cs atoms are depicted to reside on the Eu sites, this is not strictly necessary, as any uniform translation of all Cs atoms relative to the EuO would not alter the density). For an ordered Cs surface like that depicted in Figure 8.5, the unit cell is enlarged by $\sqrt{2} \times \sqrt{2}\mathrm{R}45^\circ$ relative to the original EuO unit cell. This would result in a reconstruction of the reciprocal lattice, also illustrated in Figure 8.5.

In Figure 8.6 we present LEED images for a pristine $Eu_{0.96}La_{0.04}O$ sample, along with a sample with Cs deposited on it. Both images are nearly identical, strongly suggesting that the Cs overlayer makes no modification to the surface crystal structure. Notably, we cannot identify the presence of any extra spots which would be indicative of the ordered phase

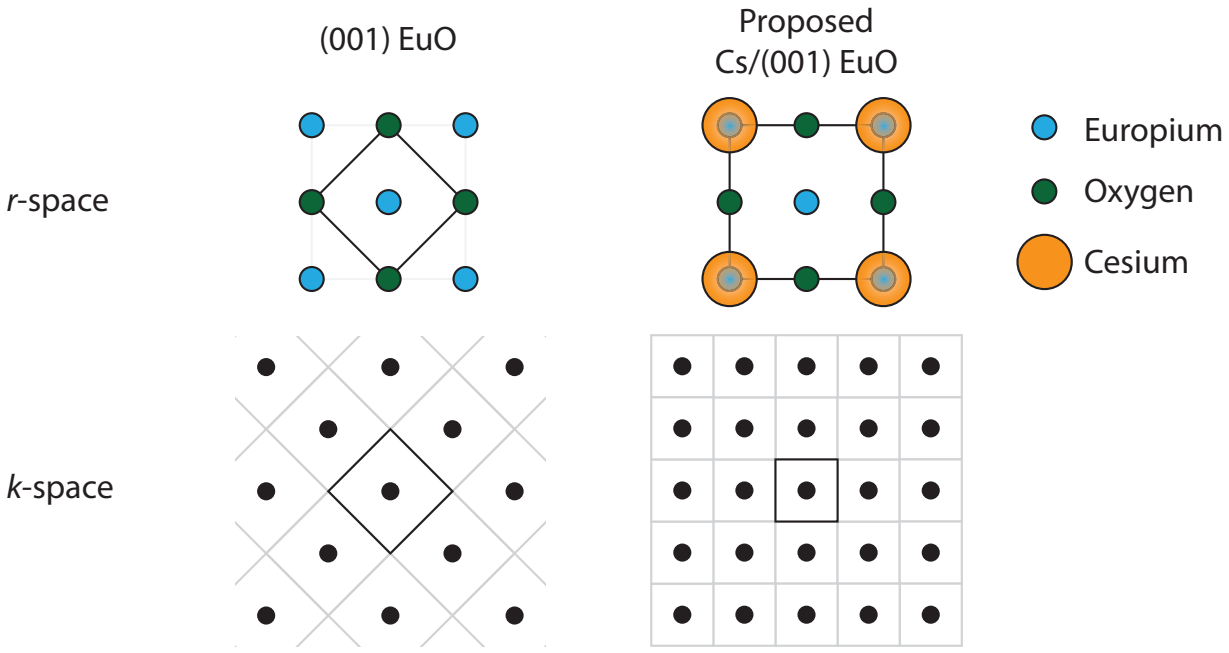

Figure 8.5: (top left) Surface atomic structure of a (001) EuO crystal face, with primitive 2D unit cell illustrated by the dark square, and (bottom left) the corresponding reciprocal space lattice, with the first Brillouin Zone indicated by the black square. (top right) Proposed crystal structure of (001) EuO after Cs deposition, with a $\sqrt{2} \times \sqrt{2}$R45° enlarged unit cell, and which yields a carrier density of 1/2 electron Eu atom. The Cs atoms have been made transparent to show the underlying Eu atoms. (bottom right) Reciprocal space structure of the proposed ordered Cs surface, with first Brillouin Zone illustrated by the black square. Note that the Cs atoms need not sit directly on top of the Eu sites, as any translation of all Cs atoms would not change the reciprocal space unit cell dimensions.

discussed above. In contrast, a second possibility is that Cs forms a polycrystalline or amorphous layer which produces a uniform intensity across the entire LEED detector, and which is undetectable when superimposed with the diffraction pattern of the underlying EuO film. While LEED is a surface sensitive measurement technique, it is no more surface sensitive than ARPES, and many of the spectral features of EuO are still observable even after deposition of Cs onto the film (see e.g., Figure 8.1). If one considers that the Pauling metallic radius for Cs is 2.67 Å [192], just 2% larger than the Eu-Eu lattice spacing (2.62 Å) in the surface unit cell of EuO grown on $YAlO_3$, it seems plausible that a disordered Cs phase could be present, and the fact that the Luttinger count yields a half-integer carrier density per EuO unit cell is purely coincidental. Nevertheless, such a scenario would likely result in a broadening of the diffraction spots due to increased scattering (as seen in the photoemission spectra), and this does not seem to be apparent in the LEED images shown in Fig 8.6. It would be useful to conduct a comprehensive LEED I-V study (such as that described in Appendix A) to assist in surface crystal structure determination of Cs/EuO, however these measurements have not been carried out to date. Furthermore it would be beneficial in future experiments to iteratively measure samples using photoemission and LEED to determine whether the LEED electron beam produces any unintended effects on the structure of the Cs adlayer, preventing the detection of an ordered phase.

8.5 Cs Coverage-Dependent EuO Valence Band Shift

Perhaps the most intriguing part of the Cs/EuO system is the behavior of the EuO valence band. Shown in Figure 8.7, we find that with the addition of excess Cs, the Eu $4f$ band shifts *toward* E_F by as much as 330 meV. In a simple rigid band picture, alkali metal deposition is used as an n-type dopant and the opposite behavior is expected: the n-type dopant would induce a chemical potential shift and the valence band consequently shifts away from E_F to

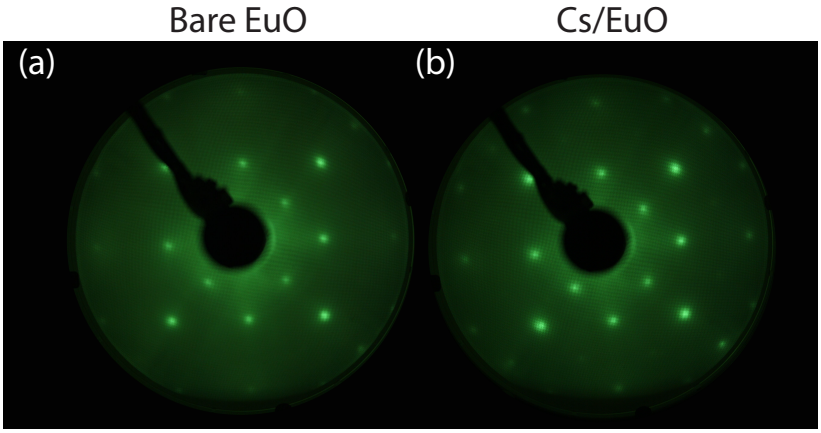

Figure 8.6: LEED Images of (a) a pristine $Eu_{0.96}La_{0.04}O$ surface taken at T = 300 Kand (b) an $Eu_{0.96}La_{0.04}O$ surface following the deposition of Cs for 13 minutes and measured at T = 60 K, showing a well-ordered surface devoid of any superstructure. In both cases the electron beam energy is 220 eV.

accommodate the extra charge carriers. We discuss the potential origin of this behavior below.

The exact nature of the interaction between a metallic substrate and an alkali metal adlayer is a contentious subject, and there has been a substantial body of work published in the literature with no clear consensus. While the the Langmuir-Gurney model of ionic donation, described in the beginning of this Chapter, was the *de facto* explanation for these systems for decades, the accuracy of this ionic donation picture was questioned in the early 1990s, primarily a result of the of the work by Ishida and Terakura (IT). IT used first-principles calculations [193] for Na on Al(001) and found that the interaction between adsorbate and substrate is best described as covalent, with the electron density primarily concentrated within the adsorbate layer, rather than within the substrate. Schefler *et al.* [194] subsequently argued that the ionic picture is in fact accurate, though only in the low coverage regime. Much of the debate regarding the nature of the interaction between adsorbate and substrate has centered around discussion of coverage-dependent surface core-level shifts observed by Wertheim and collaborators in photoemission measurements of

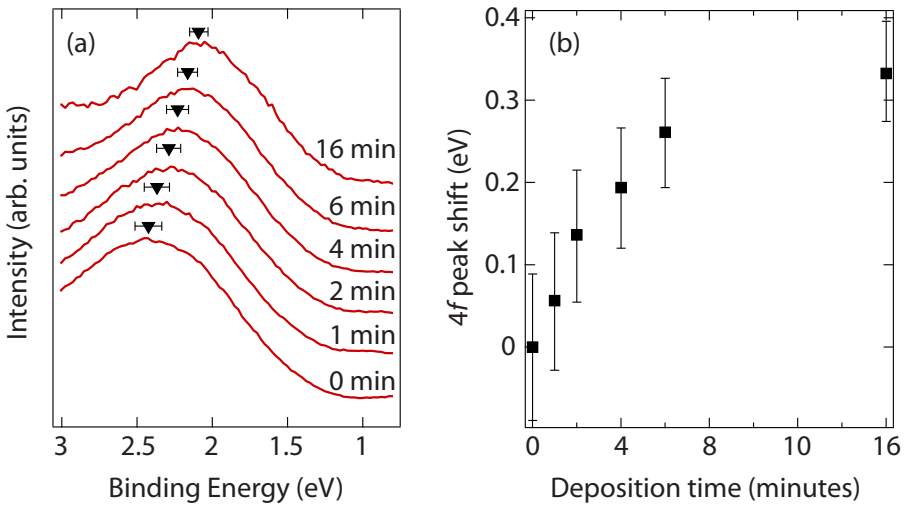

Figure 8.7: (a) Eu $4f$ valence band (vertically offset for clarity) for various Cs deposition times. Cs was deposited and spectra were acquired at $T = 20$ K. (b) Relative shift in Eu $4f$ peak position as a function of Cs deposition time.

alkali metals adsorbed on metallic substrates. The most heavily studied system is W(110) [195, 196], although these measurements have been extended to other systems such as Ta(110) [197]. Wertheim *et al.* found that the substrate (e.g., W $4f$) surface core level shifts non-monotonically, and often to lower binding energy by ~ 25 meV as a function of alkali metal deposition.

A proposed explanation of this behavior is that the energy of the surface core level can be expressed as a sum of multiple components [197, 198],

$$\Delta_{\mathrm{SCS}} = \Delta_{\mathrm{env}} + \Delta_{\mathrm{config}} + \Delta_{\mathrm{ct}} + \Delta_{\mathrm{hybrid}} + \Delta_{\mathrm{relax}} \tag{8.6}$$

where Δ_{env} is an environmental component, accounting for internal charge redistribution within the substrate, Δ_{config} is a configurational component, accounting for the presence of the alkali nucleus on the substrate surface, Δ_{ct} is the charge transfer component, Δ_{hybrid} accounts for the hybridization between alkali metal s orbitals with the substrate valence and conduction band (i.e., covalent bonding), and Δ_{relax} accounts for screening effects from the

overlayer. For the case of Cs on W(110), Benesch and King [198] calculate the contribution of many of these components to be several hundred meV in magnitude, but the components differ in sign so that the sum in Equation (8.6) amounts to only a few tens of meV. Such a detailed analysis of the shift in the Eu $4f$ band for Cs/EuO is beyond the scope of this work, although we would note that the charge transfer component Δ_{ct} is likely to be small for this system compared to Cs/W(110), as the work function of EuO (1.8 eV) [74] is small compared to the Cs ionization potential (3.9 eV), implying minimal charge transfer from adlayer to substrate. The absence of this component could explain the relatively large shift toward E_F with increasing Cs coverage.

8.6 Conclusions

In this Chapter we have investigated the effect of Cs deposition on the electronic structure of EuO. Our measurements have revealed that with increasing Cs content, a marked transition is observed from an EuO Fermi surface to one resembling a two-dimensional free electron gas, exhibiting minimal k_z dispersion, but otherwise closely resembling the Fermi surface for Cs metal. Core level spectroscopy reveals the presence of Cs in the few monolayer regime, yet LEED reveals no extra diffraction peaks. Furthermore, we have revealed an unexpectedly large shift in the EuO valence band toward the Fermi level, behavior that is wholly inconsistent with a simple charge transfer/rigid band shift model of alkali metal adsorption.

While our measurements presented here have primarily been limited to the heavily doped (~ monolayer) regime, it is the dilute regime where ionic charge transfer is expected. Investigation of this dilute doping regime is therefore a promising future avenue of research that could potentially circumvent the maximum in charge carrier density seen in chemically doped samples [91] and permit the exploration of the properties of heavily doped EuO.

CHAPTER 9

Properties and growth of $SrRuO_3$ [1]

For the remainder of this thesis, we will focus our attention on a second complex oxide material, $SrRuO_3$. $SrRuO_3$ exhibits a number of similarities to EuO, including ferromagnetism and evidence for strong correlations, yet it also differs in a number of ways. It is intrinsically a metal and it is the itinerant charge carriers which give rise to the magnetism.

In this Chapter we will introduce the properties of $SrRuO_3$ including prior work that has been done on this system, and we will highlight some of the open questions which we will address using photoemission. We will then describe the growth of $SrRuO_3$ thin films[2] using oxide MBE and their subsequent characterization using a number of different techniques, including structural characterization (electron and x-ray diffraction) along with electronic characterization using charge transport and angle-integrated photoemission. We will show that our films are some of the best in existence and we will discuss why such high quality is necessary for characterizing $SrRuO_3$ with ARPES measurements, which will be presented in the next Chapter.

9.1 Introduction to $SrRuO_3$

The Ruddlesden-Popper series [199, 200] of ruthenates $Sr_{n+1}Ru_nO_{3n+1}$ displays a number of remarkable electronic and magnetic properties where ferromagnetic tendencies are

[1] Much of the data presented in this Chapter has been published in D.E. Shai *et al.* Phys. Rev. Lett. **110**, 087004 (2013) and is reproduced here with permission.

[2] All $SrRuO_3$ films described in this Chapter were grown by C. Adamo.

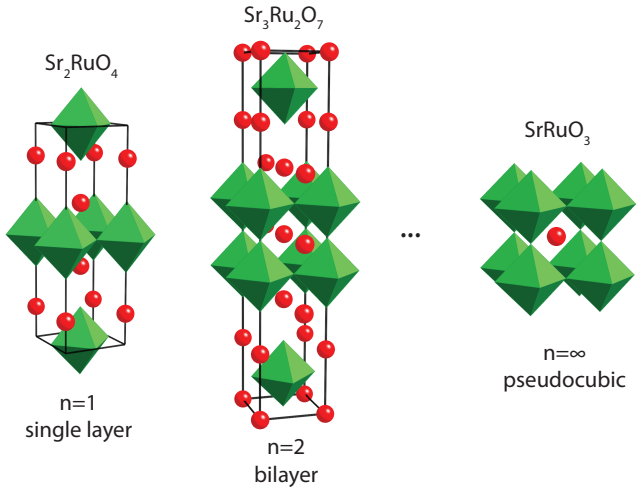

Figure 9.1: Crystal structure of the structure of the Ruddlesden-Popper series of strontium ruthenates, $Sr_{n+1}Ru_nO_{3n+1}$, $n = 1,\ 2, \ldots \infty$.

enhanced by increasing the number, n, of RuO_2 sheets per unit cell. The crystal structure of representative members of this series can be found in Figure 9.1. The single layer $n = 1$ compound, Sr_2RuO_4, is proposed to be an exotic spin triplet superconductor with a time-reversal symmetry breaking ground state [201], while the $n = 2$ $Sr_3Ru_2O_7$ exhibits quantum critical metamagnetism [202] and an electronic nematic ground state near $B = 7.8$ T. The series culminates in the pseudocubic, $n = \infty$ member, $SrRuO_3$, a correlated ferromagnet (FM) with Curie temperature (T_c) 160 K [203] and a low temperature moment of 1.4 μ_B [204], rare for a 4*d* transition metal oxide.

Due to its metallicity, magnetic properties, and epitaxial lattice match to other oxides, $SrRuO_3$ has become one of the central materials in oxide electronics [18], and has been utilized as a conductive electrode for ferroelectrics, Schottky diodes, magnetocalorics, and magnetoelectrics [205–208]. $SrRuO_3$ has even been proposed to support the existence of magnetic monopoles in *k*-space [209] or to form a building block for an oxide superlattice that supports a spin-polarized two-dimensional electron gas [19].

Yet, despite this great interest in utilizing $SrRuO_3$ for applications, a number of

fundamental questions about this material have gone unanswered. There has been significant discussion as to what degree $SrRuO_3$ exhibits strong electron correlations. As a 4*d* TMO, $SrRuO_3$ is expected to have weaker correlations than its 3*d* counterparts, yet the large effective masses reported in specific heat measurements [210] and presence of magnetic order indicate that correlations could be important.

Early optical conductivity data from Ahn *et al.* [211] suggested that correlations were important in $CaRuO_3$ and $SrRuO_3$ due the presence of peaks assigned to optical transitions between a lower and upper Hubbard band (so-called U excitation) and between a quasiparticle peak and lower (upper) Hubbard band ($U/2$ excitation). Such a peak structure is an optical signature of a Mott-Hubbard system, and for the case of $SrRuO_3$ the values of the Coulomb repulsion U and hopping energy W were determined to be 3.23 eV and 1.31 eV, respectively. Such a value of U is smaller, but comparable to many 3*d* TMOs ($U > 4$) [212]. Subsequent optical measurements from compounds including the perovskites (Sr,Ca)RuO_3 and pyrochlore ruthenates $(Y,Bi)_2Ru_2O_7$ over a large energy range (5 meV − 12 eV) showed that electron correlations were much weaker than originally thought, and the value of U was estimated to be ~ 1.7 eV [213].

Similarly, early photoemission measurements by Fujioka [214] showed evidence of strong electron correlations. The amount of spectral weight at the Fermi level was found to be suppressed strongly relative to an "incoherent" peak at 1.2 eV binding energy. Yet this was questioned by later photoemission measurements by Maiti *et al.*[215], who argued that correlation effects were weak in $SrRuO_3$.

Additionally, $SrRuO_3$ is one of the only 4*d* ferromagnetic perovskites. While $SrRuO_3$ has often been interpreted in the context of the Stoner model of itinerant ferromagnetism, previous optical measurements [216] showed little temperature dependence through T_c, and recent magnetometry measurements suggest that the Stoner picture may be inaccurate [217].

Direct access to its low energy electronic structure would be highly desirable to address these open questions pertaining to $SrRuO_3$. Its quasi-2D analogue, Sr_2RuO_4, has been extensively studied using ARPES (see Refs. [218–222] for several examples). As it consists of one RuO_2 layer followed by an insulating double rock salt SrO spacer layer, the electronic structure in this material is primarily two-dimensional, as is confirmed by the large resistivity anisotropy, $\rho_c/\rho_{ab} > 500$ [223]. As a result of its two-dimensional nature and the absence of complicating effects such as ferromagnetism, the Sr_2RuO_4 Fermi surface, shown schematically in Figure 9.2, represents and ideal starting point for our discussion of $SrRuO_3$. The Fermi surface consists of three sheets labelled α, β, and γ. The α and β sheets are derived from the quasi-1D Ru d_{xz} and d_{yz} orbitals, whereas the γ band is derived primarily from the d_{xy} orbital. More recently the bilayer compound has been characterized by ARPES [224, 225], and its resulting Fermi surface maps is significantly more structured due to complicating effects such as bilayer splitting and octahedral roatations. The inability to cleave single crystals of $SrRuO_3$, however, due to its pseudocubic structure, has meant that even a basic understanding of its low-energy electronic structure has remained out of reach.

Our MBE+ARPES approach enables us to grow extremely high quality films of $SrRuO_3$ and subsequently characterize them using ARPES without needing to cleave the samples. In the remainder of this Chapter, we will describe the growth of these films and their measurement using multiple characterization techniques. Following this, in Chapter 10, we will describe our ARPES measurements which characterize the $SrRuO_3$ Fermi surface and address several of the questions described above such as the origin of the large mass enhancement, and the nature of the ferromagnetic order.

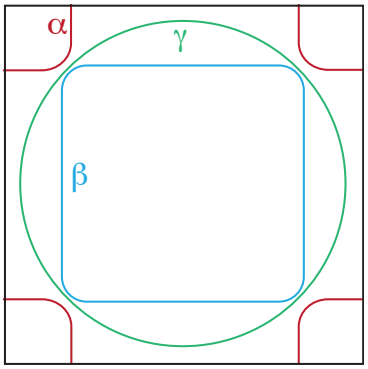

Figure 9.2: Schematic Fermi surface of Sr_2RuO_4, illustrating the three Ru 4*d* t_{2g}-derived Fermi surface sheets (labelled α, β, and γ).

9.2 Film growth

20 nm thick films of $(001)_p$ $SrRuO_3$ (where the subscript p denotes pseudocubic indices) were deposited epitaxially on $(001)_p$ $NdGaO_3$ single crystal substrates in a Veeco GEN10 dual-chamber oxide MBE. During growth the substrate was held at 800 °C and the oxidant (O_2 + 10% O_3) background pressure was held at 8×10^{-7} Torr. Sr was evaporated with a flux of 2×10^{13} atoms/cm^{2}s from an effusion cell and shuttered to provide Sr in sequential doses corresponding to the number of Sr atoms in a SrO monolayer. Note that $SrRuO_3$ grown along the $[001]_p$ growth direction can be considered as alternating monolayers of SrO and RuO_2. In contrast, Ru was evaporated with a flux of 4×10^{13} atoms/cm^{2}s using an electron beam evaporator and supplied continuously during the entire growth. The growth rate was about 0.4 nm/min (1 pseudocubic unit cell per minute) and films were monitored using reflection high-energy electron diffraction (RHEED), described below.

9.3 RHEED

RHEED images were collected along the $[110]_p$ azimuth during growth. RHEED images of the $NdGaO_3$ substrate and $SrRuO_3$ film are shown in Figure 9.3. $SrRuO_3$ films exhibit

prominent Kikuchi lines, indicating good crystalline perfection, which was found to be a strong indicator of the quality of the photoemission spectra (described below).

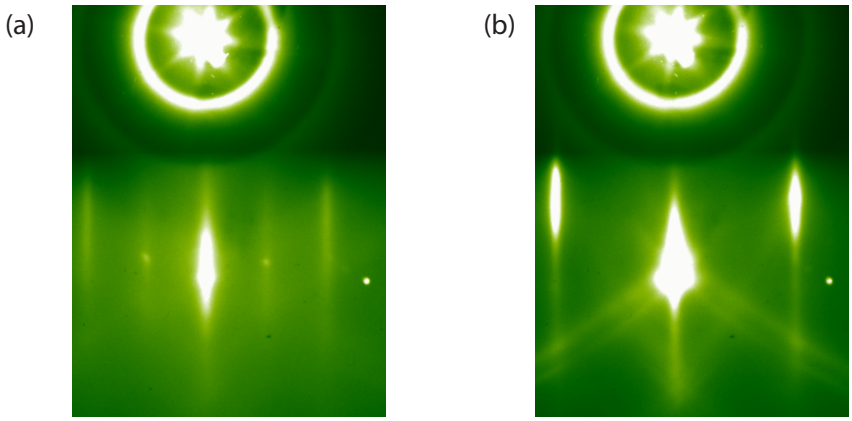

Figure 9.3: RHEED diffraction images taken along the $[110]_p$ azimuth of (a) the bare $NdGaO_3$ substrate and (b) after the growth of a 20 nm thick $SrRuO_3$ film.

9.4 Low-Energy Electron Diffraction

Following ARPES measurements, films were characterized *in situ* by low-energy electron diffraction (LEED). An exemplary LEED pattern is shown in Figure 9.4, taken at normal incidence with a beam energy of 150 eV. The sharp diffraction peaks indicate a well ordered surface crystal structure. The lowest pseudocubic diffraction beams are indicated in the pattern, and the spots appearing at $\sqrt{2} \times \sqrt{2}$ R45° relative to these are a result of the orthorhombic symmetry of the film.

9.5 X-Ray Diffraction

The phase purity and crystallinity of the $SrRuO_3$ films were characterized *ex situ* by four-circle x-ray diffraction (XRD). $\theta - 2\theta$ and rocking curve in ω scans are respectively shown in Figure 9.5(a) and 9.5(b). The full width at at half maximum of the ω-rocking curve of the 002_p film

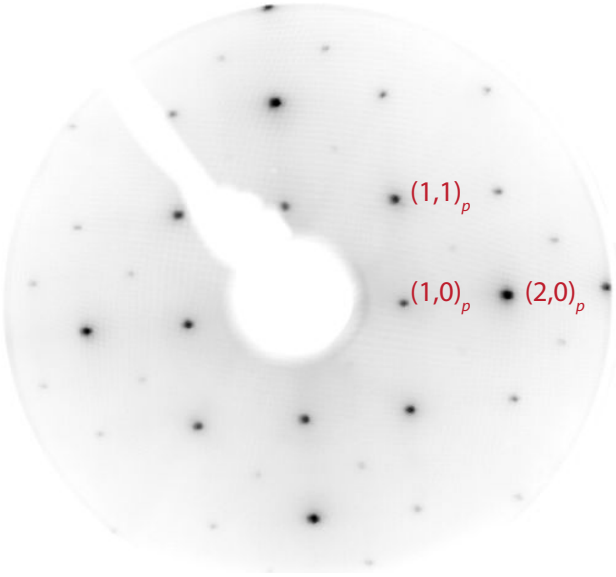

Figure 9.4: Low-energy electron diffraction (LEED) image of $(001)_p$ $SrRuO_3$, taken with an electron energy of 150 eV.

peak was determined to be 22 arcsec, nearly identical to that of the $NdGaO_3$ substrate (18 arcsec), indicating the high crystalline quality of the films. Furthermore, XRD was used to characterize the c axis lattice constant, as described in the next section.

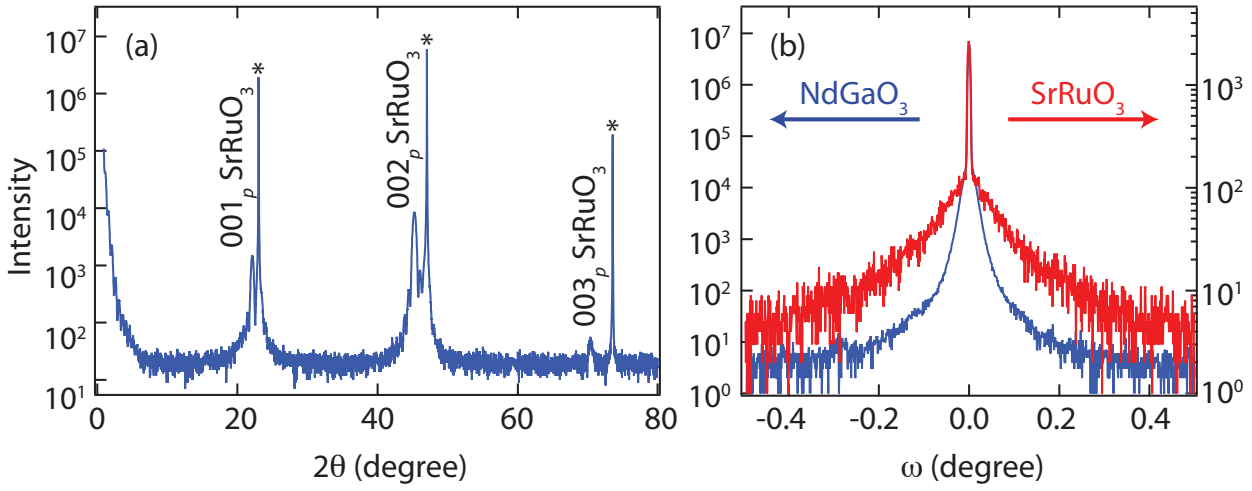

Figure 9.5: (a) X-ray diffraction $\theta - 2\theta$ scan of a 20 nm thick $SrRuO_3$ film grown on $NdGaO_3$. Substrate peaks are marked with an asterisk (*). (b) Rocking curve about the 002_p peak for both the $SrRuO_3$ film and the underlying $NdGaO_3$ substrate.

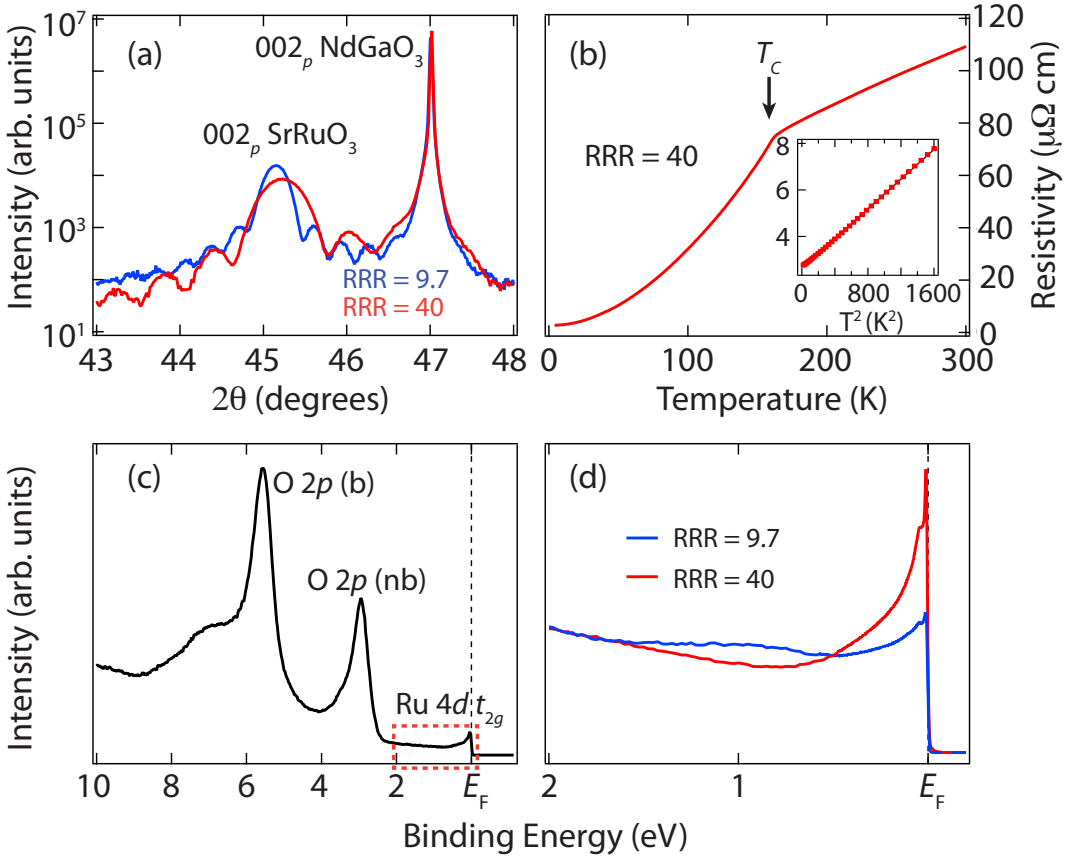

Figure 9.6: (a) X-Ray diffraction $\theta - 2\theta$ scan for two $SrRuO_3$ films showing an elongation of the c lattice constant and lower RRR associated with Ru deficiency. The RRR=40 film is 18 nm thick and the RRR=9.7 film is 24 nm thick. (b) Temperature-dependent resistivity for a $SrRuO_3$ film. (inset) Resistivity showing Fermi liquid T^2 dependence below 40 K. (c) Valence band photoemission near $(k_x, k_y) = 0$ for $SrRuO_3$. (d) Comparison between the near-E_F spectra at $(0, 0)$ from stoichiometric and Ru poor films. Spectra were normalized at 2 eV and were taken in the FM phase (T = 20 - 30 K).

9.6 Ruthenium Stoichiometry

It has been established that the ruthenates are particularly sensitive to disorder [226], and here we show that this has important implications on the photoemission spectra of $SrRuO_3$. As demonstrated by Siemons *et al.* [227], the RRR and the c-axis lattice constant is highly dependent on Ru stoichiometry. We found that only films with the correct Ru stoichiometry, determined from XRD measurements of the c-axis (Figure 9.6(a)), would exhibit a high residual resistivity ratio (RRR = ρ_{300K}/ρ_{4K}) in transport measurements (Fig 9.6(b)).

Establishing the correct Ru stoichiometry additionally has significant effects on the quality of the photoemission spectra. The valence band of $SrRuO_3$ is shown in Figure 9.6(c). By comparison with existing density functional calculations [214], we can identify the features between 3 and 7 eV as primarily O 2*p* bonding (b) and non-bonding (nb) states, while the peak near E_F can be assigned to the Ru 4*d* t_{2g} orbitals, consistent with results from angle-integrated photoemission [228]. While these large energy features look similar for all samples, near the Fermi level, the photoemission spectral weight is significantly affected by the Ru stoichiometry. Only for stoichiometric films, we observe sharp dispersive QP peaks near the Fermi level (Figure 9.6(d)) at low temperatures, where the resistivity follows the expected Fermi liquid T^2 dependence (Figure 9.6(b)). For Ru-deficient films, we find the quasiparticle peak and density of states at the Fermi level are suppressed strongly, and spectral weight is transferred to higher binding energies (1 eV). This strong dependence of spectral features on sample quality underscores the necessity of utilizing oxide MBE, which produces thin films of $SrRuO_3$ with the highest RRR. For comparison, in Table 9.1 we have compiled the highest reported RRR for $SrRuO_3$ found in the literature. The highest reported RRRs in thin films grown by other deposition techniques such as pulsed laser deposition or sputtering are 8 and 4, respectively [229, 230].

9.7 Conclusions

In this Chapter we have reviewed some of the properties of the 4*d* perovskite itinerant ferromagnet $SrRuO_3$. In contrast to its quasi-2D counterparts, $SrRuO_3$ has a fully three-dimensional structure which lacks a natural cleavage plane and therefore requires thin films for use with ARPES. We have proven that our films are of extremely high quality through a combination of x-ray diffraction, charge transport, and electron diffraction measurements,

[1]MAD = metalorganic aerosol deposition
[2]PLD = pulsed laser deposition

Table 9.1: Compilation of highest reported residual resistivity ratios for $SrRuO_3$, illustrating the large variety of sample quality.

Work By	RRR	Method	Thickness	Substrate
Alexander *et al.* [231]	140	Self-flux	bulk	N/A
Cao *et al.* [232]	51	Self-flux	bulk	N/A
Mackenzie *et al.* [233]	60	MBE	~100 nm	Vicinal (001) $SrTiO_3$
Klein *et al.* [234]	45	MBE	80-200 nm	Vicinal (001) $SrTiO_3$
This work	40	MBE	16 nm	(110) $NdGaO_3$
Schneider *et al.* [235]	29	MAD[1]	40-50 nm	(001) $SrTiO_3$
Siemons *et al.* [227]	26	MBE	20-30 nm	(001) $SrTiO_3$
Chu *et al.* [230]	8.4	PLD[2]	100 - 150 nm	(001) $LaAlO_3$
Siemons *et al.* [227]	7	PLD	20-30 nm	(001) $SrTiO_3$
	⋮			

and that this high quality is necessary to extract accurate photoemission measurements. In the next Chapter we will measure these films using ARPES and discuss the nature of the Fermi surface, many-body interactions, and ferromagnetism.

CHAPTER 10

Electronic structure and Ferromagnetism in $SrRuO_3$[1]

In this Chapter, we report the first high-resolution ARPES measurements of $SrRuO_3$. A mapping of the Fermi surface (FS) reveals a number of sheets composed of well-defined quasiparticle (QP) states. We observe a prominent kink in the low-energy QP dispersion characteristic of coupling to bosonic modes, indicating that the large effective masses reported in this material are a result of electron-boson interactions. Finally, we track the temperature dependence of the electronic structure from 20 K through T_c and find that while the QPs lose coherence, they do not shift appreciably, indicating the ferromagnetic exchange splitting remains nonzero above T_c in contrast to the expectations of itinerant Stoner FM. These findings suggest that local moment FM is more appropriate for describing $SrRuO_3$.

10.1 Experimental Details

Experimental details of the growth and characterization of the $SrRuO_3$ films are described in §9.2-9.6. After growth, samples were immediately (< 300 seconds) transferred through ultrahigh vacuum to a high-resolution ARPES system consisting of a VG Scienta R4000 electron analyzer and a VUV5000 helium plasma discharge lamp and monochromator. Measurements were performed using an energy resolution of 10 meV, He Iα ($h\nu$ = 21.2 eV) photons, and base pressure of 8×10^{-11} Torr.

[1]Much of the data presented in this Chapter has been published in D.E. Shai *et al.* Phys. Rev. Lett. **110**, 087004 (2013) and is reproduced here with permission.

10.2 Fermi Surface

The fermiology of FM $SrRuO_3$ is expected to be complex. In Sr_2RuO_4, each Ru atom contributes 3 partially filled 4*d* t_{2g} bands (Figure 9.2). Due to octahedral rotations, there are 4 Ru atoms for each $SrRuO_3$ unit cell, resulting in 12 t_{2g} orbitals, which would be doubled to 24 from the FM splitting. Additionally, calculations by Santi *et al.* [236] suggest that the e_g orbitals may also be partially filled. In Figure 10.1 we show a Fermi surface (FS) intensity map, and in Figure 10.2 we show a truncated version of the same map along with the underlying E vs. k spectra. A number of FS sheets are evident, including two large rectangular sheets which are reminiscent of the quasi-1D, $d_{xz,yz}$-derived α and β sheets present in Sr_2RuO_4, which we denote as α_1 and β_1. Particularly around $(2\pi/3, 2\pi/3)$ (with respect to the pseudocubic Brillouin zone), near where the α_1 and β_1 sheets meet, we observe a large number of band crossings, which result in numerous small FS pockets. Earlier Shubnikov–de Haas (SdH) [233] and de Haas-van Alphen (dHvA) [231] measurements both resolved a coexistence of large and very small FS sheets, which we have tabulated in Table 10.1, and which are consistent with the large β_1 sheet and the small pockets that we observe near $(2\pi/3, 2\pi/3)$. We find the area enclosed by the β_1 sheet to be 1.02 Å^{-2}, in good agreement with the 10.5 kT (1.00 Å^{-2}) orbit reported in Ref. [231]. The area enclosed by the α_1 pocket is approximately 0.37 Å^{-2}, close to the 3.5 kT (0.33 Å^{-2}) orbit in Ref. [233]. While our measurements probe only a single value of the out-of-plane momentum (k_z), we expect them to accurately represent the features of the α_1 and β_1 sheets, which likely exhibit little k_z dispersion along large sections of the Brillouin zone due to their apparently quasi-1D nature. A detailed discussion of the complete, complex three-dimensional fermiology will follow in a future paper.

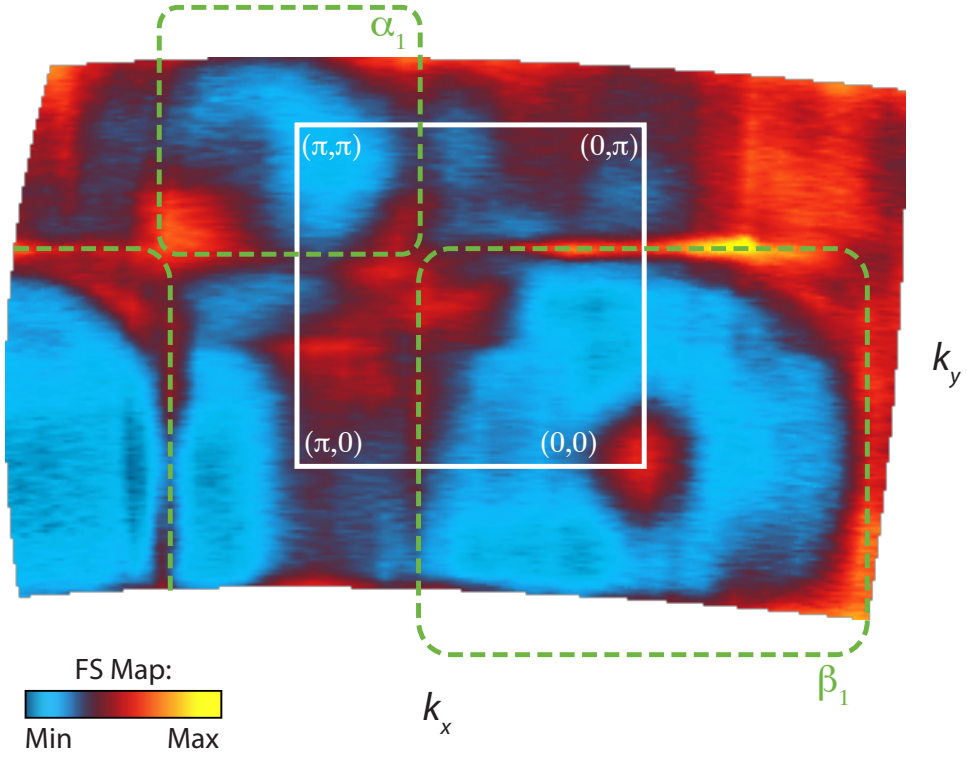

Figure 10.1: Unsymmetrized FS map for $SrRuO_3$ at T = 20 K integrated within $E_F \pm 5$ meV. The FS was normalized to a linearly increasing background in k_x to account for a slowly varying change in net intensity.

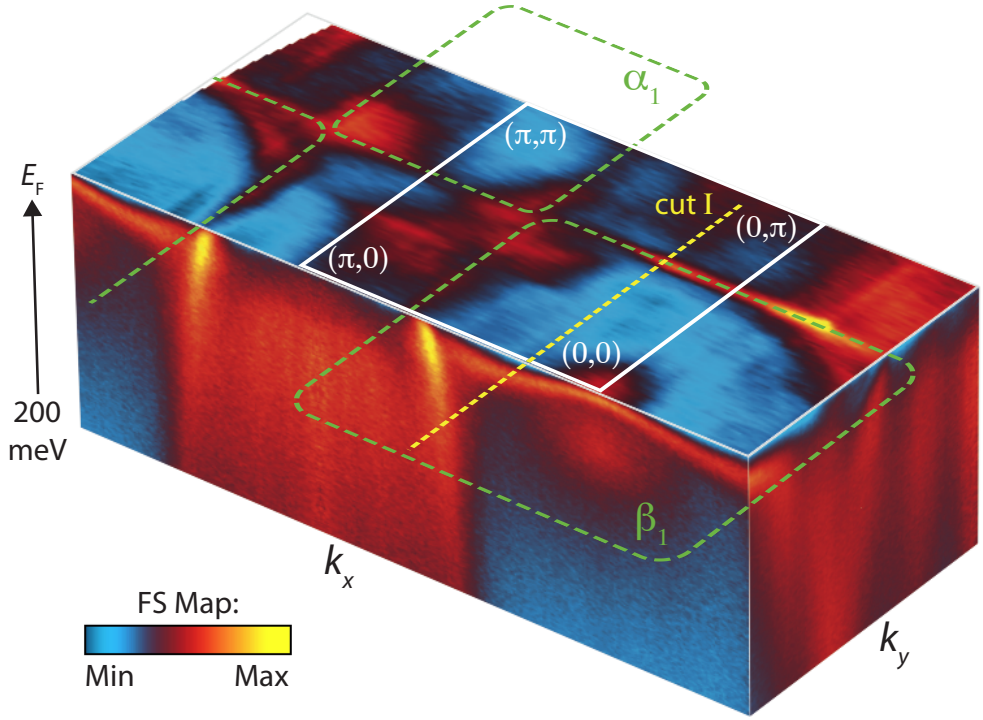

Figure 10.2: Same as Fig 10.1, along with E vs. k_x, k_y spectra illustrating the underlying bandstructure. E vs. k data were taken at symmetry equivalent locations in the Brillouin zone, are symmetrized for values of $k_x > \pi/a$, and are plotted on separate intensity scales (not shown) for illustrative purposes.

10.3 Many-body Effects

In order to address the nature of the many-body interactions in $SrRuO_3$, we focus on the momentum region marked as cut I in Figure 10.2, as this is where the β_1 band appears to be most separated from the other bands and thus is best suited for a detailed analysis. The spectra in this region are shown in Figure 10.3(a) and (c), and exhibit a sharp QP peak at E_F, deep in the T^2 Fermi liquid (FL) regime (Figure 9.6(b)). This is also consistent with SdH measurements [233] that indicated the low-temperature ground state of $SrRuO_3$ is indeed FL-like. We extract the dispersion of the β_1 band using a momentum distribution curve (MDC) analysis, shown in Figure 10.3(b). The dispersion is then fit to a quadratic polynomial

Table 10.1: Fermi surface sheets for $SrRuO_3$ extracted from quantum oscillations.

Work By	Frequency (T)	FS Area (10^{14} cm^{-2})	Effective Mass (m_e)
Mackenzie *et al.* [233]	34	0.32	0.2
	1500	14.3	4.5
	3500	33.4	6.1
Alexander *et al.* [231]	118	1.13	5.1
	364	3.47	6.0
	1015	9.68	5.5
	1015	9.68	5.5
	1500	14.31	6.9
	10486	100.01	4.1
	1110	10.59	4.1
	13	0.12	—

to account for the intrinsic curvature of the band over a wide energy range. An abrupt kink in the dispersion is evident around 65 meV binding energy. We also observe a prominent increase in the MDC width (W_k) at the same energy, indicating a sudden increase in the imaginary part of the self-energy, $\Sigma''(\omega) = -v_F \cdot W_k$, shown in Figure 10.3(e). The observation of a sharp kink in the dispersion with a corresponding increase in the scattering rate is a classic signature of strong electron-boson interactions. To further support this assignment, we extract the real part of the self-energy, $\Sigma'(\omega)$ by subtracting the smooth polynomial dispersion in Figure 10.3(b), and perform a Kramers-Kronig transformation (KKT) of $\Sigma'(\omega)$ to obtain $\Sigma''(\omega)$. (To do this, we assume that $\Sigma'(\omega)$ is antisymmetric about $\omega = 0$, and then perform a discrete Fourier transform to calculate the KKT in Fourier space, as described in Ref. [237].) We show in Figure 10.3(d), (e) that the self-energy extracted directly from the dispersion $\Sigma''(\omega)$ matches closely to the self-energy computed from the KKT, $\Sigma''_{KK}(\omega)$, aside from a constant offset and a slight decrease in the change in scattering rate with ω, which we attribute to impurity scattering and finite instrumental resolution effects, respectively. This

close agreement indicates that our self-energy analysis is not only self-consistent, but that this kink arises from many-body interactions and is not an artifact of band crossings or hybridization.

Electronic specific heat measurements [210] show a large mass renormalization of $m^*/m_b \approx 4$, where the band mass, m_b, was determined from density functional calculations. Although early angle-integrated photoemission [214] and optical conductivity measurements [211] suggested that electron-electron interactions might be responsible for the large effective masses, later optical [213] and angle-integrated photoemission measurements [215] indicate that electron-electron interactions could be relatively weak. Our observation of an abrupt kink in the β_1 band provides direct evidence that strong electron-boson coupling in $SrRuO_3$ is a dominant factor in the large observed effective masses. This is consistent with recent first principles calculations which suggest weak electronic correlations in $SrRuO_3$ [238]. By comparing the bare velocity v_F (from our polynomial fit) to the renormalized v_F^* (computed from the MDC peak dispersion), we obtain a ratio of $v_F/v_F^* = 1.9 \pm 0.2$; by performing a more conventional analysis where we fit straight lines to the dispersion between 100 and 150 meV and between ±10 meV of E_F, we extract an even larger quantity of $v_{HE}/v_F^* = 5.5 \pm 0.5$. We believe that the former analysis provides a more accurate estimate of the true velocity renormalization and in a weak-coupling scenario results in a mass renormalization, m^*/m_b, of 1.9, which places $SrRuO_3$ well into the strong-coupling regime. Averaging this value around the β_1 sheet, we deduce a sheet-averaged effective mass $m^* = \hbar^2\langle k_F\rangle/v_F^* \approx 3.9 \pm 0.7\ m_e$, in excellent agreement with the dHvA value of $4.1 \pm 0.1\ m_e$ [231] for this sheet.

10.4 Temperature Dependence and Relation to Ferromagnetism

We now discuss the temperature dependence of the electronic structure, concentrating again on the β_1 band. As the temperature is increased, we observe that the sharp QP features on

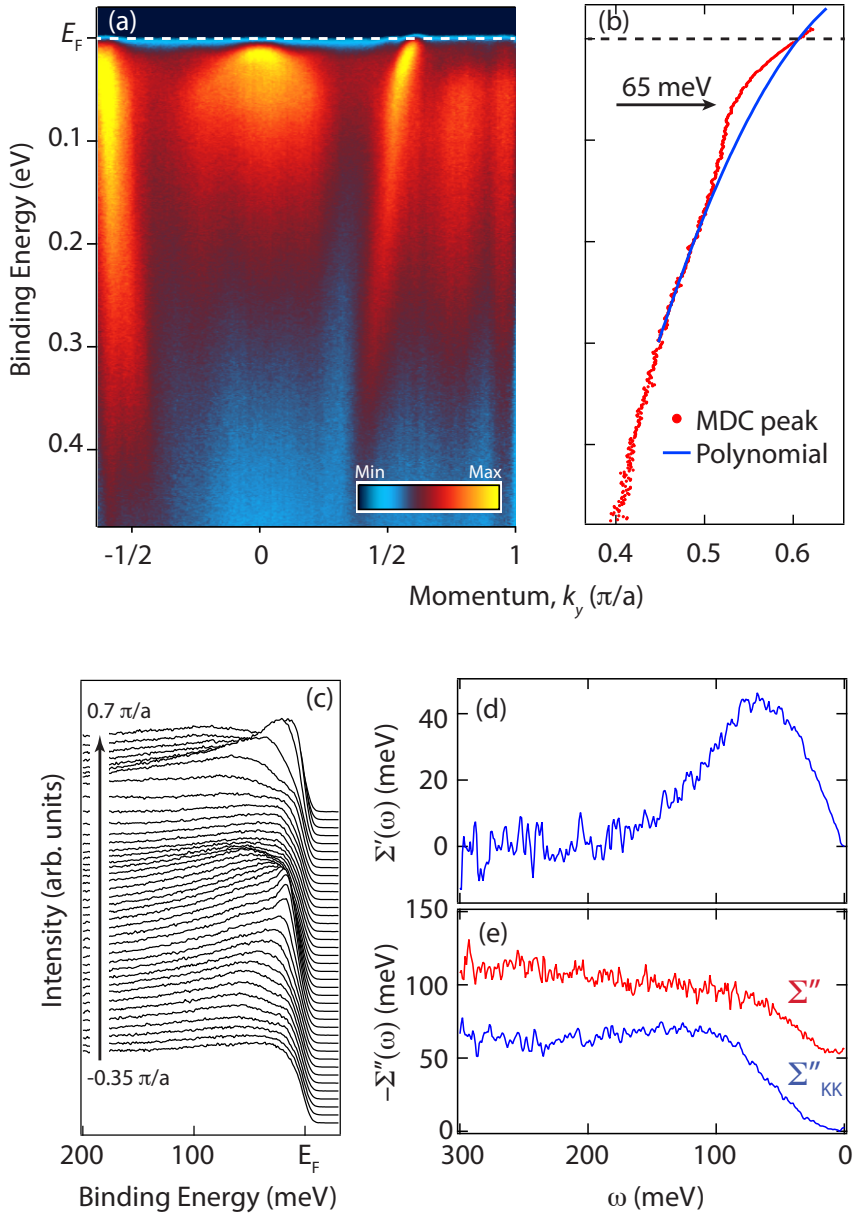

Figure 10.3: (a) ARPES spectral intensity plot taken at $T = 20$ K along cut I (see Figure 10.2). (b) Extracted momentum distribution curve (MDC) dispersion for the β_1 band along with a quadratic polynomial fit approximating the bare band dispersion. (c) Energy distribution curves (EDCs) showing QP peaks in $SrRuO_3$. (d). Real part of the self-energy, $\Sigma'(\omega)$, extracted from the MDC dispersion and polynomial fit in (b). (e) Imaginary part of the self-energy, $\Sigma''(\omega)$, computed from MDC widths, along with the Kramers-Kronig transformation of $\Sigma'(\omega)$, denoted $\Sigma''_{KK}(\omega)$.

the β_1 sheet lose coherence and become significantly broadened, as shown in Figure 10.4(a). Nevertheless, we can still reliably track this band using MDCs from low temperature (19 K) up towards T_c. In Figure 10.4(c) we present MDCs at 200 meV binding energy which clearly show the β_1 band at all temperatures. Even above T_c this band is resolvable as a shoulder to the feature located at 0.7 π/a. We observe the same behavior both upon warming and cooling the sample, excluding the possibility of surface aging as being responsible for this effect. Up to temperatures of 125 K we can reliably track the band dispersion from 200 meV all the way to E_F, shown in Figure 10.4(b). We observe negligible changes in the shape of dispersion, and the kink persists throughout the entire temperature range.

By comparing the average shift in momentum Δk for the extracted dispersion in Fig 10.4(b), we can compute the temperature-dependent energy shift of the β_1 band $\Delta E = \Delta k \cdot dE/dk$, presented in Figure 10.4(d). We find that at 125 K, the β_1 band has shifted by only 27 ± 25 meV from its low temperature value. Within the context of the Stoner model [240], the exchange splitting of an itinerant FM should decrease from its saturation value at low temperatures to zero at T_c, varying proportionally to the bulk magnetization. For comparison, we also include in Figure 10.4(d) the temperature-dependent magnetization [239] which has been scaled to half of the density functional theory-predicted exchange splitting (325 meV, the expected shift per spin population) [241], showing the strong deviation of the bands in $SrRuO_3$ from the expectations of a simple Stoner model. We also did not observe substantial shifts in other bands, although we could not extract their dispersions as reliably as the β_1 band. These results are consistent with earlier bulk-sensitive optical measurements where a corresponding small shift of only 40 meV (of which only a maximum of 10 meV could be attributed to the exchange splitting) was reported upon warming to 140 K [216], and with recent magnetization measurements which showed deviations from the Stoner model across a series of perovskite ruthenates, ARuO$_3$ (A = Ca, Sr,

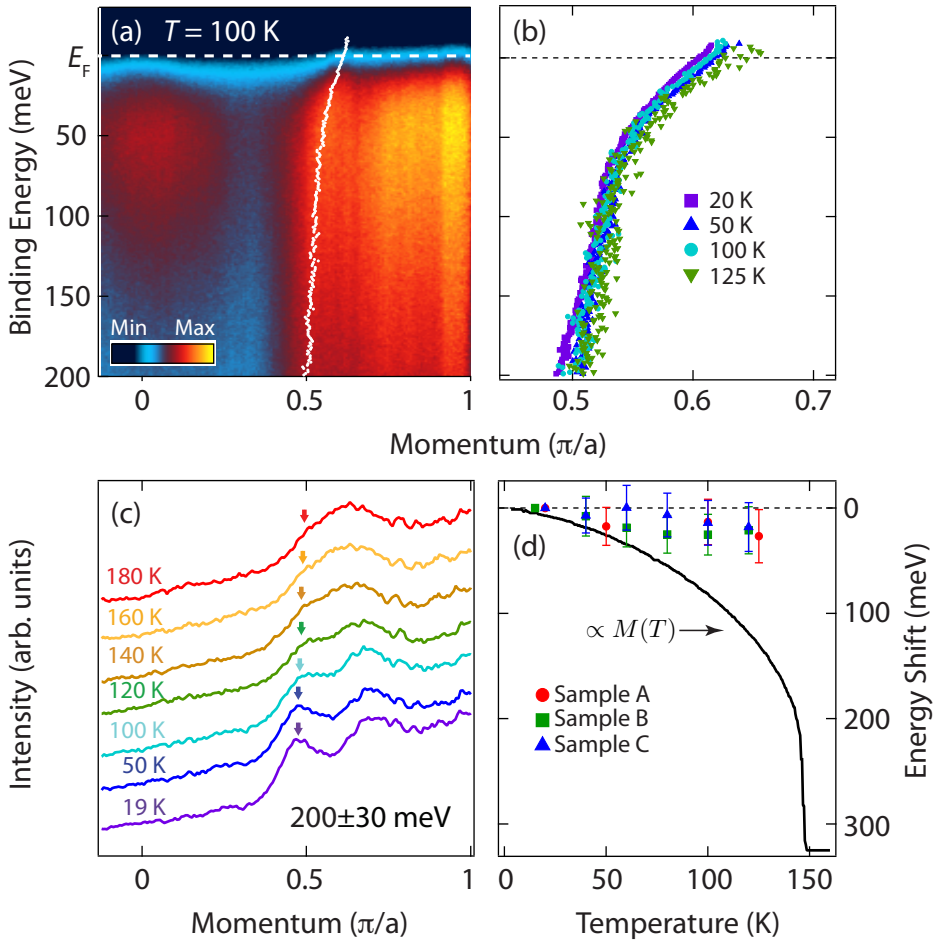

Figure 10.4: (a) ARPES spectral intensity plot taken at T = 100 K along cut I in Figure 10.2. Overlaid is the extracted MDC dispersion. (b) MDC extracted dispersion of the β_1 band at temperatures between 20-125 K. (c) MDCs (offset for clarity) showing the evolution of the β_1 band through T_c. (d) Temperature dependent β_1 band energy shift from multiple ARPES samples and expected energy shift from Stoner FM. Magnetization data was taken from Ref. [239].

Ba) [217]. This agreement between the optical, magnetic, and ARPES measurements clearly points towards a scenario where the magnetism has a local character.

Previous magnetic measurements [242] indicate a ratio of the Curie-Weiss moment to the saturation moment of 1.3, placing $SrRuO_3$ in the category of a more localized moment FM, similar to Fe or Ni. The existing experimental literature on Ni is somewhat complex and possibly conflicting, with some reports showing little change in the spin polarization of Ni through T_c [243], while other work appears to show an exchange splitting which decreases to zero at T_c [244]. Spin-polarized photoemission on Fe reveals exchange split bands with little temperature dependence when heated through T_c [245]. Such observations have led to propositions that these metals retain their local moment above T_c, but lose long-range magnetic order resulting from transverse spin fluctuations [246], which could be consistent with our ARPES results for $SrRuO_3$.

10.5 Conclusions

In summary, our ARPES measurements provide the first insights into the momentum-resolved electronic structure of $SrRuO_3$. Our observation of a kink in the quasiparticle dispersion conclusively demonstrates that strong electron-boson interactions have an important role in the large mass renormalization in $SrRuO_3$. Furthermore, our temperature dependent measurements of the electronic structure suggest that a simple Stoner model cannot adequately describe the magnetism in $SrRuO_3$ and that local moments may play an important role. This new understanding of the electronic structure and quasiparticle interactions is an important step in realizing novel oxide interfaces, electronics, and devices based on $SrRuO_3$.

CHAPTER 11

Conclusions and Outlook

In this thesis, we have described original research performed by investigating the electronic properties of two ferromagnetic oxide thin film materials, EuO and $SrRuO_3$. To accomplish this, we have contributed to the development and construction of a high resolution angle-resolved photoemission spectroscopy system capable of accepting oxide thin films grown by molecular-beam epitaxy, which can be transferred entirely within ultra-high vacuum. The first of its kind, this combination is now being replicated by a number of research groups worldwide. We have utilized this instrumentation to study EuO and $SrRuO_3$ films.

We have discussed the first *k*-resolved electronic structure measurements characterizing the ferromagnetic metal-insulator transition in EuO. By tracking the near E_F spectral intensity as a function of temperature, we have identified three types of charge carriers. In the ferromagnetic metallic state, a portion of the carriers enter the EuO conduction band at X while others occupy relatively dispersionless bound states at the Γ point and are attributed to inactive dopants consistent with Hall measurements. Above T_c, the metallic charge carriers are transferred to a relatively broad but dispersive pseudogapped state at Γ, which through our doping-dependent measurements appear to be a manifestation of semi-localized states: electrons which are neither fully localized nor fully itinerant in real space. Moreoever, our doping dependent measurements of the inactive bound states have revealed a crossover between completely dispersionless and states which exhibit some dispersion but still appear to be localized with no weight at the Fermi level. Additionally, we investigated the

doping dependence of the valence band in EuO and found that the magnitude of the temperature-dependent redshift decreased with charge carrier density, consistent with what has been seen optically. Meanwhile, the magnitude of the energy gap between valence and conduction band appears to decrease with increasing dopant concentration, an effect that, by comparison with first-principles calculations, we have attributed to a dopant-induced lattice strain. Finally, we have explored the effects of externally doping EuO using Cs surface deposition, and we have shown that this results in the formation of an unexpected two-dimensional free electron gas.

Additionally, we have mapped out the *k*-resolved electronic structure of some of the highest quality $SrRuO_3$ in existence. We have revealed a complex Fermi surface consisting of numerous sheets, but still reminiscent of several of the features seen in its two-dimensional counterpart, Sr_2RuO_4. By analyzing the band dispersion near E_F, we have shown that the large effective mass reported by thermodynamic measurements is a result of electron-boson coupling. Finally, by analyzing the temperature dependence of the electronic structure, we have revealed that $SrRuO_3$ doesn't behave as a typical itinerant Stoner ferromagnet as previously suggested. Rather, it exhibits behavior commonly seen in local moment magnets.

There are a number of exciting future avenues of research resulting from this work. For EuO, the most pressing goal is increasing the ferromagnetic Curie temperature, and given the evidence that this is closely related to the charge carrier activation in Gd-doped EuO, further work toward increasing the carrier density would be valuable. To this end, one could explore growth of EuO at lower temperatures in the flux matched regime, as it has already been shown that higher substrate temperatures lead to lower carrier activation [247]. Another option may be to utilize δ-doping, by growing single heavily doped layers embedded within an undoped EuO crystal. Such an approach has been shown to geometrically prevent certain defects and increase dopant activation in traditional semiconductor systems such as Si:Sb [248].

The use of synchrotron-based k_z mapping in photoemission would be greatly beneficial in further elucidating the nature of the states appearing at (0,0) in doped EuO. Such measurements have been achieved recently on undoped samples [249].

Our measurements of the EuO valence band as a function of doping were consistent with a dopant induced strain scenario. These measurements could be extended by exploring the effects of epitaxial strain instead of chemical doping. Epitaxial strain is in many ways a "cleaner" way of exploring these effects, as it neither introduces disorder nor does it modify the charge carrier density.

Further analysis of the charge carriers using real space probes such as scanning tunneling microscopy would be highly beneficial, not only to explore the concept of semi-localized states, but also to gather valuable information regarding the nature of the inactive dopants. Furthermore *in situ* STM could clarify the mysterious structure of the Cs overlayer reported in Chapter 8. There is much to be explored with surface doping of EuO in general, as it could be a promising method to modulate the charge carrier density in a manner similar to field effect gating in devices. In the doping regimes studied thus far, the likelihood of ionic charge transfer is small due to depolarizing dipole fields, and therefore investigation of the more dilute doping regime where ionic transfer is be expected would be beneficial.

$SrRuO_3$ offers many fertile areas of research as well. While our measurements revealed a large number of Fermi surface sheets, our data was taken at a single photon energy and therefore a single k_z value. Synchrotron-based k_z mapping will be crucial to elucidating the entire fermiology in this compound. Along these lines, if one could remove or reduce the amount of octahedral rotations in $SrRuO_3$ it would vastly reduce the number of bands at E_F. One method to do this could be through epitaxial strain. Prior work has shown that strain has significant effects on the rotation pattern in $SrRuO_3$ [250]. Furthermore recent structural measurements have shown that oxygen vacancies also affect the rotation pattern [251].

An alternate method to remove octahedral rotations is to study $BaRuO_3$, which is isoelectronic with $SrRuO_3$, but cubic in structure [252]. $BaRuO_3$ requires a high pressure synthesis, precluding the growth of large single crystals, but it may be easier to synthesize in thin film form. In addition to being perfectly cubic, the ferromagnetic Curie temperature of $BaRuO_3$ is T_c = 60 K, significantly lower than for $SrRuO_3$, which could result in much more clear photoemission temperature-dependence with substantially reduced thermal broadening effects. Moreover $BaRuO_3$ has more clear indications of non-Stoner behavior [217], which would be interesting to study in conjunction with the results presented in this thesis.

Another avenue of research would be to compose a superlattice consisting of $SrRuO_3$ and another cubic perovskite, such as $SrTiO_3$. The $SrRuO_3/SrTiO_3$ system has been studied theoretically by first-principles calculations and has been found to support a spin-polarized two-dimensional electron gas [19]. The combination of MBE and *in situ* ARPES would be ideally suited for investigation of these superlattices.

APPENDIX A

LEED I-V on EuO films

Low-energy electron diffraction (LEED) is a powerful tool for determining the surface crystalline structure of a material. Just as with the determination of bulk crystal structure using x-rays, surface crystal structure determination can be accomplished by analyzing location of Bragg peaks formed when electrons diffract from an ordered structure. The electron diffraction experiment differs from x-ray diffraction by the fact that electrons interact strongly with matter. The inelastic mean free path for low-energy (~ 100 eV) electrons is on the order of 1 nm [42], which for many materials is just 1-2 unit cells. Thus, electron diffraction is sensitive only to the first few unit cells in a material.

Because the elastically scattered electrons interact only with the first few monolayers of a crystal, the diffraction pattern observed in a LEED experiment is determined by a two-dimensional crystal structure at the crystal surface. The points in the normally three-dimensional reciprocal lattice become rods and thus the out-of-plane (k_z) component of the Bragg condition is always satisfied. The diffraction condition is satisfied whenever the electron is scattered with an in-plane momentum transfer that is equal to a 2D reciprocal lattice vector.

While the location of a diffraction peak is determined the in-plane crystal structure of a material, the *intensity* of the these peaks contains more information. The probe electron can elastically scatter multiple times before exiting the crystal. Such multiple scattering processes lead to varying amounts of constructive and destructive interference, which depend on the diffraction order, electron energy, and the crystal being probed. As an example of this intensity variation with beam energy, in Figure A.1 we show experimentally measured LEED

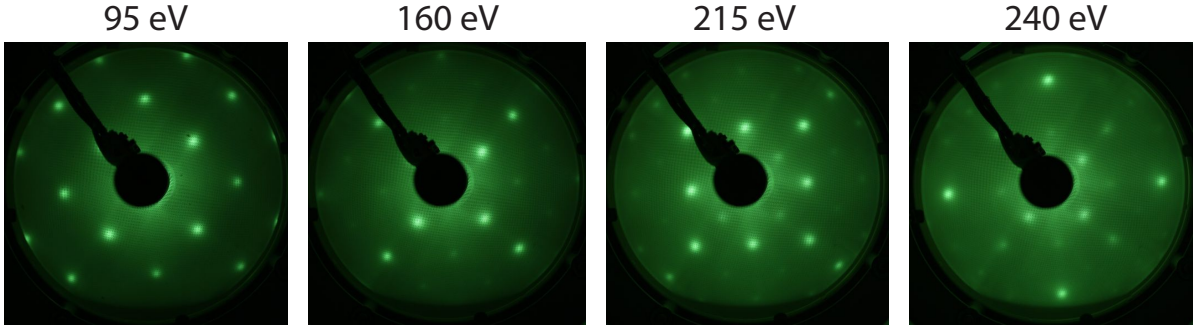

Figure A.1: Example LEED images for $Eu_{0.96}Lu_{0.04}O$ grown on $YAlO_3$, taken for different electron beam energies (indicated at the top of each image).

patterns for a thin film of (001) $Eu_{0.96}Lu_{0.04}O$ for several different electron beam energies. It is clearly visible that the intensity of the different diffraction peaks clearly change with beam energy. The measurement of the diffraction intensity as a function of energy is referred to as LEED I-V.

Due to the complexity of the multiple scattering within a crystal, it is not possible to measure an I-V curve and from that calculate the crystal structure that gives rise to it. By assuming a particular crystal structure, however, the LEED I-V can be simulated. By comparing the results of a such simulations to the experimentally measured I-V curve, and then modifying the starting parameters, the surface crystal structure can be solved in an iterative manner.

Much of the formalism for calculating LEED I-V is described elsewhere in the literature [253–255]. For an electron scattering from an atomic potential, the electron wavefunction consists of an incident plane wave and a scattered wave. If the scattering potential is spherically symmetric the wavefunction is typically written as an expansion in waves with

constant angular momentum l. Using the so-called partial wave expansion, in the region where the scattering potential can be ignored the electron wavefunction is

$$\psi_{\mathbf{k}}(r) = e^{ikz} + k\sum_{l=0}^{\infty} i^{l+1}(2l+1)t_l(k)h^{(1)}(kr)P_l(\cos\theta), \tag{A.1}$$

where $\mathbf{k}$ is the wavevector for the incident plane wave, $h^{(1)}$ is the spherical Hankel function of the first kind, P_l are the Legendre polynomials, and the partial wave amplitude $t_l(k)$ is

$$t_l(k) = \frac{e^{2i\delta_l(k)} - 1}{2ik}. \tag{A.2}$$

The terms $\delta_l(k)$ are the energy-dependent phase shifts experienced by the l component of the wavefunction upon scattering. In the region $kr \gg 1$ the scattered wave reduces to a spherical wave and Equation (A.1) becomes

$$\psi_{\mathbf{k}} \longrightarrow e^{i\mathbf{k}\cdot\mathbf{r}} + f(k,\theta)\frac{e^{ikr}}{r}, \tag{A.3}$$

where the scattering amplitude $f(k,\theta)$ is

$$f(k,\theta) = \sum_{l=0}^{\infty}(2l+1)t_l(k)P_l(\cos\theta). \tag{A.4}$$

The differential scattering cross section

$$\frac{d\sigma}{d\Omega} = \left|f(k,\theta)\right|^2, \tag{A.5}$$

can be integrated over the entire solid angle Ω to get the total scattering cross section:

$$\sigma(k) = \frac{4\pi}{k^2}\sum_{l=0}^{\infty}(2l+1)\sin^2\delta_l(k). \tag{A.6}$$

All of the information specific to a given scattering potential is contained within the partial wave phase shifts, $\delta_l(k)$. Thus the entire scattering problem is reduced to finding the (energy and angular momentum dependent) phase shifts. Once this is achieved, the atoms can be regarded as point scatterers as long as the phase shifts are taken into account. In the following section, we discuss how these phase shifts are calculated for each component of the crystal EuO.

Phase Shift Calculation

A versatile software package for calculating phase shifts for use in LEED calculations has been written by A. Barbieri and M.A. Van Hove [256]. The phase shifts are calculated using three steps, the details of which are expanded upon in the following sections. First, a self-consistent charge density is calculated for each species as a free atom. Second, the scattering potential is constructed using the muffin tin approximation. Finally, the phase shifts are calculated by solving the radial Schrödinger equation and enforcing continuity of the wavefunction.

Radial Charge Density

The first step in determining atomic phase shifts is calculation of the free atom charge density. This is accomplished in the Barbieri/Van Hove software package by means of a relativistic Hartree-Fock calculation. This calculation was performed for both Eu and O free atoms, and the resulting radial charge densities are shown in Figure A.2.

Muffin Tin Potentials

The calculation of the scattering phase shift requires knowledge of the potential of each atom within the crystal. In the Barbieri/Van Hove software package, a muffin tin potential is

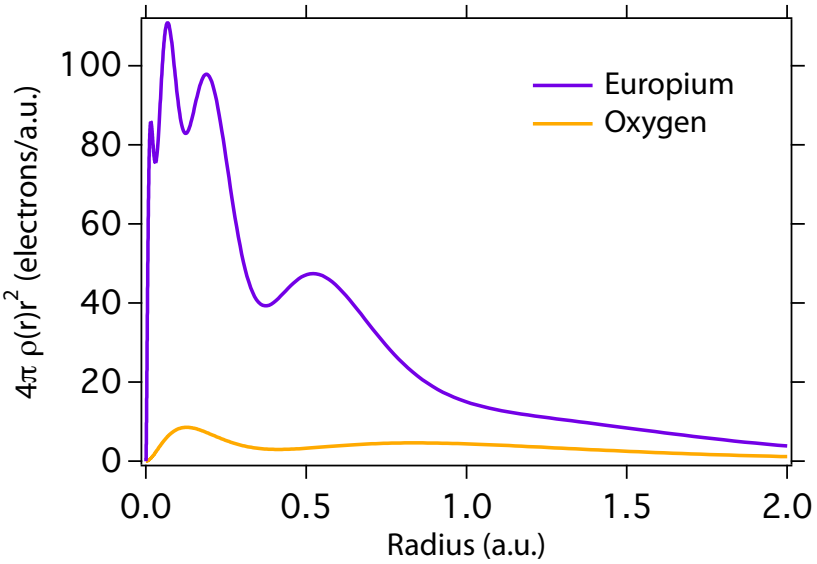

Figure A.2: Radial charge density for Europium and Oxygen atoms.

constructed by the method proposed by Mattheiss [257]. Atomic potentials are arranged on the crystal lattice. A finite radius is defined for each atom, and the potential outside that radius is assumed constant and takes on the value averaged over the entire interstitial region. The potential within the muffin tin radius is given by the atomic potential with an added contribution from neighboring overlapping potentials.

Following this prescription, the muffin tin potentials for both Eu and O in EuO were calculated. The muffin tin radii were chosen to be Eu = 2.50 a.u. and O = 2.28 a.u, based on the results automatically chosen by a commercial density functional theory package [258]. These radii are in close agreement according to the tabulated ionic radii for Eu^{2+} (2.47 a.u.) and O^{2-} (2.38 a.u.) [143], and it was confirmed that the resulting phase shifts are not particularly sensitive to the choice of muffin tin radii. The resulting potentials are shown in Figure A.3.

It should be noted that the constant interstitial potential, known as the inner potential, V_0 (or alternatively is sometimes referred to as the muffin tin constant) differs from the vacuum

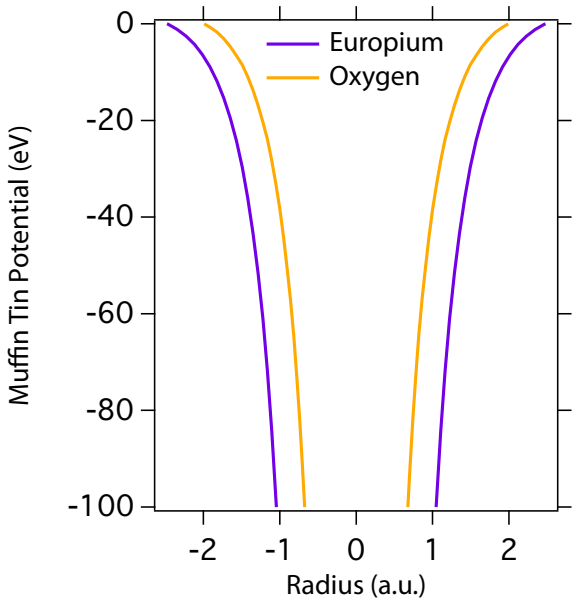

Figure A.3: Muffin tin potentials for Europium and Oxygen in EuO.

and as a result there is a potential barrier at the solid-vacuum interface. The inner potential must be specified in order to calculate LEED I-V curves. Additionally, to account for attenuation of the electron wavefunction as a result of inelastic scattering, the inner potential is taken to be complex: $V_0 = V_{0r} + iV_{0i}$, where V_{0r} is the (positive) real inner potential and V_{0i} is the imaginary part which takes on negative values.

Phase Shifts

Given the muffin tin potentials calculated above, the scattering phase shifts are determined as follows. First, using the expansion

$$e^{ikz} = \sum_{l=0}^{\infty} i^l (2l+1) j_l(kr) P_l(\cos\theta) \tag{A.7}$$

Equation (A.3) can be rewritten as

$$\psi_{\mathbf{k}}(r) = \sum_{l=0}^{\infty} i^l (2l+1) \left[j_l(kr) + ikt_l(k) h_l^{(1)}(kr) \right] P_l(\cos\theta). \tag{A.8}$$

In the above, j_l are the spherical Bessel functions, related to the spherical Hankel functions of the first and second kind by

$$j_l(x) = \frac{1}{2}\left(h_l^{(1)}(x) + h_l^{(2)}(x) \right). \tag{A.9}$$

Equation (A.8) is the wavefunction outside of the muffin tin radius, r_{mt}. We next compute the logarithmic radial derivative $L_l = R_l'/R_l$, where $R_l(r)$ is the radial portion of Equation (A.8). The result is

$$L_l(r > r_{\mathrm{mt}}) = \frac{h_l'^{(2)}(kr) + e^{2i\delta_l} h_l'^{(1)}(kr)}{h_l^{(2)}(kr) + e^{2i\delta_l} h_l^{(1)}(kr)}. \tag{A.10}$$

Within the muffin tin, the radial Schrödinger equation is numerically integrated using the muffin tin potential to produce the radial wavefunction $R_l(r < r_{\mathrm{mt}})$. Continuity of the radial wavefunction and its first derivative is then enforced by equating the logarithmic derivative as r approaches the muffin tin radius from above ($r = r_{mt}^{+}$) and below ($r = r_{mt}^{-}$). This leads to the condition

$$e^{2i\delta_l} = \frac{L_l(r_{\mathrm{mt}}^-) h_l^{(2)}(kr_{\mathrm{mt}}^+) - h_l^{(2)\prime}(kr_{\mathrm{mt}}^+)}{h_l^{(1)\prime}(kr_{\mathrm{mt}}^+) - L_l(r_{\mathrm{mt}}^-) h_l^{(1)}(kr_{\mathrm{mt}}^+)}. \tag{A.11}$$

Equation (A.11) is solved for each value of l and k (energy). The resulting phase shifts encode all necessary information for the atomic scattering problem. The phase shifts for both Eu and

O were calculated based on the muffin tin potentials shown in Figure A.3, and the results are shown in Figure A.4.

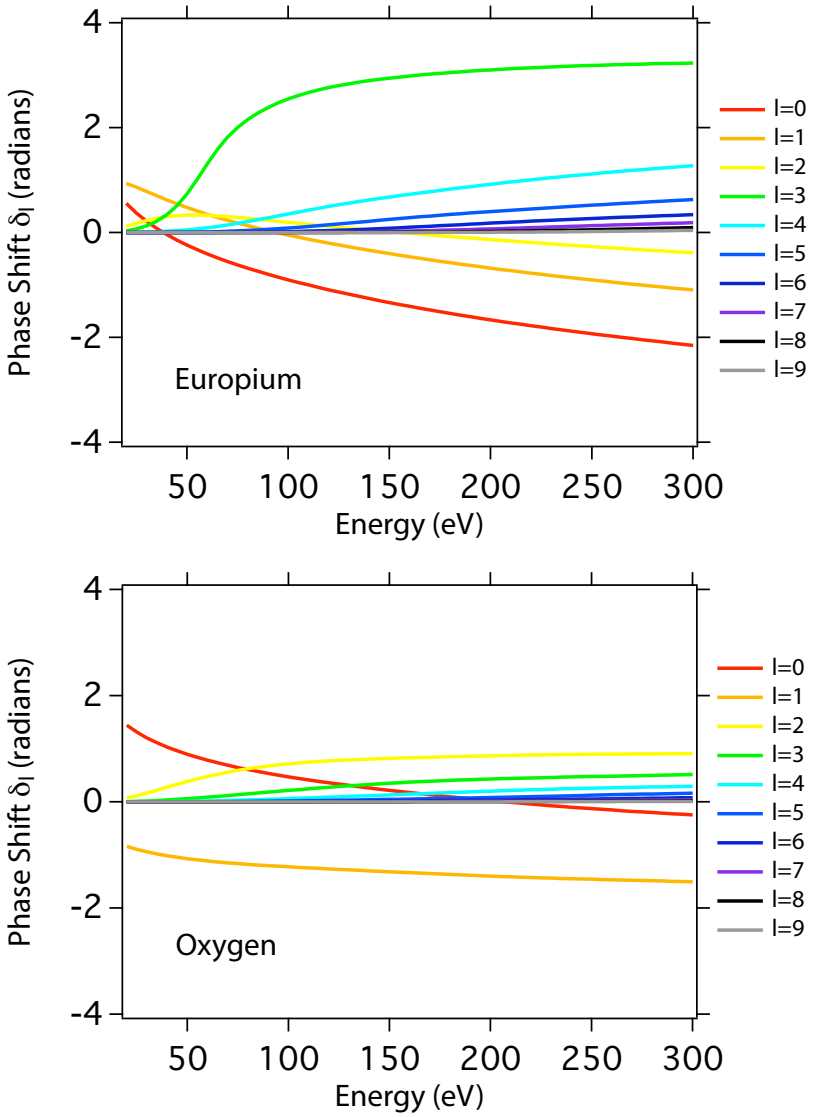

Figure A.4: Scattering phase shifts calculated for Europium and Oxygen in EuO, using Equation (A.11).

The phase shifts become smaller for larger l. This indicates that to a good approximation the infinite sum over l can be truncated without loss of accuracy. As an illustration of the accuracy of this truncation, the total elastic scattering cross section (Equation (A.6)) was calculated for both Eu and O in EuO with an increasing partial wave cutoff parameter, l_{max}.

The results for Eu, shown in Figure A.5, show very little change for $l_{max} \geq 8$. The results for oxygen (not shown) converge for even smaller values of l_{max}. Thus, for the remainder of the calculation, l_{max} was taken to be 8.

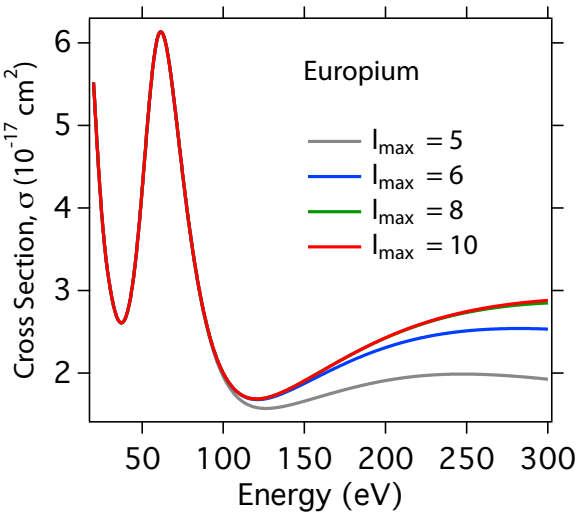

Figure A.5: Total elastic scattering cross section, $\sigma(k)$, for an electron scattering from Europium in EuO for various cutoff momenta, l_{max}. Cross sections were calculated using Equation (A.6).

Dynamical LEED Calculation

Given an accurate set of phase shifts, LEED I-V spectra can now be computed. Accurate LEED intensities require a dynamic (multiple scattering) description, since electrons interact strongly with the crystal lattice. The calculation of LEED intensities is typically broken into two parts: scattering within a plane, and scattering between planes. Intraplanar scattering is treated exactly in a spherical wave representation, whereas interplanar scattering is treated perturbatively in a plane wave representation. A full description of the formalism involved in the dynamical LEED calculation is beyond the scope of this thesis, and so the interested reader is directed to Ref. [259].

LEED I-V calculations were performed using the symmetrized automated tensor LEED (SATLEED) program, developed by M.A. Van Hove and collaborators [260]. The SATLEED

package performs a dynamical LEED calculation given a starting crystal structure, and then, given a set of experimental data, performs a semi-automated search, modifying the crystal structure in order to achieve better agreement between the theoretical I-V curves and the experimental data.

For the present case of EuO, I-V curves were simulated for an epitaxial (001) oriented film coherently strained to a $YAlO_3$ (110) substrate, with an in-plane fcc lattice constant $a = 5.23$ Å (the pseudo cubic lattice of the underlying $YAlO_3$ substrate), and the out-of-plane lattice constant was adjusted to $c = 4.96$ Å to conserve unit cell volume. No surface reconstruction was considered. The real part of the inner potential was set to $V_{0r} = 12$ eV. Inner potentials near 10 eV have historically been shown to produce good experimental agreement with LEED from simple metals, although the applicability to transition metal oxides has been called into question recently. Nasciemento *et al.* [261] found that for the system $Ca_{1.5}Sr_{0.5}RuO_4$, an energy-dependent inner potential, varying between 2 and 7 eV gives the best agreement with experimental I-V curves. Implementing such an energy dependent inner potential is possible with the SATLEED program, but would require some modification of the source code. Without this modification, the (constant) inner potential can be treated as a optimizable parameter to be included in the SATLEED search algorithm. The imaginary part of the inner potential was taken to be $V_{0i} = -5$ eV, a commonly accepted value. The calculated I-V are shown in Figure A.6.

Also shown in Figure A.6 are experimentally extracted I-V curves for a 30 nm $Eu_{0.96}Lu_{0.04}O$ film grown on $YAlO_3$. The Lu dopant served to make the films conducting, which is necessary for LEED measurements. Intensities represent the maximum image intensity for a diffraction spot. No background subtraction was used. All data were taken with the same camera settings and the intensities are normalized to the incident beam current. Overall, there is a clear correlation between the experimental data and un-optimized calculation, and

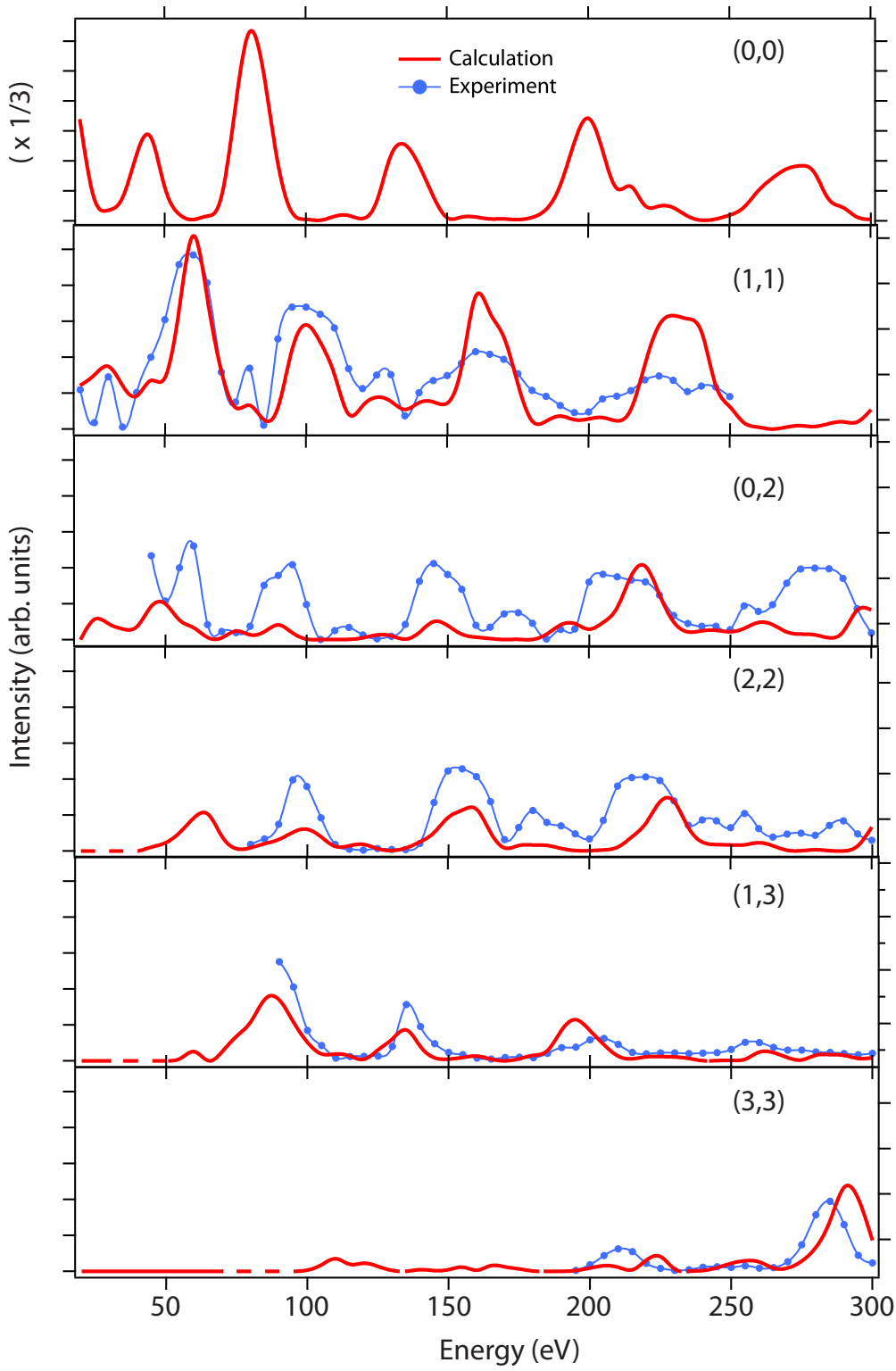

Figure A.6: I-V curves for EuO (001). Red curves are calculated for film coherently strained onto $YAlO_3$ (110) using the parameters V_{0r} = 12 eV and V_{0i} = −5 eV. The blue points are experimentally determined peak intensities measured for a 30 nm $Eu_{0.96}Lu_{0.04}O$ thin film grown on a $YAlO_3$.

the degree of correlation will increase with the implementation of the structural search component of the SATLEED program (not reported here).

In order to evaluate the goodness of fit in the search algorithm, a reliability factor must be defined. A commonly used factor is the Pendry factor, R_P [262]. Pendry formulated his reliability factor based on the desire to give equal weight to all peaks (and minima) in the I-V spectra, regardless of peak intensity. Thus rather than comparing the intensities, $I(E)$, he chose to compare the logarithmic derivatives of the intensities: $L = I'/I$. To avoid the divergence which occurs when I goes to zero, Pendry chose to compare the function

$$Y = \frac{L^{-1}}{L^{-2} + V_{0i}^2} \tag{A.12}$$

calculated using the experimental and theoretical data. The reliability factor is defined as

$$R_P = \frac{\int (Y_{th} - Y_{expt})^2 dE}{\int (Y_{th}^2 + Y_{expt}^2) dE}. \tag{A.13}$$

A value of $R_P = 0$ is achieved for perfect correlation between theoretical and experimental curves. For no correlation, $R_P = 1$. It is generally accepted that a value of $R_P < 0.3$ indicates that the surface structure has been solved. Despite the excellent visual agreement between our measured and calculated I-V curves, the values of R_P are still large (average $R_P = 0.86$). R_P is known to decrease sharply in the viscinity of its minimal value [262]. We therefore expect significant improvement withwith optimization of model parameters such as the inner potential and lattice parameters.

References

1. G. E. Moore, "Cramming more components onto integrated circuits," *Electronics* **38** (1965) 8. 1
2. T. Theis *et al.*, "It's time to reinvent the transistor!," *Science* **327** (2010) 1600. 1
3. R. Ramesh *et al.*, "Whither oxide electronics?," *MRS Bull.* **33** (2008) 1006. 1
4. Y. Tokura *et al.*, "Condensed-matter physics: Complex oxides on fire," *Nat. Mater.* **7** (2008) 694. 1
5. H. Takagi *et al.*, "An emergent change of phase for electronics," *Science* **327** (2010) 1601. 1
6. M. Bohr and K. Mistry, "Intel technology roadmap," 2011. `http://download.intel.com/newsroom/kits/22nm/pdfs/22nm-details_presentation.pdf`. 1
7. `http://energy.gov/sites/prod/files/oeprod/DocumentsandMedia/LIPA__5_16_08.pdf`. 2
8. "FRAM technology overview." `http://www.ti.com/lsds/ti/microcontroller/16-bit_msp430/fram/overview.page?DCMP=FRAM&HQS=FRAM`. 2
9. A. Tsukazaki *et al.*, "Observation of the fractional quantum Hall effect in an oxide," *Nat. Mater.* **9** (2010) 889. 2
10. R. McKee *et al.*, "Crystalline oxides on silicon: the first five monolayers," *Phys. Rev. Lett.* **81** (1998) 3014. 2
11. A. Melville *et al.*, "Lutetium-doped EuO films grown by molecular-beam epitaxy," *Appl. Phys. Lett.* **100** (2012) 222101. 2, 35, 40, 48, 52, 58
12. G. Petrich *et al.*, "Exchange-induced autoionization in Eu-rich EuO," *Phys. Rev. Lett.* **26** (1971) 885. 2, 34, 87
13. T. Penney *et al.*, "Insulator-Metal Transition and Long-Range Magnetic Order in EuO," *Phys. Rev. B* **5** (1972) 3669. 2, 39
14. Y. Shapira *et al.*, "EuO. I. Resistivity and Hall Effect in Fields up to 150 kOe," *Phys. Rev. B* **8** (1973) 2299. 2, 40, 86, 87
15. A. Schmehl *et al.*, "Epitaxial integration of the highly spin-polarized ferromagnetic semiconductor EuO with silicon and GaN," *Nat. Mater.* **6** (2007) 882. 2, 34, 40
16. A. Swartz *et al.*, "Epitaxial EuO thin films on GaAs," *Appl. Phys. Lett.* **97** (2010) 112509. 2, 34
17. T. Santos *et al.*, "Observation of spin filtering with a ferromagnetic EuO tunnel barrier," *Phys. Rev. B* **69** (2004) 241203. 2, 40, 48
18. G. Koster *et al.*, "Structure, physical properties, and applications of $SrRuO_3$ thin films," *Rev. Mod. Phys.* **84** (2012) 253. 2, 112
19. M. Verissimo-Alves *et al.*, "Highly Confined Spin-Polarized Two-Dimensional Electron Gas in $SrTiO_3$/$SrRuO_3$ Superlattices," *Phys. Rev. Lett.* **108** (2012) 107003. 3, 112, 134

20. M. Feigenson *et al.*, "Current-induced magnetic instability in $SrRuO_3$," *J. Appl. Phys.* **103** (2008) 07E741. 3

21. Y. Shperber *et al.*, "Current-induced magnetization reversal in $SrRuO_3$," *Phys. Rev. B* **86** (2012) 085102. 3

22. E. Dagotto, "Complexity in strongly correlated electronic systems," *Science* **309** (2005) 257. 3

23. D. Schlom *et al.*, "A thin film approach to engineering functionality into oxides," *J. Am. Ceram. Soc.* **91** (2008) 2429. 3, 44, 45

24. J. Chakhalian *et al.*, "Whither the oxide interface," *Nat. Mater.* **11** (2012) 92. 3

25. H. Hwang *et al.*, "Emergent phenomena at oxide interfaces," *Nat. Mater.* **11** (2012) 103. 4

26. P. Zubko *et al.*, "Interface Physics in Complex Oxide Heterostructures," *Annu. Rev. Condens. Matter Phys.* **2** (2011) 141. 4

27. S. Hüfner, *Photoelectron Spectroscopy*. Springer-Verlag, Berlin, 1995. 6, 15, 57

28. S. Hüfner, ed., *Very High Resolution Photoelectron Spectroscopy*, vol. 715 of *Lecture Notes in Physics*. Springer, Berlin, 2007. 6

29. H. Bonzel, "On the history of photoemission," *Prog. Surf. Sci.* **49** (1995) 107. 6

30. H. Hertz, "Über einen einfluss des ultravioletten lichtes auf die elektrische entladung," *Ann. Physik* **31** (1887) 983. 7

31. P. Lenard, "Erzeugung von Kathodenstrahlen durch ultraviolettes Licht," *Ann. Physik* **307** (1900) 358. 7

32. P. Lenard, "Ueber die lichtelektrische Wirkung," *Ann. Physik* **313** (1902) 149. 7

33. A. Einstein, "Über einen die erzeugung und verwandlung des lichtes betreffenden heuristischen gesichtspunkt," *Ann. Physik* **322** (1905) 132. 7

34. R. Millikan, "A Direct Photoelectric Determination of Planck's "h"," *Phys. Rev.* **7** (1916) 355. 7

35. W. Spicer *et al.*, "*d* Band of Copper," *Phys. Rev. Lett.* **12** (1964) 9. 7

36. C. Berglund *et al.*, "Photoemission studies of copper and silver: Theory," *Phys. Rev.* **136** (1964) A1030.

37. C. Berglund *et al.*, "Photoemission studies of copper and silver: Experiment," *Phys. Rev.* **136** (1964) A1044. 7

38. E. Kane, "Implications of crystal momentum conservation in photoelectric emission for band-structure measurements," *Phys. Rev. Lett.* **12** (1964) 97. 8

39. M. Traum *et al.*, "Angular Dependence of Photoemission and Atomic Orbitals in the Layer Compound 1*T*-$TaSe_2$," *Phys. Rev. Lett.* **32** (1974) 1241. 8

40. N. Smith *et al.*, "Mapping energy bands in layer compounds from the angular dependence of ultraviolet photoemission," *Solid State Commun.* **15** (1974) 211. 8

41. A. Damascelli, "Probing the electronic structure of complex systems by ARPES," *Phys. Scripta* **T109** (2004) 61. 10, 65

42. M. Seah *et al.*, "Quantitative Electron Spectroscopy of Spectroscopy of Surfaces," *Surf. Interface Anal.* **1** (1979) 2. 13, 14, 135

43. V. Strocov, "Intrinsic accuracy in 3-dimensional photoemission band mapping," *J. Electron Spectrosc.* **130** (2003) 65. 13, 15

44. A. Damascelli *et al.*, "Angle-resolved photoemission studies of the cuprate superconductors," *Rev. Mod. Phys.* **75** (2003) 473. 16, 29

45. R. Mattuck, *A Guide to Feynman Diagrams in the Many-Body Problem (Dover Books on Physics)*. Dover Publications, New York, 1992. 17

46. A. A. Kordyuk *et al.*, "Bare electron dispersion from experiment: Self-consistent self-energy analysis of photoemission data," *Phys. Rev. B* **71** (2005) 214513. 20

47. G. Grimvall, *The Electron-Phonon Interaction in Metals*. North-Holland Publishing Company, Amsterdam, 1981. 20

48. J. Harter *et al.*, "A tunable low-energy photon source for high-resolution angle-resolved photoemission spectroscopy," *Rev. Sci. Instrum.* **83** (2012) 113103. 23

49. D. Roy *et al.*, "Design of electron spectrometers," *Rep. Prog. Phys.* **53** (1990) 1621. 23, 24

50. N. Smith *et al.*, "General instrumentation considerations in electron and ion spectroscopies using synchrotron radiation," *Nucl. Instrum. Methods* **195** (1982) 309. 23

51. B. Wannberg, "Electron optics development for photo-electron spectrometers," *Nucl. Instrum. Meth. A* **601** (2009) 182. 26

52. J. Harter, *Angle-Resolved Photoemission Spectroscopy of $Sr_{1-x}La_xCuO_2$ thin films grown by molecular-beam epitaxy*. PhD thesis, Cornell University, 2013. 27

53. E. Monkman *et al.*, "Quantum many-body interactions in digital oxide superlattices," *Nat. Mater.* **11** (2012) 855. 29

54. J. Harter *et al.*, "Nodeless Superconducting Phase Arising from a Strong (π,π) Antiferromagnetic Phase in the Infinite-Layer Electron-Doped $Sr_{1-x}La_xCuO_2$ Compound," *Phys. Rev. Lett.* **109** (2012) 267001. 29

55. E. Monkman *et al.*, "Epitaxial strain control of electronic structure through the metal-insulator transition in manganite thin films," *submitted* (2014) . 29

56. P. D. C. King *et al.*, "Atomic-scale control of competing electronic phases in ultrathin $LaNiO_3$," *Nature Nanotech.* (2014) . 29

57. H. International, "Haynes® 214® alloy information." `http://www.haynesintl.com/214HAYNESALLOY.htm`. 30

58. J. Rondinelli *et al.*, "Oxide interfaces: Instrumental insights," *Nat. Mater.* **11** (2012) 833. 31

59. P. Wachter, "Europium Chalcogenides: EuO, EuS, EuSe and EuTe," *Handbook on the Physics and Chemistry of Rare Earths* **2** (1979) 507–574. 33

60. A. Mauger *et al.*, "The magnetic, optical, and transport properties of representatives of a class of magnetic semiconductors: The europium chalcogenides," *Phys. Rep.* **141** (1986) 51.

61. E. Nagaev, "Colossal-magnetoresistance materials: manganites and conventional ferromagnetic semiconductors," *Phys. Rep.* **346** (2001) 387.

62. T. Kasuya *et al.*, "Anomalous Transport Phenomena in Eu-Chalcogenide Alloys," *Rev. Mod. Phys.* **40** (1968) 684.

63. W. Nolting, "Theory of ferromagnetic semiconductors," *Phys. Status Solidi (B)* **96** (1979) 11.

64. N. Tsuda, K. Nasu, A. Yanase, and K. Siratori, *Electronic Conduction in Oxides*, vol. 94 of *Springer Series in Solid- State Sciences*. Springer Verlag, Berlin, 1991.

65. P. Wachter, "The optical electrical and magnetic properties of the europium chalcogenides and the rare earth pnictides," *Crit. Rev. Solid State Mater. Sci.* **3** (1972) 189. 33

66. G. Brauer, "Über Europium(II)-Oxyd," *Angew. Chem.* **65** (1953) 261. 33

67. H. Eick *et al.*, "Lower Oxides of Samarium and Europium. The Preparation and Crystal Structure of $SmO_{0.4-0.6}$, SmO and EuO," *J. Am Chem. Soc.* **78** (1956) 5147. 33

68. B. Matthias *et al.*, "Ferromagnetic Interaction in EuO," *Phys. Rev. Lett.* **7** (1961) 160. 33, 36

69. I. Tsubokawa, "On the Magnetic Properties of a $CrBr_3$ Single Crystal," *J. Phys. Soc. Jpn* **15** (1960) 1664. 33

70. H. Yang *et al.*, "Proximity Effects Induced in Graphene by Magnetic Insulators: First-Principles Calculations on Spin Filtering and Exchange-Splitting Gaps," *Phys. Rev. Lett.* **110** (2013) 046603. 34

71. A. Swartz *et al.*, "Integration of the Ferromagnetic Insulator EuO onto Graphene," *ACS Nano* **6** (2012) 10069. 34

72. M. Oliver *et al.*, "Temperature and magnetic field dependence of the conductivity of EuO," *IBM J. Res. Dev.* **14** (1970) 276. 34, 40

73. M. Oliver *et al.*, "Pressure dependence of the electrical resistivity of EuO," *Phys. Rev. Lett.* **24** (1970) 1064. 34, 39

74. K.-H. Hellwege and O. Madelung, eds., *Landolt-Börnstein: Numerical Data and Functional Relationships in Science and Technology 321*, vol. 17 of *New Series – Group III*. Springer, Berlin, 1984. 35, 93, 110

75. F. Lévy, "Effets magnétostrictifs spontanés de quelques composés des terres rares," *Physik Kondens. Materie* **10** (1969) 71. 35

76. M. Shafer *et al.*, "Studies of Curie-Point Increases in EuO," *J. Appl. Phys.* **39** (1968) 588. 35, 37

77. K. Ahn *et al.*, "Magnetic and Magneto-optic Properties of EuO Films Doped with Trivalent Rare-Earth Oxide," *J. Appl. Phys.* **39** (2003) 5061.

78. T. Mairoser *et al.*, "Influence of chemical doping on the magnetic properties of EuO," *Phys. Rev. B* **87** (2013) 014416. 35, 37, 48

79. K. Y. Ahn, "EuO Films Doped with Fe and Gd," *J. Appl. Phys.* **43** (1972) 231. 35

80. S. Kikuda *et al.*, "Magnetic Properties of EuO Thin Films Doped with Transition Metal," *IEEE Transl. J. Magn. Jpn.* **2** (1987) 434.

81. K. Y. Ahn, "Increase of Curie Temperature in EuO Films by Fe Doping," *Appl. Phys. Lett.* **17** (1970) 347.

82. T. McGuire *et al.*, "Magnetic and Magneto-Optical Properties of Fe-Doped EuO Films," *J. Appl. Phys.* **42** (1971) 1775. 35, 37

83. E. Bousquet *et al.*, "Strain-Induced Ferroelectricity in Simple Rocksalt Binary Oxides," *Phys. Rev. Lett.* **104** (2010) 37601. 35, 67

84. T. Kasuya, "Exchange mechanisms in europium chalcogenides," *IBM J. Res. Dev.* **14** (1970) 214. 36

85. H. Miyazaki *et al.*, "Direct Observation of Momentum-Dependent Exchange Interaction in a Heisenberg Ferromagnet," *Phys. Rev. Lett.* **102** (2009) 227203. 36, 63, 65

86. R. W. Ulbricht *et al.*, "Adsorption-controlled growth of EuO by molecular-beam epitaxy," *Appl. Phys. Lett.* **93** (2008) 2105. 37, 48, 61

87. H. Miyazaki *et al.*, "La-doped EuO: A rare earth ferromagnetic semiconductor with the highest Curie temperature," *Appl. Phys. Lett.* **96** (2010) 232503. 37, 38

88. A. Mauger *et al.*, "Magnetic properties of Gd doped EuO single crystals," *Le Journal de Physique Colloques* **41** (1980) C5–263. 37

89. H. Ott *et al.*, "Soft x-ray magnetic circular dichroism study on Gd-doped EuO thin films," *Phys. Rev. B* **73** (2006) 94407. 48

90. R. Sutarto *et al.*, "Epitaxy, stoichiometry, and magnetic properties of Gd-doped EuO films on YSZ (001)," *Phys. Rev. B* **80** (2009) 85308. 38, 52, 61

91. T. Mairoser *et al.*, "Is There an Intrinsic Limit to the Charge-Carrier-Induced Increase of the Curie Temperature of EuO?," *Phys. Rev. Lett.* **105** (2010) 257206. 37, 38, 48, 52, 69, 74, 78, 85, 87, 88, 110

92. S. Altendorf *et al.*, "Oxygen off-stoichiometry and phase separation in EuO thin films," *Phys. Rev. B* **84** (2011) 155442. 38, 48

93. X. Wang *et al.*, "Effects of Gd Doping and Oxygen Vacancies on the Properties of EuO Films Prepared via Pulsed Laser Deposition," *IEEE Trans. Magn.* **46** (2010) 1879. 38, 80

94. P. Liu *et al.*, "Antiferromagnetic coupling in EuO_{1-x}," *Phys. Rev. B* **85** (2012) 224417. 38

95. P. Monteiro *et al.*, "Spatially homogeneous ferromagnetism below the enhanced Curie temperature in EuO_{1-x} thin films," *Phys. Rev. Lett.* **110** (2013) 217208. 38, 94

96. S. V. Molnár, "Transport properties of the europium chalcogenides," *IBM J. Res. Dev.* **14** (1970) 269. 40

97. P. G. Steeneken *et al.*, "Exchange Splitting and Charge Carrier Spin Polarization in EuO," *Phys. Rev. Lett.* **88** (2002) 047201. 40

98. J. Moodera *et al.*, "The phenomena of spin-filter tunnelling," *J. Phys.: Condens. Matter* **19** (2007) 165202. 40

99. J. Lettieri *et al.*, "Epitaxial growth and magnetic properties of EuO on (001) Si by molecular-beam epitaxy," *Appl. Phys. Lett.* **83** (2003) 975. 40, 48

100. J. A. Mundy *et al.*, "Hetero-epitaxial EuO Interfaces Studied by Analytic Electron Microscopy," *arXiv* **cond-mat.mtrl-sci** (2013) , 1308.0967v1. 40

101. Y. Shapira *et al.*, "EuO. II. Dependence of the Insulator-Metal Transition on Magnetic Order," *Phys. Rev. B* **8** (1973) 2316. 40

102. M. Abd-Elmeguid *et al.*, "Onset of valence and magnetic instabilities in the ferromagnetic semiconductor EuO at high pressures," *Phys. Rev. B* **42** (1990) 1048. 41

103. H. Zimmer *et al.*, "Insulator-metal transition and valence instability in EuO near 130 kbar," *Phys. Rev. B* **29** (1984) 2350. 41

104. D. DiMarzio *et al.*, "Effect of pressure on the electrical resistance of EuO," *Phys. Rev. B* **35** (1987) 8891. 41

105. N. J. C. Ingle *et al.*, "Influence of epitaxial strain on the ferromagnetic semiconductor EuO : First-principles calculations," *Phys. Rev. B* **77** (2008) 121202. 41, 65, 67, 79

106. R. Sutarto, *EuO and Gd-doped EuO thin films: epitaxial growth and properties*. PhD thesis, Universität zu Köln, 2009. 41

107. T. Etsell *et al.*, "Electrical properties of solid oxide electrolytes," *Chem. Rev.* **70** (1970) 339. 41

108. R. Sutarto *et al.*, "Epitaxial and layer-by-layer growth of EuO thin films on yttria-stabilized cubic zirconia (001) using MBE distillation," *Phys. Rev. B* **79** (2009) 205318. 41, 48

109. A. Melville *et al.*, "Effect of film thickness and biaxial strain on the curie temperature of EuO," *Appl. Phys. Lett.* **102** (2013) 062404. 42, 79

110. A. Melville *et al.*, "Epitaxial growth of europium monoxide on diamond," *Appl. Phys. Lett.* **103** (2013) 222402. 42

111. Y. Wang *et al.*, "Prediction of a spin-polarized two-dimensional electron gas at the $LaAlO_3$/EuO (001) interface," *Phys. Rev. B* **79** (2009) 212408. 42, 67

112. H. Zhang *et al.*, "Topological States in Ferromagnetic CdO/EuO Superlattices and Quantum Wells," *Phys. Rev. Lett.* **112** (2014) 096804. 42

113. P. Wei *et al.*, "Exchange-Coupling-Induced Symmetry Breaking in Topological Insulators," *Phys. Rev. Lett.* **110** (2013) 186807. 42

114. A. Cho *et al.*, "Molecular Beam Epitaxy," *Prog. Solid State Ch.* **10** (1975) 157. 44

115. R. Betts *et al.*, "Growth of thin-film lithium niobate by molecular beam epitaxy," *Electron. Lett.* **21** (1985) 960. 45

116. J. Haeni *et al.*, "RHEED intensity oscillations for the stoichiometric growth of $SrTiO_3$ thin films by reactive molecular beam epitaxy," *J. Electroceram.* **4** (2000) 385. 46

117. C. Adamo *et al.*, "*In situ* composition control of oxide thin films using shuttered RHEED intensity oscillations," *submitted* (2014) . 46

118. M. Shafer *et al.*, "Relationship of crystal growth parameters to the stoichiometry of EuO as determined by I.R. and conductivity measurements," *J. Phys. Chem. Solids* **33** (1972) 2251. 47

119. J. Arthur, "Interaction of Ga and As_2 molecular beams with GaAs surfaces," *J. Appl. Phys.* **39** (1968) 4032. 47

120. P. Steeneken, *New light on EuO thin films*. PhD thesis, Rijksuniversiteit Groningen, 2002. 48

121. G. J. McCarthy, "Oxygen-Fugacity-Temperature Diagram for the Eu-O System," *J. Am. Ceram. Soc.* **57** (1974) 502. 48

122. A. Melville *et al.*, "Protective amorphous Eu_2O_3 barrier for EuO thin films," *submitted* (2013) . 48

123. W.-D. Schneider *et al.*, "Shake-up excitations and core-hole screening in Eu systems," *Phys. Rev. B* **24** (1981) 5422. 49

124. D. Shai *et al.*, "Temperature Dependence of the Electronic Structure and Fermi-Surface Reconstruction of $Eu_{1-x}Gd_xO$ through the Ferromagnetic Metal-Insulator Transition," *Phys. Rev. Lett.* **108** (2012) 267003. 51, 53, 59

125. A. Achkar *et al.*, "Bulk sensitive x-ray absorption spectroscopy free of self-absorption effects," *Phys. Rev. B* **83** (2011) 081106. 53

126. A. Achkar *et al.*, "Determination of total x-ray absorption coefficient using non-resonant x-ray emission," *Sci. Rep.* **1** (2011) 182. 53

127. S. Eisebitt *et al.*, "Determination of absorption coefficients for concentrated samples by fluorescence detection," *Phys. Rev. B* **47** (1993) 14103. 55

128. E. Negusse *et al.*, "Effect of electrode and EuO thickness on EuO-electrode interface in tunneling spin filter," *J. Appl. Phys.* **99** (2006) 08E507. 57

129. W. Lang *et al.*, "Multiplet structure in X-ray photoelectron spectra of rare earth elements and their surface oxides," *Faraday Discuss. Chem. Soc.* **60** (1975) 37. 57

130. D. E. Eastman *et al.*, "Photoemission Studies of the Electronic Structure of EuO, EuS, EuSe, And GdS," *Phys. Rev. Lett.* **23** (1969) 226. 63

131. R. Schiller *et al.*, "Prediction of a surface state and a related surface insulator-metal transition for the (100) surface of stochiometric EuO," *Phys. Rev. Lett.* **86** (2001) 3847. 63

132. J. Schoenes *et al.*, "Exchange optics in Gd-doped EuO," *Phys. Rev. B* **9** (1974) 3097. 64, 75, 77, 93, 94

133. R. Schiller *et al.*, "Temperature-dependent band structure of bulk EuO," *Solid State Commun.* **118** (2001) 173. 67

134. T. Mairoser, "Untersuchung des Dotierverhaltens epitaktischer EuO-Filme," Diploma Thesis, Universität Augsburg, 2009. 69

135. T. Matsumoto *et al.*, "Preparation of Gd-doped EuO_{1-x} thin films and the magnetic and magneto-transport properties," *J. Phys.: Condens. Matter* **16** (2004) 6017. 69

136. B. Sheu *et al.*, "Onset of ferromagnetism in low-doped $Ga_{1-x}Mn_xAs$," *Phys. Rev. Lett.* **99**

(2007) 227205. 69

137. K. Shen *et al.*, "Missing quasiparticles and the chemical potential puzzle in the doping evolution of the cuprate superconductors," *Phys. Rev. Lett.* **93** (2004) 267002. 69

138. D. Schrupp *et al.*, "High-energy photoemission on Fe_3O_4: Small polaron physics and the Verwey transition," *Europhys. Letters* **70** (2005) 789. 69

139. N. Mannella *et al.*, "Nodal quasiparticle in pseudogapped colossal magnetoresistive manganites," *Nature* **438** (2005) 474. 69, 71

140. Y.-D. Chuang *et al.*, "Fermi surface nesting and nanoscale fluctuating charge/orbital ordering in colossal magnetoresistive oxides," *Science* **292** (2001) 1509. 69, 71

141. B. Shklovskii and A. Efros, *Electronic Properties of Doped Semiconductors*. Springer-Verlag, Berlin, 1984. 71

142. J. Yeh *et al.*, "Atomic subshell photoionization cross sections and asymmetry parameters: $1 \leq Z \leq 103$," *At. Data. Nucl. Data Tables* **32** (1985) 1. 76

143. R. Shannon, "Revised effective ionic radii and systematic studies of interatomic distances in halides and chalcogenides," *Acta Crystallogr. Sect. A* **32** (1976) 751. 78, 139

144. S. Altendorf *et al.*, "Spectroscopic observation of strain-assisted T_C enhancement in EuO upon Gd doping," *Phys. Rev. B* **85** (2012) 081201. 80

145. S. Altendorf *et al.*, "Growth and characterization of Sc-doped EuO thin films," *Appl. Phys. Lett.* **104** (2014) 052403. 80

146. G. Brauer *et al.*, "Die mischkristallreihe EuO-SrO und ein neues verfahren zur darstellung von EuO," *J. Less Common Met.* **13** (1967) 213. 80

147. K. Ahn *et al.*, "Preparation and properties of EuO films," *IEEE Trans. Magn.* **3** (1967) 453. 80

148. F. Liu *et al.*, "Ultrafast Time-Resolved Faraday Rotation in EuO Thin Films," *Phys. Rev. Lett.* **108** (2012) 257401. 80

149. R. Ingel *et al.*, "Lattice Parameters and Density for Y_2O_3-Stabilized ZrO_2," *J. Am. Ceram. Soc.* **69** (1986) 325. 81

150. P. Dernier *et al.*, "High pressure synthesis and crystal data of the rare earth orthoaluminates," *Mater. Res. Bull.* **6** (1971) 433. 81

151. S. Geller *et al.*, "Crystallographic studies of perovskite-like compounds. I. Rare earth orthoferrites and $YFeO_3$, $YCrO_3$, $YAlO_3$," *Acta Cryst.* **9** (1956) 563. 81

152. J. Luttinger *et al.*, "Ground-state energy of a many-fermion system. II," *Phys. Rev.* **118** (1960) 1417. 84, 104

153. J. Luttinger, "Fermi surface and some simple equilibrium properties of a system of interacting fermions," *Phys. Rev.* **119** (1960) 1153. 84, 104

154. N. Mott, "Metal-Insulator Transition," *Rev. Mod. Phys.* **40** (1968) 677. 85

155. M. Alexander *et al.*, "Semiconductor-to-metal transition in n-type group IV semiconductors," *Rev. Mod. Phys.* **40** (1968) 815. 86

156. P. Edwards *et al.*, "Universality aspects of the metal-nonmetal transition in condensed media," *Phys. Rev. B* **17** (1978) 2575. 86

157. N. Ashcroft and N. Mermin, *Solid State Physics*. Saunders College, Philadelphia, 1976. 86

158. M. Oliver *et al.*, "Conductivity Studies in Europium Oxide," *Phys. Rev. B* **5** (1972) 1078. 87

159. C. Godart *et al.*, "Physical Properties of EuO Versus Electronic Concentrations," *J. Phys. Colloques* **41** (1980) C5–205. 87

160. W. Ku *et al.*, "Unfolding first-principles band structures," *Phys. Rev. Lett.* **104** (2010) 216401. 88

161. V. Popescu *et al.*, "Effective band structure of random alloys," *Phys. Rev. Lett.* **104** (2010) 236403. 88

162. T. Herng *et al.*, "Room-temperature ferromagnetism of Cu-doped ZnO films probed by soft X-ray magnetic circular dichroism," *Phys. Rev. Lett.* **105** (2010) 207201. 88

163. T. Berlijn *et al.*, "Do transition-metal substitutions dope carriers in iron-based superconductors?," *Phys. Rev. Lett.* **108** (2012) 207003. 88

164. K. Iwaya *et al.*, "Atomically resolved silicon donor states of β-Ga_2O_3," *Appl. Phys. Lett.* **98** (2011) 142116–142116–3. 88

165. P. Richard *et al.*, "Observation of momentum space semi-localization in Si-doped β-Ga_2O_3," *Appl. Phys. Lett.* **101** (2012) 232105. 88

166. M. Fischer. private communication. 90

167. J. Klinkhammer *et al.*, "Spin-Polarized Surface State in EuO (100)," *Phys. Rev. Lett.* **112** (2014) 016803. 92

168. N. Bebenin, "On magnetic red shift of absorption edge in EuO," *Solid State Commun.* **55** (1985) 823. 93

169. C. Patil *et al.*, "Magnetic Field Dependent Carrier Mobility in Ferromagnetic Semiconductors," *Phys. Status Solidi (B)* **105** (1981) 391. 93

170. J. Torrance *et al.*, "Bound Magnetic Polarons and the Insulator-Metal Transition in EuO," *Phys. Rev. Lett.* **29** (1972) 1168. 93

171. A. Mauger, "Magnetic polaron: Theory and experiment," *Phys. Rev. B* **27** (1983) 2308. 93

172. W. Spicer, "Negative affinity 3–5 photocathodes: Their physics and technology," *Appl. Phys.* **12** (1977) 115. 97

173. W. Mross, "Alkali doping in heterogeneous catalysis," *Catal. Rev.-Sci. Eng.* **25** (1983) 591. 97

174. I. Langmuir, "Vapor pressures, evaporation, condensation and adsorption," *J. Am Chem. Soc.* **54** (1932) 2798. 97

175. R. Gurney, "Theory of electrical double layers in adsorbed films," *Phys. Rev.* **47** (1935) 479. 97

176. R. Diehl *et al.*, "Current progress in understanding alkali metal adsorption on metal

surfaces," *J. Phys.: Condens. Matter* **9** (1997) 951. 97

177. M. Hossain *et al.*, "In situ doping control of the surface of high-temperature superconductors," *Nature Phys.* **4** (2008) 527. 98

178. P. King *et al.*, "Large Tunable Rashba Spin Splitting of a Two-Dimensional Electron Gas in Bi_2Se_3," *Phys. Rev. Lett.* **107** (2011) 096802. 98

179. R. Comin *et al.*, "Na_2IrO_3 as a Novel Relativistic Mott Insulator with a 340-meV Gap," *Phys. Rev. Lett.* **109** (2012) 266406. 98

180. K. Rossnagel *et al.*, "Continuous Tuning of Electronic Correlations by Alkali Adsorption on Layered 1*T*-TaS_2," *Phys. Rev. Lett.* **95** (2005) 126403. 98

181. L. Bondarenko *et al.*, "Large spin splitting of metallic surface-state bands at adsorbate-modified gold/silicon surfaces," *Sci. Rep.* **3** (2013) 1826. 98

182. T. Eknapakul *et al.*, "Electronic structure of a quasi-freestanding MoS_2 monolayer," *Nano Letters* no. 14, (2014) 1312. 98

183. Y. Zhang *et al.*, "Direct observation of the transition from indirect to direct bandgap in atomically thin epitaxial $MoSe_2$," *Nature Nanotech.* **9** (2013) 111. 98

184. S. Zhou *et al.*, "Metal to insulator transition in epitaxial graphene induced by molecular doping," *Phys. Rev. Lett.* **101** (2008) 086402. 98

185. M. Succi *et al.*, "Atomic absorption evaporation flow rate measurements of alkali metal dispensers," *Vacuum* **35** (1985) 579. 98

186. G. Ebbinghaus *et al.*, "Photoemission from Metallic Cesium Oxide Films," *Phys. Rev. Lett.* **37** (1976) 1770. 99

187. T. Sham *et al.*, "Electronic structure of Cs multilayer and monolayer adsorbed on Ru (001): A photoemission study," *J. Chem. Phys.* **89** (1988) 1188. 99

188. S. Mahanti *et al.*, "Band Structure and Properties of Cesium Metal," *Phys. Rev.* **183** (1969) 674. 103

189. K. Okumura *et al.*, "The Fermi surface of caesium," *Proc. R. Soc. A* **287** (1965) 89. 104

190. A. Naumovets *et al.*, "Surface diffusion of adsorbates," *Surf. Sci. Rep.* **4** (1985) 365. 104

191. H. Over *et al.*, "Coverage dependence of adsorption-site geometry in the Cs/Ru(0001) system: A low-energy electron-diffraction analysis," *Phys. Rev. B* **45** (1992) 8638. 104

192. L. Pauling, "Atomic radii and interatomic distances in metals," *J. Am Chem. Soc.* **69** (1947) 542. 107

193. H. Ishida *et al.*, "First-principles study of the coverage dependence of the electronic structure of alkali-metal-metal surfaces: Na on Al (001)," *Phys. Rev. B* **38** (1988) 5752. 108

194. M. Scheffler *et al.*, "A self-consistent surface-Green-function (SSGF) method," *Physica B: Condensed Matter* **172** (1991) 143. 108

195. D. Riffe *et al.*, "Alkali metal adsorbates on W (110): Ionic, covalent, or metallic?," *Phys. Rev. Lett.* **64** (1990) 571. 109

196. G. Wertheim *et al.*, "Nature of the charge localized between alkali adatoms and metal

substrates," *Phys. Rev. B* **49** (1994) 4834. 109

197. A. Andrews *et al.*, "Surface Core-Level Shifts of Ta (110) and W (110) vs. Alkali-Atom Coverage: Implications for theAlkali-Substrate Interaction," *Phys. Rev. B* **49** (1994) 8396. 109

198. G. Benesh *et al.*, "Core-level shift spectroscopy for adsorbates: ionic, covalent or metallic bonding?," *Chemical physics letters* **191** (1992) 315. 109, 110

199. D. Balz *et al.*, "Die Struktur des Kaliumnickelfluorids, K_2NiF_4," *Z. Elektrochem.* **59** (1955) 545. 111

200. S. Ruddlesden *et al.*, "The compound $Sr_3Ti_2O_7$ and its structure," *Acta Cryst.* **11** (1958) 54. 111

201. A. Mackenzie *et al.*, "The superconductivity of Sr_2RuO_4 and the physics of spin-triplet pairing," *Rev. Mod. Phys.* **75** (2003) 657. 112

202. S. Grigera *et al.*, "Magnetic field-tuned quantum criticality in the metallic ruthenate $Sr_3Ru_2O_7$," *Science* **294** (2001) 329. 112

203. A. Callaghan *et al.*, "Magnetic interactions in ternary ruthenium oxides," *Inorg. Chem.* **5** (1966) 1572. 112

204. J. Longo *et al.*, "Magnetic properties of $SrRuO_3$ and $CaRuO_3$," *J. Appl. Phys.* **39** (2003) 1327. 112

205. J. Junquera *et al.*, "Critical thickness for ferroelectricity in perovskite ultrathin films," *Nature* **422** (2003) 506. 112

206. T. Fuji *et al.*, "Hysteretic current-voltage characteristics and resistance switching at an epitaxial oxide Schottky junction $SrRuO_3/SrTi_{0.99}$ $Nb_{0.01}O_3$," *Appl. Phys. Lett* **86** (2005) 012107.

207. S. Thota *et al.*, "Anisotropic magnetocaloric effect in all-ferromagnetic ($La_{0.7}Sr_{0.3}MnO_3/SrRuO_3$) superlattices," *Appl. Phys. Lett.* **97** (2010) 112506.

208. M. Niranjan *et al.*, "Magnetoelectric effect at the $SrRuO_3/BaTiO_3$ (001) interface: An ab initio study," *Appl. Phys. Lett.* **95** (2009) 052501. 112

209. Z. Fang *et al.*, "The anomalous Hall effect and magnetic monopoles in momentum space," *Science* **302** (2003) 92. 112

210. P. Allen *et al.*, "Transport properties, thermodynamic properties, and electronic structure of $SrRuO_3$," *Phys. Rev. B* **53** (1996) 4393. 113, 126

211. J. S. Ahn *et al.*, "Spectral Evolution in (Ca,Sr)RuO_3 near the Mott-Hubbard Transition," *Phys. Rev. Lett.* **82** (1999) 5321. 113, 126

212. M. Imada *et al.*, "Metal-insulator transitions," *Rev. Mod. Phys.* **70** (1998) 1039. 113

213. J. Lee *et al.*, "Optical investigation of the electronic structures of $Y_2Ru_2O_7$, $CaRuO_3$, $SrRuO_3$, and $Bi_2Ru_2O_7$," *Phys. Rev. B* **64** (2001) 245107. 113, 126

214. K. Fujioka *et al.*, "Electronic structure of $SrRuO_3$," *Phys. Rev. B* **56** (1997) 6380. 113, 119, 126

215. K. Maiti *et al.*, "Evidence against strong correlation in 4*d* transition-metal oxides $CaRuO_3$ and $SrRuO_3$," *Phys. Rev. B* **71** (2005) 161102(R). 113, 126

216. J. S. Dodge *et al.*, "Temperature-dependent local exchange splitting in $SrRuO_3$," *Phys. Rev. B* **60** (1999) 6987. 113, 128

217. J.-G. Cheng *et al.*, "Critical behavior of ferromagnetic perovskite ruthenates," *Phys. Rev. B* **85** (2012) 184430. 113, 130, 134

218. A. Damascelli *et al.*, "Fermi Surface, Surface States, and Surface Reconstruction in Sr_2RuO_4," *Phys. Rev. Lett.* **85** (2000) 5194. 114

219. K. M. Shen *et al.*, "Surface electronic structure of Sr_2RuO_4," *Phys. Rev. B* **64** (2001) 180502.

220. N. Ingle *et al.*, "Quantitative analysis of Sr_2RuO_4 angle-resolved photoemission spectra: Many-body interactions in a model Fermi liquid," *Phys. Rev. B* **72** (2005) 205114.

221. M. W. Haverkort *et al.*, "Strong Spin-Orbit Coupling Effects on the Fermi Surface of Sr_2RuO_4 and Sr_2RhO_4," *Phys. Rev. Lett.* **101** (2008) 26406.

222. C. Veenstra *et al.*, "Determining the Surface-To-Bulk Progression in the Normal-State Electronic Structure of Sr_2RuO_4 by Angle-Resolved Photoemission and Density Functional Theory," *Phys. Rev. Lett.* **110** (2013) 097004. 114

223. Maenoyoshiteru *et al.*, "Two-Dimensional Fermi Liquid Behavior of the Superconductor Sr_2RuO_4," *J. Phys. Soc. Jpn* **66** (1997) 1405. 114

224. A. Tamai *et al.*, "Fermi Surface and van Hove Singularities in the Itinerant Metamagnet $Sr_3Ru_2O_7$," *Phys. Rev. Lett.* **101** (2008) 26407. 114

225. M. Allan *et al.*, "Formation of heavy d-electron quasiparticles in $Sr_3Ru_2O_7$," *New J. Phys.* **15** (2013) 063029. 114

226. L. Capogna *et al.*, "Sensitivity to Disorder of the Metallic State in the Ruthenates," *Phys. Rev. Lett.* **88** (2002) 76602. 118

227. W. Siemons *et al.*, "Dependence of the electronic structure of $SrRuO_3$ and its degree of correlation on cation off-stoichiometry," *Phys. Rev. B* **76** (2007) 075126. 118, 120

228. J. Kim *et al.*, "In situ photoemission study on $SrRuO_3/SrTiO_3$ films grown by pulsed laser deposition," *Phys. Rev. B* **71** (2005) 121406(R). 119

229. D. Kacedon *et al.*, "Magnetoresistance of epitaxial thin films of ferromagnetic metallic oxide $SrRuO_3$ with different domain structures," *Appl. Phys. Lett.* **71** (1997) 1724. 119

230. F. Chu *et al.*, "Microstructures and electrical properties of $SrRuO_3$ thin films on $LaAlO_3$ substrates," *J. Electron. Mater.* **25** (1996) 1754. 119, 120

231. C. Alexander *et al.*, "Angle-resolved de Haas–van Alphen study of $SrRuO_3$," *Phys. Rev. B* **72** (2005) 024415. 120, 122, 125, 126

232. G. Cao *et al.*, "Thermal, magnetic, and transport properties of single-crystal $Sr_{1-x}Ca_xRuO_3$ ($0 \leq x \leq 1.0$)," *Phys. Rev. B* **56** (1997) 321. 120

233. A. Mackenzie *et al.*, "Observation of quantum oscillations in the electrical resistivity of $SrRuO_3$," *Phys. Rev. B* **58** (1998) R13318. 120, 122, 124, 125

234. L. Klein *et al.*, "Extraordinary Hall effect in $SrRuO_3$," *Phys. Rev. B* **61** (2000) 7842. 120

235. M. Schneider *et al.*, "Ferromagnetic quantum phase transition in $Sr_{1-x}Ca_xRuO_3$ thin films," *Phys. Status Solidi (B)* **247** (2010) 577. 120

236. G. Santi *et al.*, "Calculation of the electronic structure and the magnetic properties of $SrRuO_3$ and $CaRuO_3$," *J. Phys.: Condens. Matter* **9** (1997) 9563. 122

237. R. Bracewell, *The Fourier Transform and Its Applications*. McGraw-Hill, New York, 1986. 125

238. C. Etz *et al.*, "Indications of weak electronic correlations in $SrRuO_3$ from first-principles calculations," *Phys. Rev. B* **86** (2012) 064441. 126

239. L. Klein *et al.*, "Transport and magnetization in the badly metallic itinerant ferromagnet," *J. Phys.: Condens. Matter* **8** (1996) 10111. 128, 129

240. E. Stoner, "Collective electron ferromagnetism," *Proc. R. Soc. A* **165** (1938) 372. 128

241. D. Singh, "Electronic and magnetic properties of the 4*d* itinerant ferromagnet $SrRuO_3$," *J. Appl. Phys.* **79** (1996) 4818. 128

242. F. Fukunaga *et al.*, "On the Magnetism and Electronic Conduction of Itinerant Magnetic System $Ca_{1-x}Sr_xRuO_3$," *J. Phys. Soc. Jpn* **63** (1994) 3798. 130

243. B. Sinkovic *et al.*, "Local Electronic and Magnetic Structure of Ni below and above T_c: A Spin-Resolved Circularly Polarized Resonant Photoemission Study," *Phys. Rev. Lett.* **79** (1997) 3510. 130

244. T. J. Kreutz *et al.*, "Temperature-dependent electronic structure of nickel metal," *Phys. Rev. B* **58** (1998) 1300. 130

245. E. Kisker *et al.*, "Temperature Dependence of the Exchange Splitting of Fe by Spin-Resolved Photoemission Spectroscopy with Synchrotron Radiation," *Phys. Rev. Lett.* **52** (1984) 2285. 130

246. K. Baberschke, M. Donath, and W. Nolting, *Band Ferromagnetism*. Springer-Verlag, Berlin, 2001. 130

247. T. Mairoser *et al.*, "Influence of the substrate temperature on the Curie temperature and charge carrier density of epitaxial Gd-doped EuO films," *Appl. Phys. Lett.* **98** (2011) 102110. 132

248. P. H. Citrin *et al.*, "Geometric Frustration of 2D Dopants in Silicon: Surpassing Electrical Saturation," *Phys. Rev. Lett.* **83** (1999) 3234. 132

249. H. Miyazaki *et al.*, "Three-dimensional angle-resolved photoemission spectra of EuO thin film," *J. Electron Spectrosc.* **191** (2013) 7. 133

250. A. Vailionis *et al.*, "Misfit strain accommodation in epitaxial ABO_3 perovskites: Lattice rotations and lattice modulations," *Phys. Rev. B* **83** (2011) 064101. 133

251. W. Lu *et al.*, "Control of oxygen octahedral rotations and physical properties in $SrRuO_3$ films," *Phys. Rev. B* **88** (2013) 214115. 133

252. C.-Q. Jin *et al.*, "High-pressure synthesis of the cubic perovskite $BaRuO_3$ and evolution of ferromagnetism in $ARuO_3$ (A = Ca, Sr, Ba) ruthenates," *Proc. Natl. Acad. Sci.* **105**

(2008) 7115. 134

253. J. Pendry, *Low Energy Electron Diffraction: The Theory and its Application to Determination of Surface Structure*. Academic Press, London, 1974. 136

254. M. V. Hove and S. Tong, *Surface Crystallography by LEED: Theory, Computation, and Structural Results*. Springer-Verlag, Berlin, 1979.

255. M. V. Hove, W. Weinberg, and C.-M. Chan, *Low Energy Electron Diffraction: Experiment, Theory, and Surface Structure Determination*. Springer-Verlag, Berlin, 1979. 136

256. A. Barbieri and M. V. Hove. private communication. 138

257. L. Mattheiss, "Energy bands for solid argon," *Phys. Rev.* **133** (1964) A1399. 139

258. P. Blaha, K. Schwarz, G. K. H. Madsen, D. Kvasnicka, and J. Luitz, *WIEN2K, An Augmented Plane Wave + Local Orbitals Program for Calculating Crystal Properties*. Karlheinz Schwarz, Techn. Universität Wien, Austria, 2001. 139

259. R. Moore, *Manifestations of Broken Symmetry: The Surface Phases of* $Ca_{2-x}Sr_xRuO_4$. PhD thesis, University of Tennessee, 2006. 143

260. M. V. Hove *et al.*, "Automated determination of complex surface structures by LEED," *Surf. Sci. Rep.* **19** (1993) 191. 143

261. V. Nascimento *et al.*, "Procedure for LEED IV structural analysis of metal oxide surfaces: $Ca_{1.5}Sr_{0.5}RuO_4(001)$," *Phys. Rev. B* **75** (2007) 035408. 144

262. J. Pendry, "Reliability factors for LEED calculations," *J. Phys. C: Solid State Phys.* **13** (1980) 937. 146